Structure and magnetism of B2 chemically ordered FeRh nanoclusters in carbon matrix, as a nanocluster assembled film and over perovskite substrate

Guillermo Alberto Herrera Huerta

THESE de DOCTORAT DE
L'UNIVERSITÉ CLAUDE BERNARD LYON 1

Ecole Doctorale N°52
Physique et Astrophysique

Discipline : Physique

Soutenue publiquement le 22/05/2023, par :

Guillermo Alberto HERRERA HUERTA

Structure and magnetism of B2 chemically ordered FeRh nanoclusters in carbon matrix, as a nanocluster assembled film and over perovskite substrate

---

Devant le jury composé de :

COTTANCIN Emmanuel Professeur des Universités, ILM	**Président**
ANDREAZZA Pascal Professeur des Universités, ICMN	**Rapporteur**
RESPAUD Marc Professeur des Universités, INSA	**Rapporteur**
BARTHELEMY Agnès Professeur des Universités, Thales	**Examinatrice**
MAGNAN Hélène Ingénieure Chercheure, SPEC	**Examinatrice**
PICCOLO Laurent Directeur de Recherche, IRCELYON	**Examinateur**
DUPUIS Véronique Directrice de Recherche, ILM	**Directrice de thèse**
CANERO-INFANTE Ingrid Chargée de Recherche, INL	**Co-Directrice de thèse**

A mis padres; Carlos y Nancy
A mi abuelo Alberto

Acknowledgment

Agradezco a mis padres Carlos Herrera y Nancy Huerta por todo el soporte y amor que me han dado, y que sin ellos nada de esto hubiese sido posible. De igual manera agradezco a mis hermanas Teresa, Beatriz y, a mi sobrina Rebeca por apoyarme siempre.

My thanks to Veronique and Ingrid that guide me and help me in the research as well in other complexities of arriving to a new country.

I would like to thanks to everyone directly and indirectly involved in the VOLCONANO project; Sara Gonzales, Matthieu Bugnet, Patrick Schoeffmann, Edwidge Otero, Phillipe Orhesser, Damien Le Roy, Olivier Boisron, Adela Reyes, Celine Raton, Jittu Mathew, Armin Kleibert, Nicholas Blanchard, Bruno Canut, Fabrice Wilhelm, Tournus Florent and Alexandre Tamion.

Thanks to my friends who supported me from Chile and other parts of the world; Fernanda Perez, Daniela Mancilla, Leonardo Leiva, Eva Riveros, Juan Fernandez. Thanks to *Ramchilacha* and the ones who played DnD with me; Juan Pablo Vargas, Carolina Gonzales, Pandora Escobar, Jose Gonzales, Maximiliano Rubio, Daniel Cornejo , Josu Armendariz and Lenz Pueller. I want to give a special thanks to my best friend Eva Diaz.

Also I am happy to have shared time with others students which I thank their presence in the iLM as Charles, Vincent, Antoine Bard, Antoine Ollivier, Joseph, Paul, Jerome and Emric.

Title: Structure and magnetism of B2 chemically ordered FeRh nanoclusters in carbon matrix, as a nanocluster assembled film and over perovskite substrate

Abstract: Controlling nanomagnetism by means of an electric field is a key issue for the future development of low-power spintronics. In this context, CsCl-like B2 chemically ordered near equiatomic FeRh alloy, which presents a metamagnetic transition from antiferromagnetic order (< 370 K) to ferromagnetic order (> 370 K), is a very good candidate for assisting magnetic control through external stimuli. Recently, a ferroelectric crystal has been used to electrically drive the temperature of such phase transition of epitaxially grown FeRh films with only a few volts, with potential media applications for thermally assisted magnetic recording. This effect may be the signature of magnetic exchange correlations, acting at shorter-range in the antiferromagnetic phases than in the ferromagnetic phases.

In this work it is shown the study of FeRh nanoclusters prepared by low energy cluster beam deposition, in different system configurations at the non chemically ordered A1 phase and the chemically ordered B2 phase, which was achieved after annealing at high temperatures under vacuum.

In order to achieve a better understanding of the metamagnetic transition, we studied diluted FeRh nanoclusters in a carbon matrix, revealing that the persistence of the ferromagnetic phase at lower temperatures is an intrinsic characteristic determined by the size, regardless of the nanucluster density.

Even more, the study on FeRh nanocluster-assembled films has shown not only the option to achieve the metamagnetic transition for crystallite sizes higher than 20 nm, but also the coexistence of ferromagnetic and antiferromagnetic orders in the nanogranular system, becoming an interesting point to engineer the metamagnetic transition.

By using X-ray spectroscopy and diffraction under synchrotron facilities and scanning transmission microscopy on cross-section lamella, the epitaxial relationship between FeRh nanocluster with $SrTiO_3$ and $BaTiO_3$ surfaces is described well, showing that the competition between induced strain at the metal/oxide interface and cluster surface relaxation is not enough to induce antiferromagnetic order in FeRh nanoparticles.

Keywords: Nanoclusters, FeRh, Size effects, Perovskite, Epitaxy, Magnetism.

Titre: Structure et magnétisme de nanoclusters de FeRh chimiquement ordonnés B2 dans une matrice de carbone, sous forme de film assemblé par nanocluster et sur un substrat de pérovskite

Résumé: Etre capable de contrôler le magnétisme au moyen d'un champ électrique est une question essentielle pour le développement de futur dispositif d'électronique de spin, de faible consommation. Dans ce contexte, au voisinage de la composition équiatomique, l'alliage FeRh chimiquement ordonné dans la phase B2 CsCl qui présente une transition métamagnétique depuis un ordre antiferromagnétique à basse température vers un ordre ferromagnétique juste au-dessus de la température ambiante, est un excellent candidat pour évaluer cette possibilité de modifier le magnétisme par un stimulus extérieur. En effet, récemment un cristal ferroélectrique a été utilisé pour induire par l'application de quelques volts, une modification de la température de transition de phase métamagnétique sur un film FeRh épitaxié avec des applications potentielles pour l'enregistrement dense thermiquement activé.

Dans ce travail sont étudiés des nanoclusters de FeRh préparés par *Low Energy Cluster Beam Deposition* initialement dans la phase A1 chimiquement désordonnée qui cristallisent dans la phase B2 chimiquement ordonnée après recuit sous vide à haute température.

Afin de mieux comprendre la transition métamagnétique dans la phase B2, nous avons étudié des agrégats triés en taille de FeRh dilués en matrice de carbone après recuit, révélant que la persistence de la phase ferromagnétique à basses températures est une caractéristique intrinsèque déterminée par la taille des nanoaimants quelle que soit leur densité.

De plus, notre étude sur des films d'assemblée d'agrégats de FeRh en interaction a montré non seulement la possibilité d'observer la transition métamagnétique pour des nanocristallites B2 coalescés après recuit, de tailles supérieures à 25 nm mais aussi la coexistence d'ordre ferromagnétique et antiferromagnétique dans un tel système nanogranulaire, devenant un point intéressant pour ajuster la transition métamagnétique.

En utilisant la spectroscopie et la diffraction des rayons X sous synchrotron et la microscopie à transmission à balayage sur lamelle en coupe transversale, nous décrivons bien les relations d'épitaxie entre les facettes des nanoclusters FeRh dans la phase B2 avec une surface monocristalline $SrTiO_3$ et $BaTiO_3$ (001). Par contre, la contrainte induite au niveau de l'interface métal/oxyde en compétition avec la relaxation à la surface de l'agrégat, n'est pas suffisante pour induire un ordre antiferromagnétique dans des nanoaimants chimiquement ordonnés de FeRh de moins de 12 nm de diamètre.

Keywords: Agrégats, FeRh, Effets de taille, Perovskite, Épitaxie, Magnétisme.

Glossary

D	Nanocluster size as the diameter of a circle with same projected area of the nanocluster.
D_1	Monomer size as the diameter of a circle with same projected area of the Monomer.
D_2	Dimer size as the diameter of a circle with same projected area of the Dimer.
D_{3+}	N-mer size as the diameter of a circle with same projected area of the N-mer for N>2.
A1 phase	Strukturbericht designation face centered cube crystal.
AFM	Antiferromagnetic/Antiferromagnetism.
AR	Aspect Ratio, as the minor semi axis divided by major semi axis for a fitted ellipse.
B2 phase	Strukturbericht designation for a 2-elements crystal, a cube sub-lattice for one element and the second element in the center of the cube.
BOE	Buffered oxide etch .
BTO	Barium titanate, $BaTiO_3$.
C	Circularity as the $4\pi area/perimeter^2$.
Coalescence model	Model that assumes that nanoparticles merge into a spherical N-mere.
DCD	Direct current demagnetization.
EB	Exchange Bias; magnetic interaction at the contact of two magnetic lattice.
EDX	Energy-Dispersive X-ray spectroscopy.
FC	Field Cooling, measurement of the magnetic moment as function of the temperature while cooling with applied external field.
FFT	Fast Fourier Transform.

FLUO	Fluorescence yield, the emitted X-ray of a sample.
FM	Ferromagnetic/Ferromagnetism.
GISAX	Grazing incidence small angle x-ray diffraction.
GIWAX	Grazing incidence wide angle x-ray diffraction.
HAADF	High Angular Annular Dark Field.
HD	High density nanocluster, above 5% of surface occupation.
IRM	Isothermal remanent magnetization.
LD	Low density nanocluster, below 5% of surface occupation.
LECBD	Low energy cluster beam deposition without mass selection.
LECBD-MS	Low energy cluster beam deposition with mass selection.
MAE	Magnetic anisotropy energy.
Necklace model	Model that assumes that when nanoparticles can touch between each other but do not merge.
NN	Smaller distance boundary-to-boundary between a nanocluster and its nearest neighbor .
Non Switchable	On this thesis is used for magnetic contribution that does not present metamagnetic transition.
PLYRA	Lyonnaise Research Platform on Clusters (Plateforme Lyonnaise de Recherche sur les Agrégats).
RBS	Rutherford backscattering spectrometry.
SMSI	Strong metal support interaction.
SQUID	Superconducting quantum interferometer device.
STEM	Scanning transmission electron microscopy.
STO	Strontium titanate, $SrTiO_3$.
Switchable	On this thesis is used for magnetic contribution that present metamagnetic transition.
TEM	Transmission electron microscopy.
TEM grid	Copper grid with a layer of amorphous carbon used as support of nanoparticles to measure them from TEM.

TEY	Total electron yield.
UHV	Ultra high vacuum, pressure lower than 10^{-9} mbar.
XANES	X-ray absorption near edge structure.
XAS	X-ray absorption.
XMCD	X-ray magnetic circular dichroism.
XPS	X-ray photoelectron spectroscopy.
XRD	X-ray diffraction.
ZFC	Zero Field Cooling, measurement of the magnetic moment as function of the temperature while cooling with no applied external field.

Contents

List of Figures

List of Tables

List of samples

The sample preparation and treatment of the substrates are described in chapter 2. The letter C represents one carbon capping layer of nominal thickness 2 nm.

Chapter	Sample name	Sample description	Nominal monomer size
3	LD	C/FeRh 0.1 nm/TEM grid	7 nm
	HD	C/FeRh 1 nm/TEM grid	7 nm
	LD2	15x(C/FeRh 0.13 nm)/Si	7 nm
	HD2	2x(2C/FeRh 1 nm)/Si	7 nm
4	T1	7C/FeRh 150 nm/Si	non mass selected
	T2	FeRh 150 nm/Si	non mass selected
5	P1	2C/FeRh 0.5 nm/STO	3 nm
	P2	2C/FeRh 1 nm/BTO 7 nm/STO	7 nm
	P3	2C/FeRh 0.5 nm/NbSTO	3 nm

Table 0: List of samples

Introduction

There are many configurations of magnetic materials. For example, ferromagnetism is when the atomic magnetic moments are aligned parallel in the same orientation, resulting in a total magnetic field in the volume after having been exposed to an external magnetic field. The alignment itself can be used for recording purposes, since each orientation of an axis could be a binary value. Also the magnetic moment is an additional degree of freedom with a contribution to entropy and therefore temperature. While the inherent magnetic field and its interaction with charge (mainly Lorentz force) is commonly used for energy conversion, detection, storage and imaging.

On the other hand, antiferromagnetism corresponds to having atomic magnetic moments aligned in parallel but with opposite orientation, leading to a null total magnetic moment even after having been exposed to an external magnetic field. It doesn't have yet as many applications as ferromagnetism but having a magnetic lattice that will not affect other near magnetic components, such as skyrmions or magnons, could be used in the future.

In the vast options of magnetic materials, FeRh (Iron Rhodium) has a particular standing. It is an alloy that when at 50/50 atomic ratio and chemically ordered in the B2 CsCl phase, behaves as an antiferromagnet at room temperature but, if it is heated over 370 K, its lattice parameter expands approximately 0.5% and it becomes a ferromagnet. This phenomenon is called the *FeRh metamagnetic transition*. Since this corresponds to a switch between antiferromagnetic to ferromagnetic configurations, it has the potential for new applications such as information storage and magnetocooling. However, temperature is normally a parameter which is hard to control for applications, so it is important to explore other ways to control the FeRh metamagnetic transition.

Another important point is the miniaturization of electronic components in industry, making it important to study the system at nanoscale. Size effects could bring new phenomena or change properties already present, making necessary to explore the *FeRh metamagnetic transition* for diluted nanoparticles regardless of the substrate.

Size effects are not exclusive of isolated nanoparticles. A continuous film made up of assembled nanoclusters may report behaviors of low size cristallites, as if it were an isolated nanoparticle but with strong interactions between them. This means that a nanocluster assembled FeRh film could present novel properties, as well as give hints to solve the interactions contribution that could dominate over the FeRh metamagnetic transition.

The most common parameter to control on a device is voltage. In this aspect,

the ferroelectric perovskite $BaTiO_3$ or BTO (Barium Titanate) is an interesting substrate for FeRh nanostructures growth. When voltage is applied on BTO, its lattice parameter expands so, if an epitaxial relationship exists between FeRh and BTO, then it would be possible to induce strain on FeRh by applying voltage over the BTO substrate. This phenomena has been studied for FeRh films but not yet for FeRh nanoparticles which have various surface faces, which could lead to different epitaxies and therefore a different control over the FeRh metamagnetic transition than for the film.

This PhD thesis studies the FeRh magnetic and structural properties for the following 3 systems: FeRh nanoparticles embedded in a carbon matrix, FeRh nanocluster assembled films, and FeRh nanoparticles over BTO and STO substrates. The main objective is to see what parameters affect the metamagnetic transition and what is the physical mechanism behind that.

This thesis has been divided in six chapters:

- **Background**: Here several concepts used in this work are explained, as well the main properties of the used materials.
- **Setups**: Here the different experimental setups and techniques used to characterize the prepared samples are described.
- **FeRh nanocluster embedded in a carbon matrix**: The study of the magnetic properties of FeRh nanoclusters with size lower than 10 nm embedded in an amorphous carbon matrix.
- **FeRh nanocluster assembled film**: The study of a nanocluster assembled film of FeRh over an Si substrate.
- **FeRh nanocluster over perovskite substrates**: The study of FeRh nanoparticles with size below 10 nm deposited on BTO (Barium Titanate) and STO (Strontium titanate) substrate.
- **General conclusions**: General outlook of the obtained results.

Chapter 1

Background

1.1 Iron Rhodium

Iron rhodium (FeRh) is an alloy whose bulk, when at equiatomic ratio, has two possible crystalline phases: the non chemically ordered γ A1 phase, and the chemically ordered B2 phase [1–3] (Figure 1.1).

The γ FeRh A1 phase corresponds to a face-centered cubic lattice (fcc) with either Fe or Rh in each position and a lattice parameter of a =3.736 Å (ICDD 04-011-5204). It can be identified by the fact that in the Fourier space it can only have all three Miller indices [hkl] either odd or even, as expected for a fcc lattice. By definition, in the *Strukturbericht* designation the letter A in A1 indicates the presence of one element, but the common way to address this FeRh phase in multiple papers is A1 phase [4]. This FeRh phase is paramagnetic (Figure 1.1).

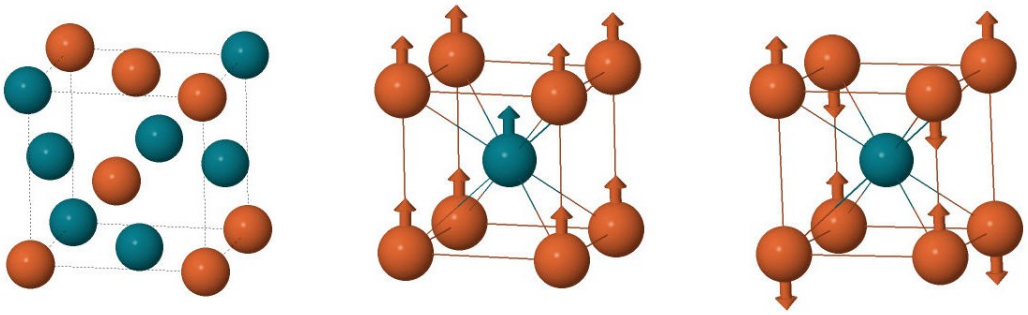

Figure 1.1: FeRh crystalline phases

Fe atoms in red and Rh atoms in blue. Left: FeRh A1 phase. Middle: FeRh B2 ferromagnetic phase. Right: FeRh B2 antiferromagnetic phase.

The bulk FeRh B2 phase is like a body-centered cubic lattice (bcc-like), resembling a B2 phase according to the *Strukturbericht* designation. This structure consists of one element positioned at the apex and the second element at the center, adhering to the definition of a B2 phase. Due to the presence of distinct atomic sublattices, Fourier analysis allows to observe the Miller indices $[hkl]$ where $h+k+l$ are odd. These indices correspond to a bcc structure but also include the forbidden peaks with less intensity. This is the reason why this crystal is called bcc-like.

Bulk FeRh B2 phase has two configurations: α'' and α'. The α'' phase, stable for temperatures below 370 K, has a lattice parameter of a =2.982 Å (ICDD 04-002-2003) and presents antiferromagnetic behaviour, with atomic magnetic moments $m_{Fe} = 3.3\mu_B$ and $m_{Rh} = 0\mu_B$. On the other hand, the α' phase, stable for temperatures above 370 K, has a lattice parameter of 2.997 Å (ICDD 04-004-8435) and exhibits ferromagnetic behaviour with atomic magnetic moments $m_{Fe} = 3.2\mu_B$ and $m_{Rh} = 0.9\mu_B$ [5–7] (Figure 1.1).

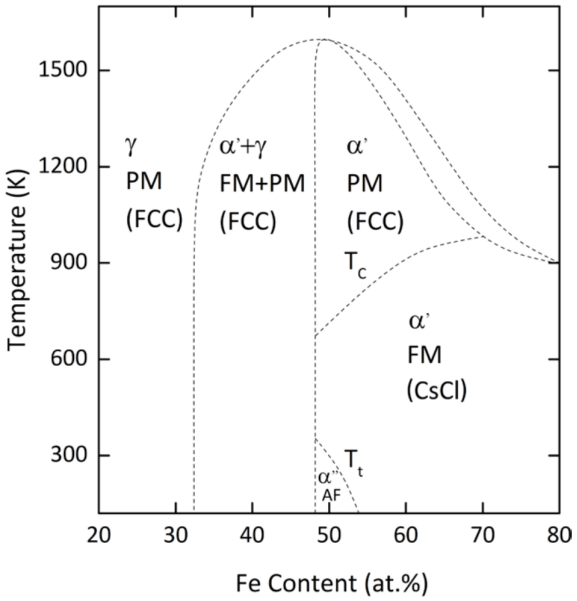

Figure 1.2: Phase diagram of FeRh

Phase diagram of FeRh at different concentrations and temperatures. The magnetic order can be antiferromagnetic (AFM), ferromagnetic (FM) and paramagnetic (PM). α'' corresponds to the antiferromagnetic B2 phase, α' is the B2 in the ferromagnetic state or paramagnetic state and A1 phase corresponds to the γ paramagnetic state, with T_T the transition temperature and T_C the Curie temperature [8, 9]

The change in magnetic order as function of the temperature in FeRh B2 phase was first discovered by Fallot in 1938 [5, 10]. The so-called *FeRh metam-*

agnetic transition in bulk is symmetrical and it is open, which means that the range of temperature where FeRh is antiferromagnetic is wider if temperature increases from the antiferromagnetic regime, and shorter if it cools down from the ferromagnetic regime (Figure 1.3).

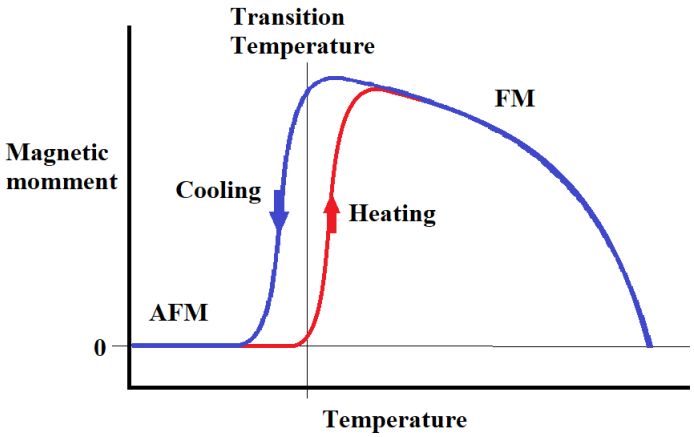

Figure 1.3: FeRh metamagnetic transition.

Schematic of the metamagnetic transition of FeRh bulk observed in the curve of magnetization as function of the temperature.

The FeRh metamagnetic transition in the range of temperature with the opening it has the coexistence of the magnetic domains ferromagnetic and antiferromagnetic [11–13].

This FeRh's metamagnetic transition brings potential uses of FeRh for *Thermally Assisted Recording* (TAR) [14], magneto-caloric devices [15–21] and ultrafast spintronics [22, 23]

Early models attempted to explain the metamagnetic transition in FeRh using ising-like models [24–26] but such FM to AFM phase transition near room temperature implies coercitive fields higher than the ones obtained in experiments and are not well adapted to low dimentional systems.

Using a four-spin hamiltonian which is very sensitive to the surface effects, a model to explore the case of thin films was recently proposed by *McGrath* [27]. With the main feature of including in the exchange energy, a quartets component to the bilinear terms considering only *Fe-Fe* interaction (Figure 1.4). In the equation 1.1 beside the exchange interaction terms between nearest neighbors NN and between next nearest neighbors NNN pairs, are added the quartets interaction.

$$\epsilon_{ex} = -\sum_{NN} J_1 s_i \cdot s_j - \sum_{NNN} J_2 s_i \cdot s_j$$
$$+\frac{1}{3}\sum_{quartets} D_{ijkl}[(s_i \cdot s_j)(s_k \cdot s_l) + (s_i \cdot s_k)(s_j \cdot s_l) + (s_i \cdot s_l)(s_k \cdot s_j)] \quad (1.1)$$

The McGrath model was used to describe films, exhibiting a metamagnetic transition even with four monolayers of Fe (Figure 1.4) but does not describe residual ferromagnetic component at low temperature neither the coexistence of ferromagnetic and antiferromagnetic domains. For the moment there is no model that fully satisfy the magnetic properties observed in FeRh.

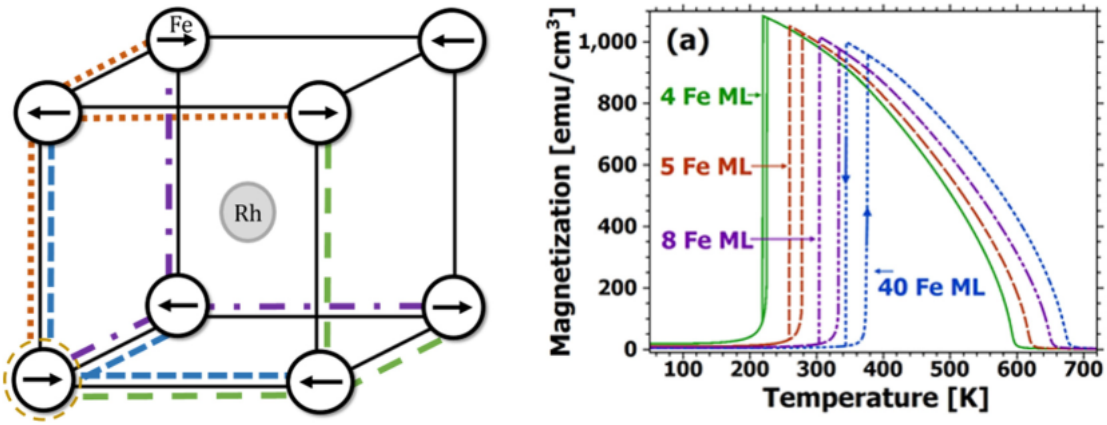

Figure 1.4: McGrath model.

On the left a scheme of the positions invloved on a quartet interaction. On the right the magnetization as function of the temperature obtained with the McGrath model fot a FeRh(001) film with four Fe atomic layers [27].

Cao et al studied the FeRh metamagnetic transition on a 150 nm film made by sputtering on MgO substrate and post annealed at different temperatures from 200 °C to 700 °C.

The magnetization curves as function of the temperature indicate that the system stays in the ferromagnetic regime up to annealing at 400 °C and then the metamagnetic transition progressively occurs by increasing annealing temperature (Figure 1.5).

Hysteresis loops at different temperatures reveal a peculiar opening at the saturation region at temperatures inside the metamagnetic transition 110 °C< T <116 °C (Figure 1.5).

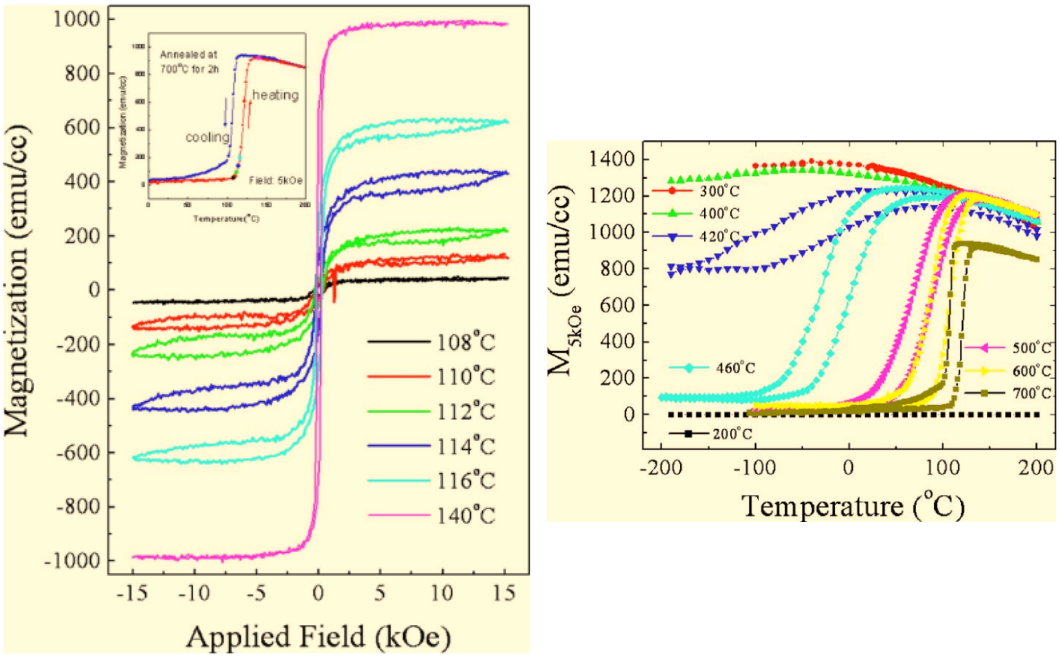

Figure 1.5: Magnetization for 150 nm FeRh film over MgO.

Magnetization as function of the temperature at 5 kOe (right) and hysteresis loops for different temperatures inside the 'magnetization as function of the temperature loop' (left) for a 150 nm FeRh film done by sputtering over MgO [28]

In the work presented by *Maat et al* on 110 nm FeRh films deposited on MgO, the hysteresis loops performed in the region of metamagnetic transition for the heating up branch at 0 T and the cooling down branch at 5 T posse an opening in the approach to saturation region wider than the ones observed by *Cao et al* [24]. On a similar 110 nm FeRh system over MgO, *Suzuki et al* showed that the opening in the saturation region of the hysteresis loop disappear when the fully ferromagnetic regime is achieved [29]. We can notice also in Figure 1.6 that the first cycle path of the hysteresis loops is not the same as the second cycle path, indicating that when the hysteresis loops is performed it leaves the branch (colling down branch or heating up branch).

Maat et al also found that the transition temperature as function of the external field posses a linear behaviour observed in both the magnetization as function of the temperature at fixed external field and magnetization as function of the external field at fixed temperature (Figure 1.6).

Pressacco et al studied a FeRh(001) films with 50 nm thickness deposited over MgO from XAS/XMCD and XPS [30]. Adjusting intensities with an exponential weight they showed that the top four layers remain ferromagnetic, the fifth layer

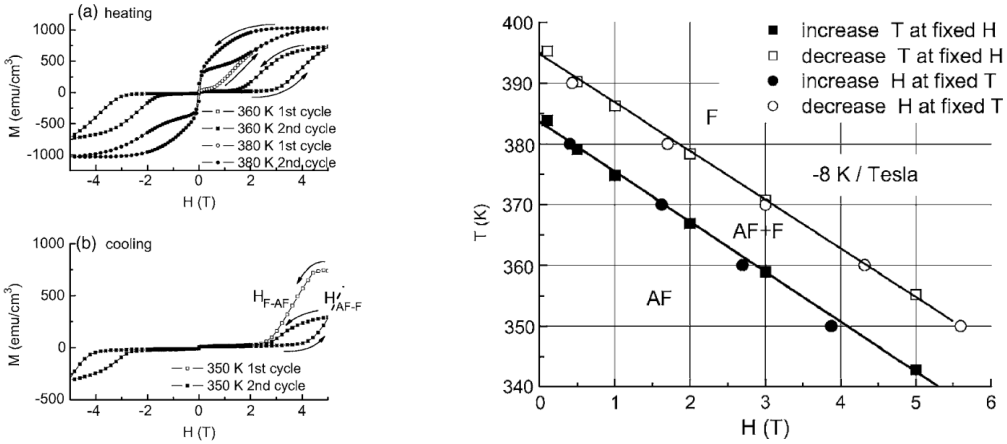

Figure 1.6: Magnetization for 110 nm FeRh film over MgO.

(Left) Field hysteresis loops for FeRh/MgO(001) upon heating taken at 360 K and 380 K for 0 T (a) and cooling at 350 K for 5 T (b), the open symbol correspond to the beging of the loop. (Right) Metamagnetic transition temperature as funcion of the field observed in hysteresys loops ans as function of the temperature [24].

has an intermediate 60% of magnetization while the core of the sample is in the antiferomagnetic state. These results indicate that the FeRh(001) surface persist in the ferromagnetic regime below the transition temperature (Figure 1.7).

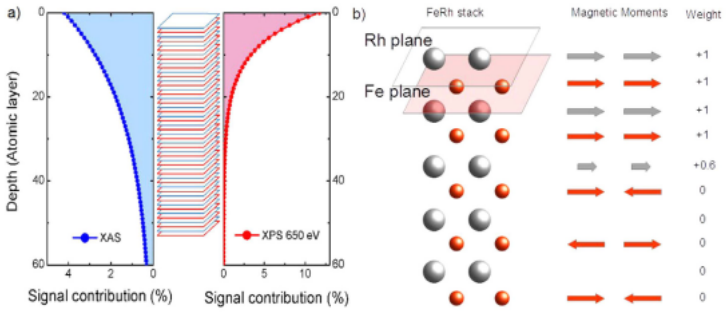

Figure 1.7: FeRh(001) magnetization at different depths

Signal contribution from XAS and XPS at different deeps and the magnetic moment weight relative to the bulk ferromagnetic FeRh at different deeps [30]

In order to determine where the metamagnetic transition occurs and where the ferromagnetic regime remains at low temperature, *Gatel et al* used electron holography on a FeRh wire of 80 nm wide and 50 nm tall. They find a residual ferromagnetic domain on the surface of the wire that expand as the temperature increases but also that ferromagnetic regions appear at 50 °C on the volume of the

wire and cover mover volume as the temperature increases [31].

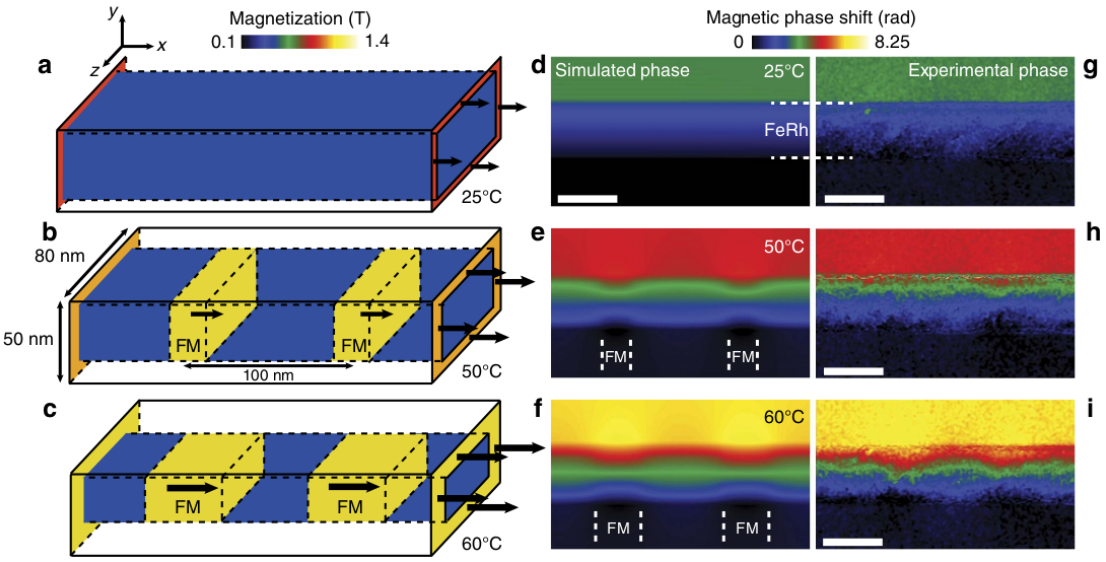

Figure 1.8: Metamagnetic transition on an FeRh wier observed by electron holography

(a-c) 3D schemes used for the micromagnetic simulations. Comparison between simulated magnetic phase images calculated from micromagnetic simulations (d-f) and experimental magnetic phase images obtained at same temperatures (g-h). Scale bars represent 50 nm. [31]

Other experimental studies on FeRh films made by sputtering with thickness from 3 nm to 10 nm over Si/SiO and covered by MgO reported by *Han et al* [32] indicate that as the film thickness decreases, the residual magnetization at low temperatures increases and the metamagnetic transition becomes broader (Figure 1.9).

A point to take into account is that the thin samples studied by *Han et al* correspond to multi granular systems, where the grain size is determined from surface morphology observed by atomic force microscopy. They noted that the projected grain size decreases from 66 nm to 39 nm when the film FeRh thickness decreases from 8 nm to 5 nm. For a smaller film thickness of 3 nm, they found a projected grain size of only 32 nm, making harder and harder the antiferromagnetic phase formation which become more and more unstable probably due to surface/interface effects.

All these results infer that a strong correlation between metamagnetic transition and size or surface ratio effects probably exist in the FeRh system. This places nanoparticles as very interesting benchmark systems.

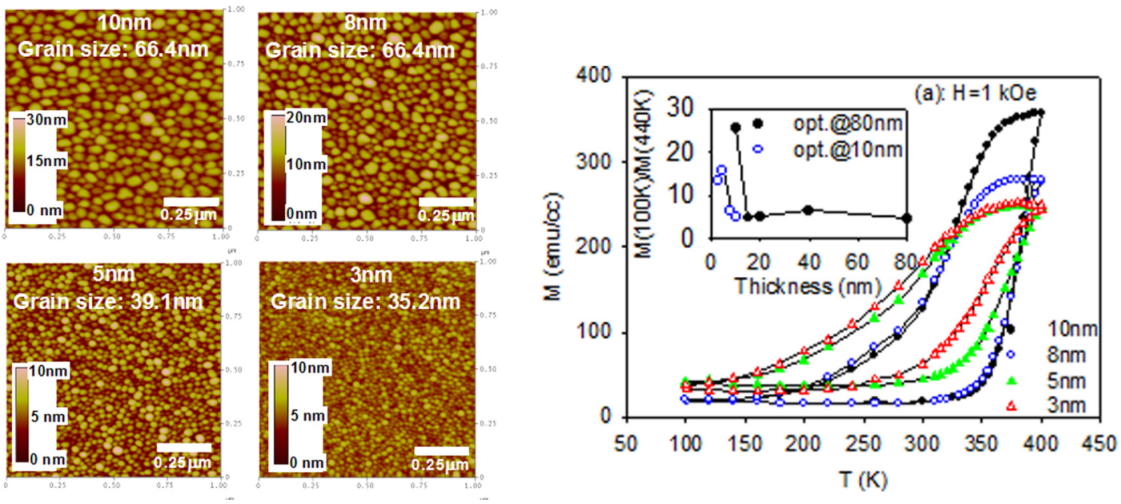

Figure 1.9: Topography and Magnetization for FeRh thin film on Si/SiO.

Atomic force microscopy images for diferen thickness of FeRh thin films over Si/SiO covered with MgO (left) and the correspondant magnetization as function of the temperature for 1 T. On insert the ratio of residual magnetization at 100 K and 400 K. Adapted from [32].

1.2 Nanoalloys

The properties of magnetic nanoparticles have presented potential applications in spintronics and neuromorphic computing [33]. But, for single domain the data storage is not compatible with the superparamagnetic (SP) behavior due to the competition between the magnetic anisotropy energy (MAE) and the thermal energy activation. Efforts have been done to solve this technological limitation by combining nanocluster of 3d metals with high spin moment as Fe or Co in contact with 4d/5d metals as Pd, Rh or Pt in order to induce by direct exchange a large orbital magnetic moment from 4d/5d metals [34]. As an example to overcome the super paramagnetism in nanoparticles, tetragonal $L1_0$ CoPt and FePt have been studied intensively to increase the magnetocristalline anysotropy and obtain high MAE which regardless the efforts have not been achieved [35, 36].

1.3 Nanocluster

Nanoparticles present some particularities that give them unique properties non observed in bulk materials. The surface/volume ratio for a nanoparticle is higher than for a bulk sample and it posses specific geometry according to its crystal lattice [37]. A perfect truncated octahedron nanoparticle of FeRh A1 phase with

5 atoms per vertex it has 3 nm size and posses 1289 atoms and 482 of them are at the surface which correspond to the 37% of the atoms. While a rhomboic dodecahedron nanoparticle of FeRh in B2 phase with 8 atoms per vertex, has a 3 nm mean size with 1695 atoms and 590 of them at the surface, which correspond to 35% of the atoms (Figure 1.10).

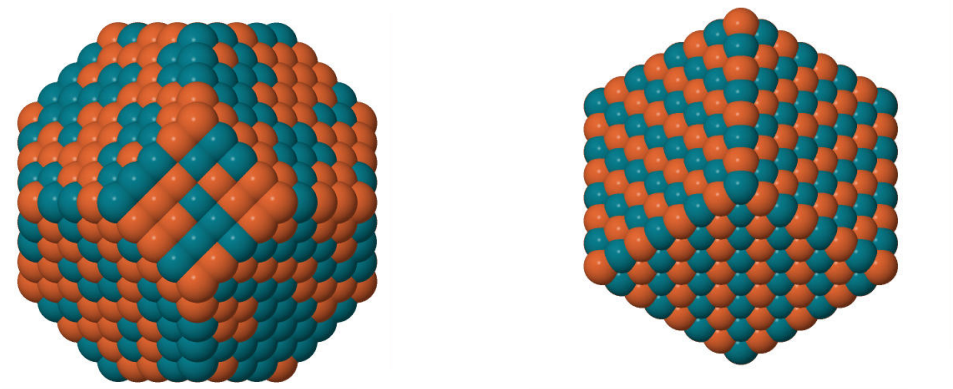

Figure 1.10: FeRh ∼3 nm nanoparticles

A truncated octahedron nanoparticle of FeRh A1 phase with 3.0 nm size (left) and a rhomboic dodecahedron nanoparticle of FeRh B2 phase with 3.0 nm size (right).

Varying the size of nanoparticles will change the surface ratio; As example a A1 phase FeRh nanoparticle with truncated octahedron shape and 11 atoms per vertex it has 7.4 nm mean size and posses 19889 atoms with 3300 of them at the surface which correspond to 16% of the atoms. While a FeRh B2 phase nanoparticle with rhombic dodecahedron and 18 atoms per vertex will have 7.2 nm mean size and posses 21455 atoms, 3470 of them at the surface which correspond to 16% of the atoms (Figure 1.11).

Nanoparticles have many shape options according to its crystal lattice [37] but also the distribution of different materials may differ for specific alloys and preparation methods. sometimes, element segregation tendency lead to the formation of core-shell structure [38–41]

Random deposition of nanoparticles makes possible contact between them, higher amount of nanoparticles and higher nanoparticle size will increase the chances of getting touch [42]. When a nanoparticle is isolated is called *monomer* and its size will be denoted as D_1, if 2 nanoparticles are in contact is a *dimer* with size D_2 and as a general rule if N nanoparticles are in contact it will correspond to a *N-mer* with size D_N. The mean diameter will be denoted as D_{mean}.

Commonly to characterize size and shape of a nanoparticle it is observed from above, and the direct measures are the area projected and perimeter of the

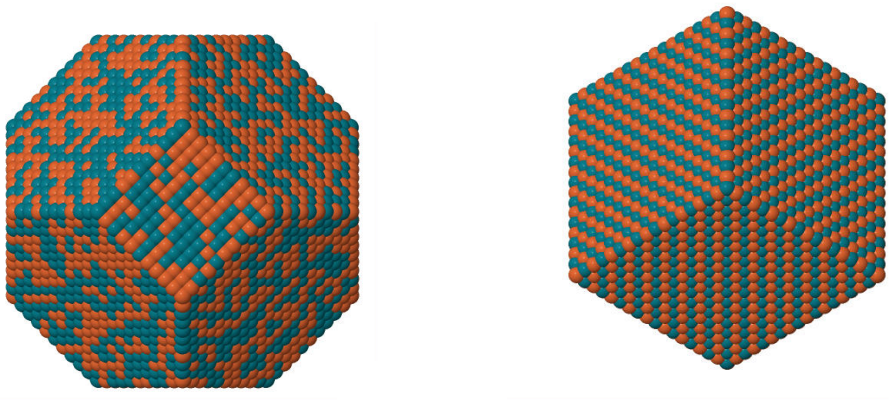

Figure 1.11: FeRh ∼7 nm nanoparticles

A truncated octahedron nanoparticle of FeRh A1 phase with 7.4 nm size (left) and a rhomboic dodecahedron nanoparticle of FeRh B2 phase with 7.2 nm size (right).

Phase	D (nm)	At_T	At_S	At_S (%)
A1	7.2	19900	3300	16%
A1	3.0	1289	482	37%
B2	7.4	21455	3470	16%
B2	3.0	1695	590	35%

Table 1.1: Nanoparticle surface/volume ratio

Number of atoms in volume (At_T) and surface (At_S) for FeRh at different phases and size (D)

nanoparticle in the image. The size of the nanoparticle is defined as the diameter of a circle with same area as the measured projected area of the nanoparticle $D = \sqrt{4Area_{proyected}/\pi}$. So with this definition the size on a N-mere D_N with projected area A_N is $D_N = \sqrt{4A_N/\pi}$ but this does not mean that the area projected is circular.

The nanoparticle size properties can be highly relevant for other properties as the magnetism that can be related to a size effect [43, 44] but also the magnetic properties of a material may be different at the surface [30].

Different shapes, sizes and distances for the nanoparticles in the cluster can be achieved [42, 45]. For this work we will consider two configurations; the *Necklace model* and the *Coalescence model*.

1.3.1 Necklace model for nanoparticles

This correspond to the case that to the substrate arrives a specific size of nanoparticle that could have any shape, the Necklace model assumes that the energy on the nanoparticles is not enough to coalesce neither make their shape changes, on fly or when arrives to the substrate. This imply that a D_N will look like a concatenation of N times D_1 (Figure 1.12).

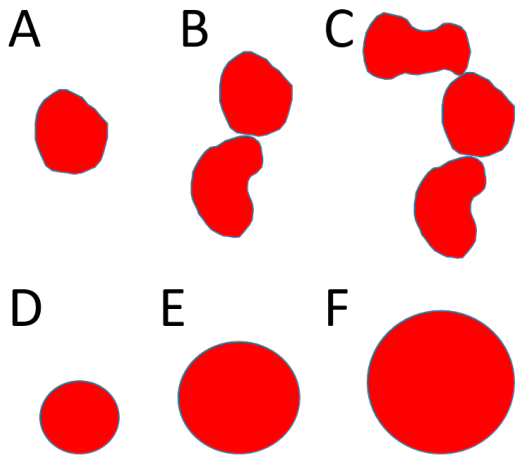

Figure 1.12: Models to describe naoparticle coalescence

For a spherical monomer A, B and C correspond to the monomer, dimer and trimer for the necklace model and D, E and F to the monomer, dimer and trimer for a coalesced model respectively.

So, for well defined monomer size with a *Necklace model*, the total area measured over one N-mer A_N should correspond to N times the area of the monomer A_1. In the same way the perimeter P_N should be close to N times the perimeter of the monomer P_1. And we obtain that A_N as function of P_N is linear, while D_N increases as the square root of N (Eq. 1.4).

$$\text{By definition: } A_N = \frac{\pi D_N^2}{4} \ , \ A_1 = \frac{\pi D_1^2}{4} \tag{1.2}$$

$$\text{For Necklace model: } A_N = A_1 N \ , \ P_N = P_1 N \tag{1.3}$$

$$\rightarrow A_N = \frac{A_1}{P_1} P_N \ , \ D_N = \sqrt{N} D_1 \tag{1.4}$$

1.3.2 Coalescence model for nanoparticles

If the nanoparticles lose their initial shape and coalesce, we can assume volume conservation and still can find some relations using that the volume of the *N-mer* V_N is N times the volume of the monomer. There is many configurations for the coalesced nanoparticle but here we will focus on the case of a perfect spherical shape for the *N-mer*. We have to notice that here A_N correspond to the projected area of the *N-mer*, not the area of the volume V_N. For this case, the A_N as function of the P_N should be quadratic and D_N increases as the cube root of N (Eq. 1.7).

$$\text{By definition: } A_N = \frac{\pi D_N^2}{4} \tag{1.5}$$

$$\text{For Coalescence model: } V_N = V_1 N \ , \ V_N = \frac{\pi D_N^3}{6} \ , \ P_N = \pi D_N \tag{1.6}$$

$$\rightarrow A_N = \frac{P_N^2}{4\pi} \ , \ D_N = \sqrt[3]{N} D_1 \tag{1.7}$$

1.3.3 Shape description

The agglomeration of nanoparticles in necklace model or coalesce model can also be described by shape parameters.

The circularity corresponds to a normalized ratio between the perimeter and the area, $C = 4\pi P/A$ obtaining $C = 1$ for a sphere, for example for a nanoarticle with constant projected surface if the circularity decrease it means that the perimeter increases.

In order to distinguish if the increase of surface corresponds to a corrugate shape or an elongated shape it can be used the aspect ratio. If we fit an ellipse for the nanoparticle, the aspect ratio (AR) will correspond to the ratio between the minor semi-axis and the major semi-axis so, aspect ratio $AR = 1$ means that the best ellipsoidal fit is a circle.

Taking these relations in consideration $C \rightarrow 1$ and $AR \rightarrow 1$ indicate that the nanoparticle is like a circle, $C \rightarrow 0$ and $AR \rightarrow 1$ is like a highly corrugated circle and $C \rightarrow 0$ and $AR \rightarrow 0$ is like a very elongated ellipse or a line. The case $C \rightarrow 1$ and $AR \rightarrow 0$ is mathematically impossible due the fact that $C \rightarrow 1$ just by itself determine that the nanoparticle is a circle then AR must be 1.

The coalescence of nanoparticles could depend on many factors, the aspect ratio and circularity can help us to describe if the system is described by the Necklace model or the Coalescense model.

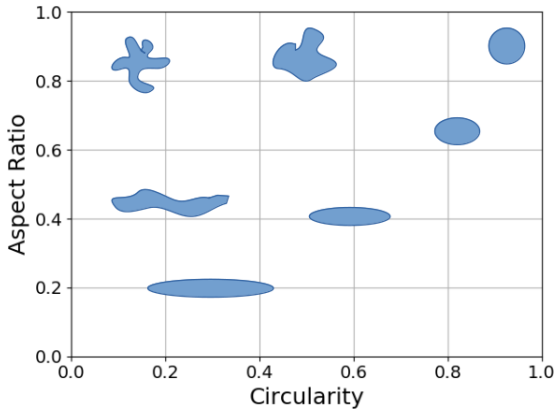

Figure 1.13: Scheme of possible aspect ratios and circularity.

Here it is indicated what kind of shape is expected for a nanoparticle according to the value of aspect ratio and circularity that posses.

1.3.4 FeRh nanoclusters

Liu et al studied B2 phase FeRh nanoparticles with sizes between 6 nm to 10 nm by magnetron co-sputtering over amorphous alumina ($\alpha - Al_2O_3$) finding on field cooling/zero field-cooling a ferromagnetic behaviour superparamagnetic-like. HAADF-STEM image over a nanoparticle was used to determine that some faces Rh-terminated (Figure 1.14). They conclude that the Rh-terminated (100) surface is in favor of an enhanced polarization of Rh that favors a ferromagnetic shell.

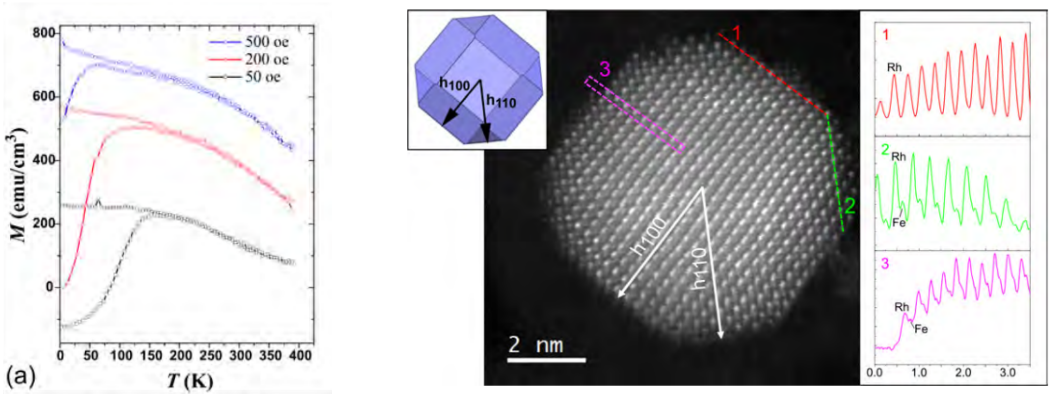

Figure 1.14: FC/ZFC and HAADF-STEM for FeRh nanoparticles in alumina matrix.

FC/ZFC (left) for FeRh nanoparticles in alumina matrix and HAADF-STEM (right) over one of the nanoparticles and profiles in different regions of the nanoparticle.

Loving et al report FeRh nanoisland of 100 nm diameter and 15 nm height over MgO. Their results indicate a huge residual ferromagnetic component at 0.1 T for magnetization as function of the temperature curves. They justify that the surface of the FeRh island are in favor of a ferromagnetic regime giving the residual ferromagnetic component (Figure 1.15).

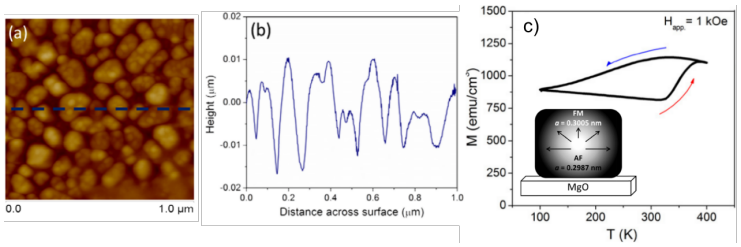

Figure 1.15: FeRh nanoisland and its metamagnetic transition

Atomic force microscope image of FeRh nanoislad on MgO (a) and the respective line profile (b) with its magnetization as function of the temperature for 0.1 T. On the insert the scheme used by [46] to indicate the ferromagnetic regime at surface and antiferromagnetic regime at the core.

Yu Yu Ko et al studied Fe_XRh_{100-X} nanoparticles between 10 nm and 15 nm after annealing at 600 °C for 6 hours, for different relative concentration. In particular for $x = 39$ that correspond to atomic 39% of Fe, it was found that the magnetization decreases as it is heating up and then follows the shape of a broad metamagnetic transition [47] (Figure 1.16). Is important to notice that according to the phase diagram for FeRh, the antiferromagnetic phase should not be stable at any temperature for 39% of Fe revealing that the phase diagram of the bulk (Figure 1.2) is not comparable to the one for nanoparticles.

In the case of chemically ordered FeRh nanostructures, the presence of the metamagnetic transition indicates strong hybridization between both components that increases magnetic moments for high temperatures. Nevertheless, the mechanisms that govern the metamagnetic transition are still not cleraly known. In the case of nanoparticles, is possible to control the density, and so the dipolar interaction between nanoparticles as a suplementary parameter. Hillion et al. already studied mass selected FeRh B2 phase nanoparticles lower than 5 nm in diameter embedded in carbon matrix with a 7% surface concentration where the ferromagnetic behavior persistence has been observed up to 3 K and a superparamagnetic behavior with a blocking temperature around T_{max} =12 K for 3 nm nanoparticle diameter [48].

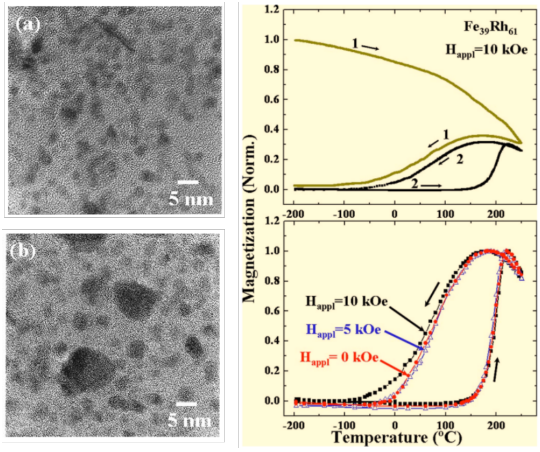

Figure 1.16: FeRh nanoparticles and metamagnetic transition

On the left $Fe_{36}Rh_{64}$ nanoparticles before (a) and after (b) annealing at 600 °C. On the right megnetization as function of the temperature for $Fe_{39}Rh_{61}$ incoming to the main branches at 10 T and in the main branches for 0 T, 0.5 T and 1 T.

1.4 Hybrid multiferroic systems

A *multiferroic* corresponds to a system that uses two or more ferroic properties, and we refer to a *Hybrid multiferroic* when it corresponds to a system with more than one phase with different ferroic properties. On this thesis we will be interested in the magnetoelectric hybrid multiferroic that correspond to the incorporation of ferroelectricity and magnetism in one system [49, 50] (Figure 1.17).

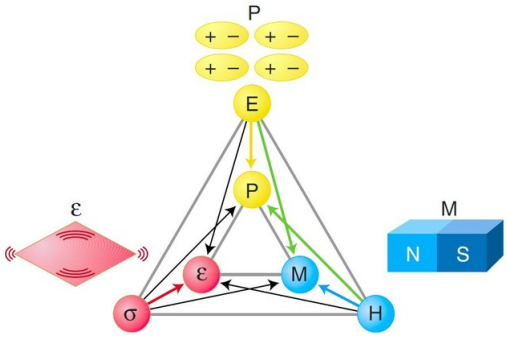

Figure 1.17: Diagram of a multiferroic.

The electric fielc E, magnetic field H and stress σ control the olarization P, magnetization M and strain ϵ respectively. Image extracted from [50]

The magnetoelectricity can be achieved by many methods as the creation of new materials, composites of element carrying each ferroic property of systems that

have interfaces between a ferroeleastic or ferroelectric and ferromagnetic material.

1.4.1 Perovskites oxides

One interesting candidate to form a multiferroic along FeRh are the perovskites, these are ABO_3 oxide compounds that adopt a cubic *perovskite structure*. This name comes from the mineral *perovskite* $C_aT_iO_3$ which crystallizes into a cubic cell with five atoms [51, 52], with the atom A as reference in the corners, the B atom at the center and the oxygen O atoms at the center of the faces (Figure 1.18).

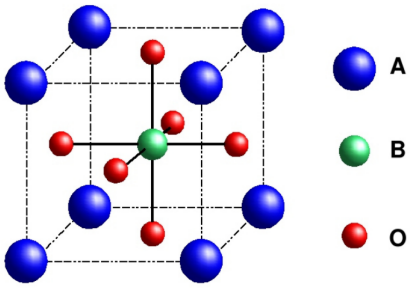

Figure 1.18: Schematic of the crystalline cell for a ABO_3 perovskite

Barium titanate (BTO)

Barium titanate $BaTiO_3$ (BTO) is a perovskite that exhibits a ferroelectric (FE) with three phase transitions [53] from cubic cell at high temperature to tetragonal cell at T_C =383 K [54], then from tetragonal cell to orthorhombic cell at T_C =278 K [55] and from orthorhombic cell to rhombohedral phase at T_C =183 K [56] (Figure 1.19).

Besides the phase transition the tetragonal phase of BTO posses the Ti shifted in the [001] direction causing the appear of ferroelectricity (FE) along that direction [57]. This means that the BTO in the tetragonal phase posses an spontaneous electric field along the [001] direction and can be switched by an external electric field, this property could be important for non-volatile devices [58–60].

Stronsium titanate (STO)

Stronsium titanate $SrTiO_3$ (STO) is a paraelectric cubic perovskite that at temperature below 105 K becomes tetragonal, non polar and antiferrodistorsive [61], that corresponds a shift of the oxygen atoms to the vertex alternating the shift direction (Figure 1.20).

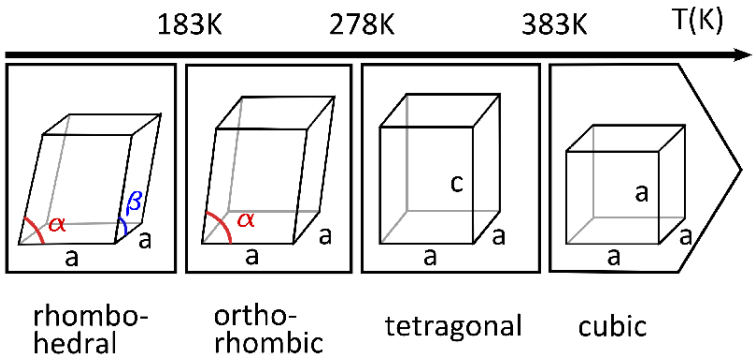

Figure 1.19: Crystalline phase transition of Barium titanate (BTO)

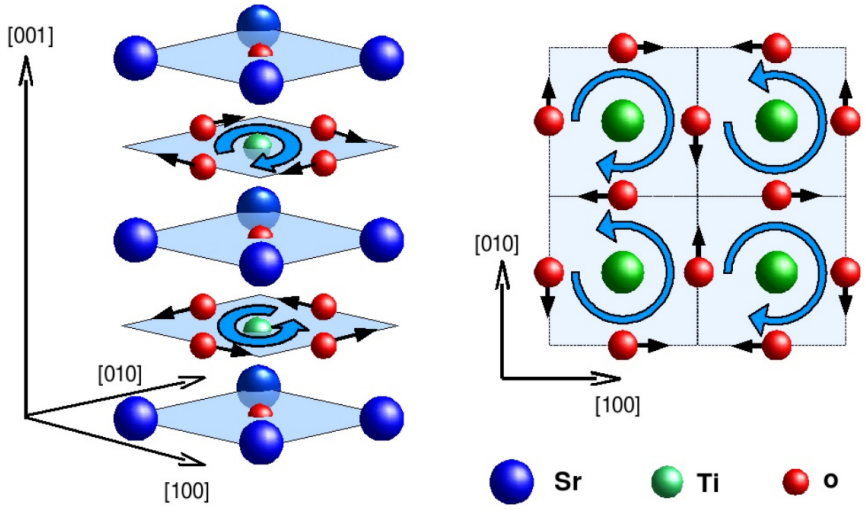

Figure 1.20: Antiferrodistorsive oxygen displacement on STO.

1.4.2 Studies of FeRh metamagnetic control

One posibility of the a multiferroic system is the control of the magnetic materials by applying voltage over the ferroelastic/ferroelectric material, some explored cases consist in a strain induced changes in the magnetic properties when voltage is applied over BTO as explored by *Cherifi et al.* They prepared a 22 nm FeRh film over BTO with electrodes to apply up to voltage 21 V finding that the metamagnetic transition is shifted to hight temperatures regardless the direction of the potential applied, even when no voltage is applied there is a difference of the metamagnetic transition depending if it was exposed to voltage indicating that the polarization of BTO can made a stable modification on the metamagnetic transition (Figure 1.21) [11].

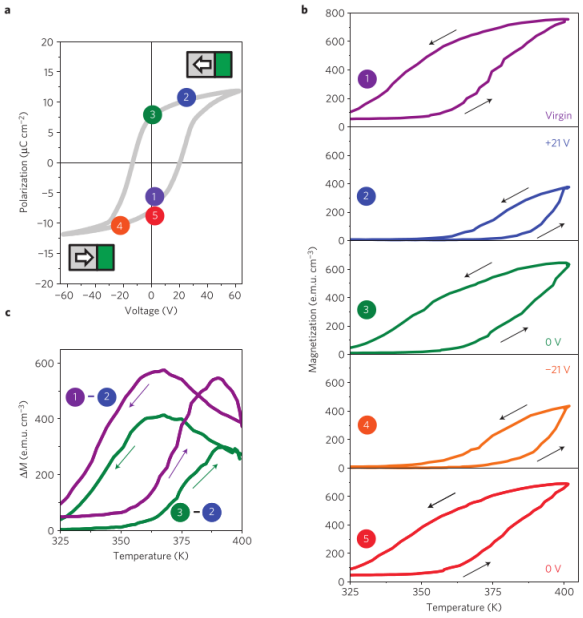

Figure 1.21: Magnetization for FeRh/BTO under voltage

Hysteresis loops for different temperatures inside the 'magnetization as function of the temperature loop' (insert) for a 150 nm FeRh film done by sputtering over MgO [11]

In order to explore strain effect *Chen et al* create a 25 nm FeRh film over BTO(001) and annealed it at 923 K achieving a B2 phase in epitaxy. They observed the FeRh metamagnetic transition of FeRh. But at temperatures that correspond to the phase transition of BTO is noticeable that there is a not dominant but sharp change in the magnetization value observed (Figure 1.22) [62].

Bennet et al explore a similar system of 25 nm FeRh film over BTO(001) where the dependence of the magnetic moment of FeRh with the BTO phase transition is also observed but, in addition polarized neutron reflectivity was used to see the magnetization at different depth revealing that the surfaces remain ferromagnetic and the region between 20 nm and 120 nm away the surface posses most of the metamagnetic transition (Figure 1.23) [63].

Is important to take in consideration that there is different factors that can be explored to modify the FeRh metamagnetic transition beside multiferroic systems. One example is the work done by *Jiang et al* where HfO_2 were placed over a 5 nm FeRh film, using a ionic liquid gate oxygen ions move from HfO_2 to the FeRh for positive voltage and return for negative potential. Is observed that as the voltage is bigger the metamagnetic transition become more bulk-like but for negative voltages the metamagnetic transition become wider and the transition

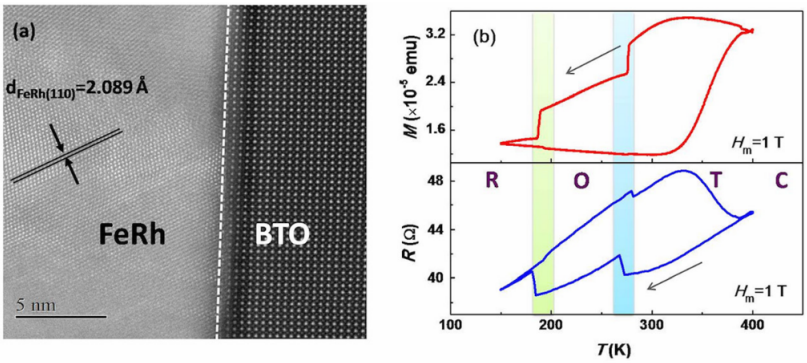

Figure 1.22: Hysteresis loops for FeRh film over MgO

On the left STEM-cross section image of FeRh over BTO and on the right the magnetization and resistance versus temperature with the regions of the phase transition of BTO marked as light blue strip (tetragonal to orthorhombic) and green strip (orthorhombic to rhombohedral) [62]

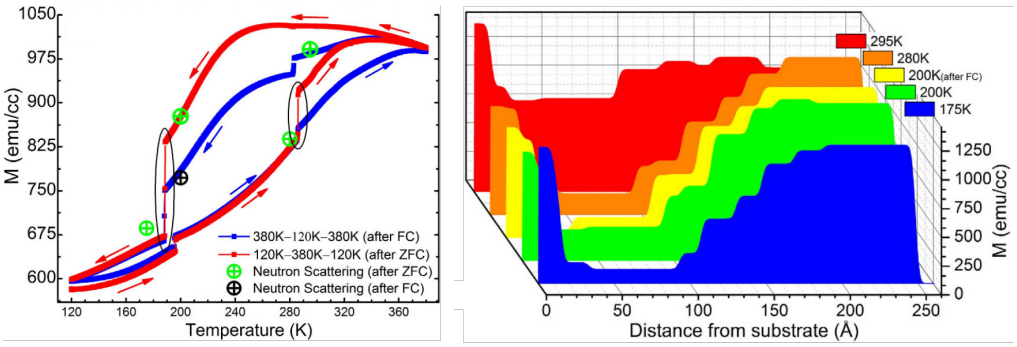

Figure 1.23: FeRh magnetic moment at different depth and temperature

Field cooling/ Zero field cooling for 1 T (Left) and magnetic moment at different temperatures and depth obtained with polarized neutron reflectivity (right) for 25 nm FeRh film over BTO [63].

temperature decreases (Figure 1.24) [64].

The work of *Jiang et al* is a proof that the metamagnetic transition is dependent of the oxidation, so it is important to consider potential changes on FeRh due to oxidation.

1.4.3 FeRh and oxidation

Papaefthimiou et al studied different 5 nm size Fe-metal nanoparticle alloys including FeRh. They observed a segregation when the nanoparticles are annealed at

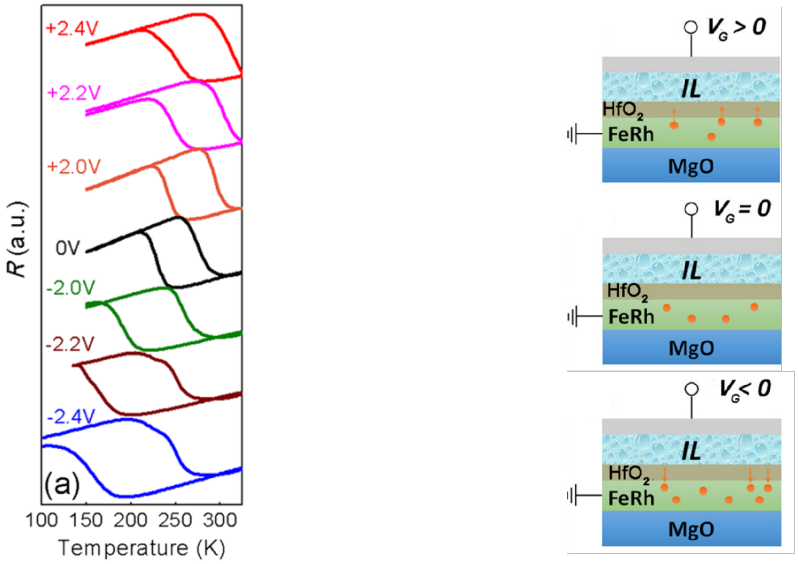

Figure 1.24: FeRh metamagnetic transition with O_X dopping.

FeRh metamagnetic transition under different voltages applied (left) and a schematic of the system used by *Jiang et al* to control O_X dopping with voltage (right) [64].

250 °C with partial atmosphere of O_2 0.2 mbar forming a Fe_XO_{1-X} shell, and after annealing at 400 °C with H_2 0.2 mbar then the nanoparticles have a Janus configuration (complete segregation of each element in opposite side) and the Fe_XO_{1-X} get partially reduced [40].

1.4.4 FeRh research

These properties make FeRh interesting to be explored for magnetocolorics, transport control valves, multiferroics applications. In addition, the exploration of low dimensional systems gives to FeRh a great interest for the scientific community, increasing the number of publications that mention FeRh by a factor four in the last ten years [65] following an exponential tendency (Figure 1.26).

1.5 On this thesis

This thesis is part of the project VOLtage COntrol of NANOmagnets (VOLCO-NANO) of the *Agence nationale de la recherche*, the aim is to study the changes in FeRh nanoparticles on perovskite substrate when a voltage is applied. The lattice modification by ferroelasticity, the surface polarization by ferroelectricity and the

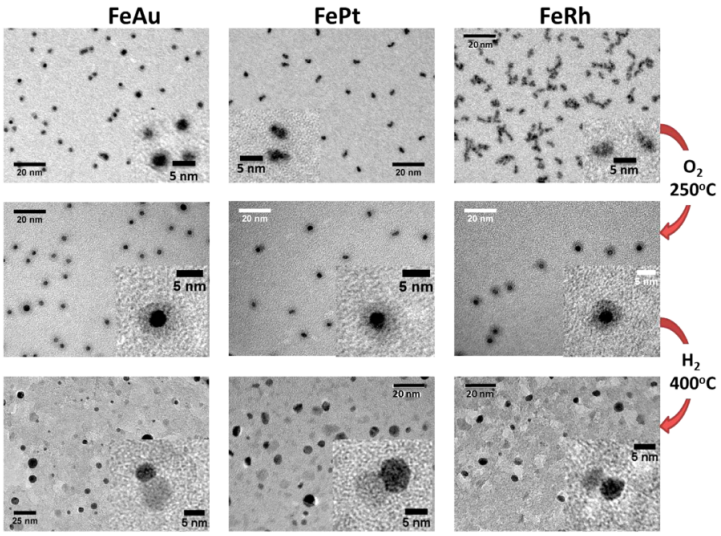

Figure 1.25: Fe-Metal nanoparticles for Au, Pt or Rh as the metal at different steps of segregation.

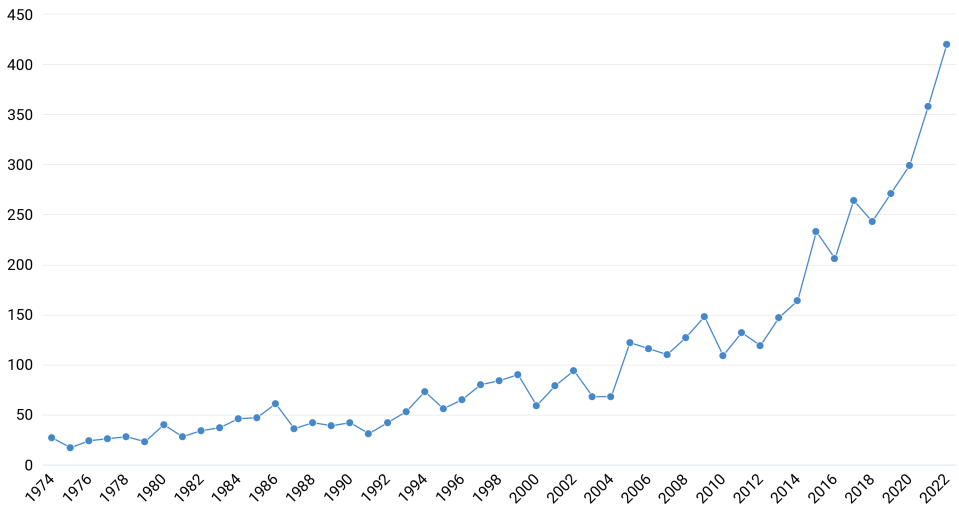

Figure 1.26: Number of publications that mention FeRh.

Number of publications that mention "FeRh" or "ion-rhodium" on its free access text per year. Plot extracted from *Dimensions*® [65].

phase transition in pevoskites may induce strain or effective potential in the FeRh nanoparticles that could modify their metamagnetic transition.

This goal requires several steps: First of all is necessary to have a magnetic, crystallographic and morphological intrinsic description of the FeRh nanoparticles

embedded in an inert matrix. Because in the past, Hillion shown that a persistent ferromagnetic state was observed up to 2 K for mass-selected B2 FeRh nanoparticles with size of 3 nm diluted in amorphous carbon matrix [66]; so as a continuation in this thesis, are explored larger FeRh nanoclusters with 7 nm of monomer and higher density of nanoparticles up to 20% of surface occupation to achieve bigger nanoparticles by coalescence upon annealing (chapter 4).

The creation of a thick film was a necessary step to prove the existence of FeRh metamagnetic transition for samples prepared by *LECBD* technique. Moreover, due to the specificity of films done by this technique, which leads to the formation of very porous samples, it has been possible to explore the FeRh films properties differences between reported films done by conventional atomic techniques and an assembled nanocluster film presently prepared by *LECBD* (5).

After well-knowing the magnetic properties of FeRh nanoparticles in inert matrix, and the behavior of FeRh in high surface/volume ratio system with metamagnetic transition, then it has been possible to enter in the purpose of the VOLCONANO project and to compare how the properties of FeRh nanoparticles change when they are in interaction with an oxide perovskite substrate; by exploring if this system posses epitaxial relationships and what changes may the epitaxy does over the magnetic properties.

Chapter 2

Experimental techniques

2.1 Substrate preparation

On this thesis different (001) substrates have been used; BTO/STO, STO, NbSTO (i.e Nb-doped STO) and Silicon wafer. The different treatment to prepare each substrate was:

- STO and NbSTO where under ultrasound bath on acetone for 2 minutes, then Buffered oxygen etching (BOE) and finally annealed at 1100 °C for 2 hours at air.
- BTO 7 nm layer were deposited by radio frequency sputtering in an ambient of 75% Argon and 25% Oxygen at 2×10^{-10} mbar.
- Silicon substrates were not treated.

The above cleaning treatment of the substrates is performed *out* the chamber of sample preparation. But before clusters deposition in the UHV chamber, the STO, NbSTO and BTO/STO samples were systematically pre-annealed *in situ* at 400 °C for 30 min.

2.2 Sample preparation

The *Plateforme Lyonnaise de Recherche sur les Agrégats* (PLYRA) is a setup at the Université Claude Bernard Lyon 1 that allows the deposition of nanoparticles preformed in gas phase, this technique is called *Low energy cluster beam deposition* (LECBD). This bottom up synthesis technique corresponds to a pulsed laser

beam (Nd:YAG with wavelength $\lambda = 532$ nm, frequency of 20 Hz and 8 ns of duration) that vaporizes the surface of an alloy rod made of the material desired as nanoparticles (equiatomic FeRh for the purpose of this work). By using laser vaporization, we conserve the stoechiometry of the rod (used as target) moved in helicoidal motion. A 30 mbar partial pressure of He gas is constantly present in a cavity which induces the nucleation of the nanoparticles in the cluster source (Figure 2.1).

A retractable quartz valance can be positioned in the cluster beam path allowing to measure the rate of deposition. And it is possible to put a substrate in the path of the beam after the quartz balance to deposit in UHV nanocluster preformed in gas phase.

It is possible to include mass selection of the nanoparticles by a technique called *Low energy cluster beam deposition - mass selected* (LECBD-MS) by incorporating an electrostatic quadripole deviator. The deviator consists in four electrodes of the same hyperbolic geometry polarized alternatively $\pm U$ and coupled with horizontal and vertical slit lenses for beam shaping.

The speed v is determined for the partial pressure and the mass m of the material used, while the charge typically is one electron per nanoparticle. The diameter of the nanoparticle can be obtained assuming a spherical nanoparticle shape and a density ρ (eq. 2.2).

In this way, as an approximation, we can consider a nanocluster speed of 600 m/s, spherical shape and the density of FeRh bulk in non chemically ordered A1 phase 10.11 $\mathrm{gr/cm^3}$ (ICDD 04-004-5204) to obtain a nanoparticle size of 3.7 nm using 300 V.

$$E_{electrostatic} = E_{kinetic} \rightarrow qU = \frac{mv^2}{2} \rightarrow m = \frac{2qU}{v^2} \tag{2.1}$$

$$\frac{\pi D^3}{6} = \frac{m}{\rho} \rightarrow D = \sqrt[3]{\frac{12qU}{\pi v^2 \rho}} \tag{2.2}$$

The amount of nanoparticles deviated by the quadripole actually corresponds to a small fraction of the cluster beam, this make necessary an additional measure of mass deposited per time. A Faraday cage is on the same axis of the sample holder, rotating the axis allow to deposit the mass selected cluster beam on the Faraday cage instead of the substrate. The Faraday cage of area A_{Cage} registers an average current I corresponding to N nanoparticles, each with one electron of charge q, arriving on a time of deposition t. Then it is possible to determine the equivalent thickness h for a selected size D as indicated in the eq. 2.4.

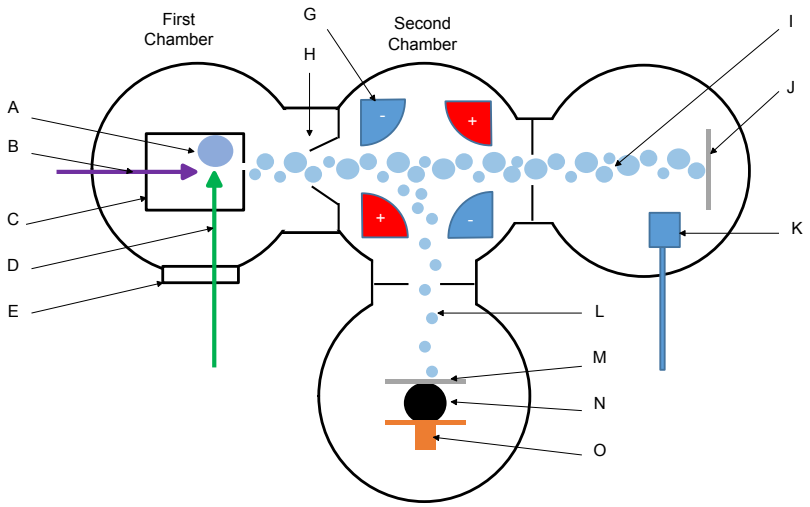

Figure 2.1: Scheme of PLYRA.

(A) FeRh rod, (B) incoming He gas, (C) cavity at 30 mbar, (D) nd:YAG LASER, (E) window, (G) quadripole, (H) Skimmer, (I) non mass selected cluster, (J) substrate for non mass selected cluster beam, (K) quartz balance retracted, (L) mass selected cluster beam, (M) substrate for mass selected cluster, (N) axis to rotate substrate and Faraday cage and (O) the Faraday cage.

$$I = \frac{Nq}{t} \ , \ h = \frac{NV_{nanoparticle}}{A_{Cage}} \ , \ V_{nanoparticle} = \frac{\pi D^3}{6} \tag{2.3}$$

$$\rightarrow h = \frac{It\pi D^3}{6qA_{Cage}} \tag{2.4}$$

As an example, by measuring an average current of I =10.95 $\times$ 10^{-10} A on a Faraday cage with 6 mm in diameter ($A_{cage} = \frac{\pi}{2}36\,\mathrm{nm}^2$), for ionized nanoparticles with D_1 =3.7 nm in diameter deviated by 300 V in the quadripole, an equivalent thickness of h =5.4 Å is expected after t =140 minutes of deposition, leading to a total amount of D_1 per area that arrived on the Faraday cage, equal to $\sim$20 306 N/μm^2. In this case, by calculating the number of nanoparticles N from 2.4 and considering no stacking neither coalescence, then the relative occupied area by deposited nanoparticles ($A_{occupied\%} = N * A_1/A_{cage} = 100 * ND_1^2/36mm^2$) corresponds to 21% of surface occupation which is the 2D threshold edge for random clusters deposition [67].

On the table 2.1 is shown different size, surface occupation and equivalent thickness. The controlled parameters are typically the deposition time t and the deviation voltage while the velocity v is set from previous measurements on other samples.

Voltage (V)	time (min)	I (pA)	v (m/s)	D_1 (nm)	h (Å)	S (%)
1200	65	5	400	7.7	10	20
1200	32	5	400	7.7	5	10
1200	6.5	5	400	7.7	1	2
1200	3.2	5	400	7.7	0.5	1
300	144	10	600	3.7	5	20
300	72	10	600	3.7	2.5	10
300	14.4	10	600	3.7	0.5	2
300	7.2	10	600	3.7	0.25	1

Table 2.1: Possible configurations of samples

For certain voltage, time, current on the Faraday cage (I) and nanocluster speed (v) the resulting monomer size (D_1), equivalent thickness (h) and surface ocupation (S).

It is possible to have nanoparticles sintering before mass selection, since the nanoparticles are hot when they leave the rod, the thermal energy will allow coalescence in fly and get a spherical shape. If we consider that nanoparticles of initial radius r_0 get coalesced with other particles of size r_0 between intervals of time t_{col}, will form a bigger spherical nanoparticle that get cooler and eventually get cooled after a time t_s at a critical radius r_c and it can not longer achieve a spherical shape, leading to irregular shape after several coalescing [68] (Figure 2.2). This indicates that is expected to have irregular shapes for big monomer after mass selection but also indicates that for different materials is possible to obtain different monomer shapes as the r_0, r_c and t_s may be different.

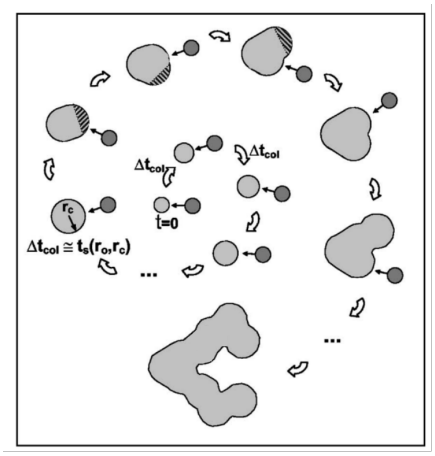

Figure 2.2: Nanoparticle coalescence on the fly

Scheme of on the fly coalescence for spherical monomer of radius r_0 and time interval between coalescence t_{col}, where for a radius r_c after a time t_s the nanoparticle can no longer achieve a spherical shape (Image adapted from [68]).

The distribution of nanoparticle size before the mass selection corresponds to a wide log-normal distribution and after the mass selection corresponds to a gaussian distribution with deviation of around 10% of the mean size (See Figure 2.3).

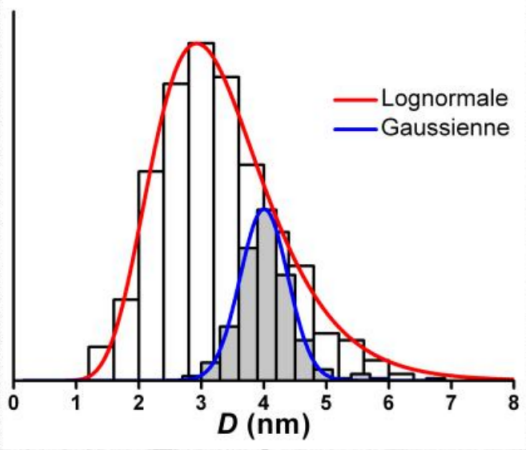

Figure 2.3: Size distributions achieved in PLYRA

Size distribution with (experiment in grey and gaussian fit in blue) and without (experiment in white and lognormal fit in red) mass selection

2.3 Superconducting quantum interference device (SQUID)

The SQUID (Superconducting QUantum Interferometer Device) measurements in this thesis are done in the *Transport ILM Tech* platform. The apparatus is a MPMS-XL5 SQUID from Quantum Design This device allows to measure samples having very small magnetic moment, typically in the order of $10^{-5}\,\mathrm{A/m^2}$. The MPMS-XL5 SQUID allows for temperature control between 2 K and 400 K and applied magnetic field from $-5\,\mathrm{T}$ up to $5\,\mathrm{T}$ [69]. The reciprocating sample option (RSO) oscillates the sample around the measuring point allowing rapid and precise measurements with a narrow flux level of $10^{-9}\,\mathrm{A/m^2}$ (Figure 2.4).

The sample is oscillating inside a superconducting coil L_1, as long the sample has magnetic moment the oscillation will produce a variation of magnetic flux through the picking coil inducing an electrical current. Notice that any time independent component of the magnetic flux do not produce induced current avoiding to measure the applied magnetic field. Also the coil L_1 is made of two coils with opposite direction on the extremes to sharpen the sensibility of the sample position detection.

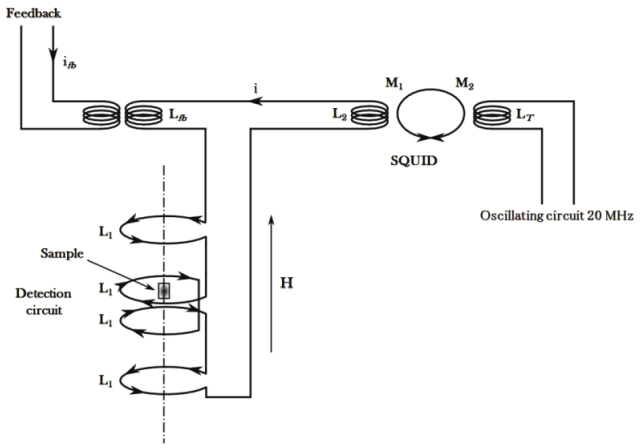

Figure 2.4: Scheme of a SQUID

Scheme of a SQUID with i_{fb} the feedback current induced over the inductance L_{fb}, i the current in the close loop, L_1 the coil around the sample, L_2 the coil that induce field over the SQUID mechanism, and L_T the coil that produce the current measured.

The induced current passes through a second coil L_2 that induces magnetic flux over the SQUID, which corresponds to a superconducting ring with one Josephson junction (RF-SQUID). Since it corresponds to a closed loop the phase difference ψ at each side of the Josephson junction must be 2π to maximize the induction.

$$\Phi_0 = \frac{2\pi\hbar}{2e} \tag{2.5}$$

$$\psi = -2\pi\frac{\Phi}{\Phi_0} \tag{2.6}$$

The induction on the SQUID will be higher if there is no phase ($\psi = 2\pi n$) and so $\Phi = n\Phi_0$ and it will be minimum for $\Phi = \Phi_0(2n+1)/2$. The variation of inductance is measured by a circuit connected to L_T. The system operates at maximum conductance on the SQUID, if it decreases due to the additional current produced by the sample magnetic field then a feedback current on L_B compensate this difference, the feedback current is the value used as indirect measure of the sample magnetic field [70].

2.4 Transmission electron microscopy (TEM)

The transmission electron microscopy consists in a technique where an electron beam passes through the sample. After interaction with the sample, the transmitted beam can be collected to identify structure and chemistry regions at nanoscale. The spatial resolution detection of a wave is typically half of the wavelenght.

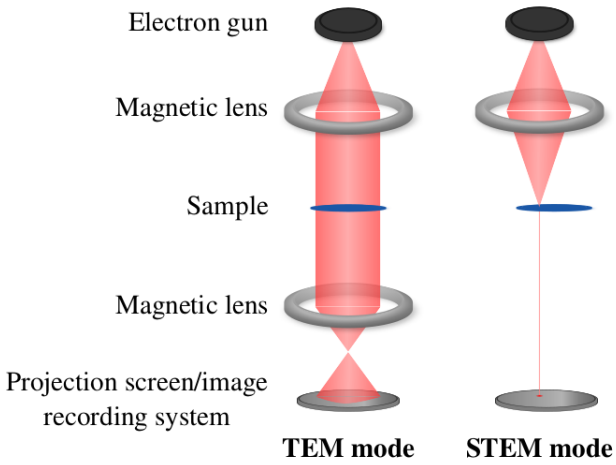

Figure 2.5: Scheme of a TEM and STEM

For the beam to transmit through the specimen, the latter must have low thickness, typically less than 100 nm. In the case of nanoparticles, they can be deposited over a carbon-coated copper grids called *TEM grids*. For nanoparticles epitaxied on STO, cross-section specimens have been prepared by focused ion beam milling, allowing to see the contact between nanoparticles and substrate.

In TEM mode, a parallel electron beam illuminates the sample, while in scanning TEM (STEM) mode, the electron beam is focused on the specimen. In STEM, the electron beam scans the surface of the sample, and the elastically-scattered electrons are collected in an annular detector.

Energy-Dispersive X-ray spectroscopy (EDX) corresponds to expose the sample to a source of energy (electron beam) and it will dissipate energy as X-rays. Each element posses a specific EDX spectrum of X-ray allowing identify which ones are in the region exited.

When the fast electron beam interacts inelastically with the sample, the de-excitation of the atoms in the sample can occur through the emission of X-rays, which can be collected by Energy-Dispersive X-ray spectroscopy (EDX).

For the STEM configuration heavier elements lead to a stronger electrostatic

interaction between the nucleus and the fast electron resulting in a higher scattering angle. This dependence of electron scattering as a function of the Z number is used to identify elements in the sample, this technique is called high angular annular dark field (HAADF) (Figure 2.6).

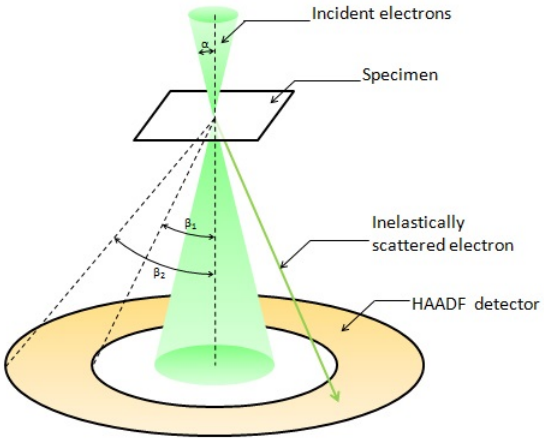

Figure 2.6: STEM-HAADF imaging mode

On this thesis STEM-HAADF images were collected on a JEOL JEM ARM 200-F (NeoARM), equipped with a cold-field emission gun and an aberration corrector (CEOS ASCOR) of the condenser lenses.

To process the images python scripts were used. STEM images were imported with the *hyperspy* library and the atoms positions were identified with the *atomap* library. While TEM images were treated on *ImageJ* to get the binary version, detect the nanoparticles and export the data analyzed with a python program, the binary image is also used imported with the *PIL* library to obtain the minimum distances to nearest neighbor of a nanocluster.

2.5 X-ray techniques

X-ray techniques can be used to study sample composition and cristallinity. In this work we used spectroscopy techniques as X-ray Photoelectron Spectoscopy (XPS), X-ray Absorption Spectroscopy (XAS) and X-ray magnetic circular dichroism (XMCD) as well X-ray diffractometry (XRD) including Grazing Incidence Wide Angle X-ray Diffraction (GIWAXS) and Graizing Incidence Small Angle X-ray Diffraction (GISAXS). On lab were performed XPS and XRD measures, while in synchrotron facilities were performed XAS, XMCD, XRD, GIWAXS and GISAXS.

Each material posses a specific potential energy to release electrons from its core levels. When an electron is ejected, if it has enough energy to surpass the work function it will go outside the sample. If it is not emitted outside, since is not bounded to a core level can be transported over the sample as current as long the sample has conduction states (metallic or induced conductivity), or can descend to a lower core level and emit a X-ray.

2.5.1 In lab techniques

For chemical characterization is important to see what is measure, if the incoming X-rays do not bring enough energy to release electrons of certain levels then electrons and their associated emissions will not me measured (Figure 2.7). In these terms we can separate the X-rays techniques used on this work on the ones that used a source of x-ray that correspond to a specific emission of a material (in-lab techniques) and the ones performed on synchrotron facilities.

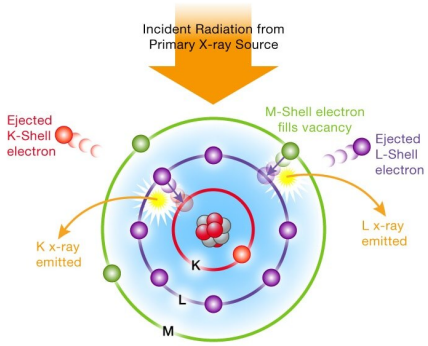

Figure 2.7: Scheme of interactions of X-ray/electrons interactions

X-ray photoelectron spectroscopy (XPS)

X-ray photoelectron spectroscopy (XPS) corresponds to the measurement of the electrons emitted by the sample when exposed to incidence X-ray. The kinetic energy of the electron E_K will be determined by the energy it received from the X-ray $h\nu$, less the energy to leave the core level called binding energy E_B and less the energy necesary to leave the sample knowed as the work function Φ (See eq. 2.7).

$$E_K = h\nu - E_B - \Phi \tag{2.7}$$

A Hemispherical electron energy analyzer allows to measure the relative amount of photoelectrons for each E_K, this detector correspond to electric lenses to slows down the incoming electrons, a capacitance that deflect the trajectory of the electrons and a electrons detector at the end (There is many shapes that allow this but in this work is used a hemispherical analyzer). For a specific potential applied in the capacitance only the electrons in a certain range of E_K will have the deviation necessary to arrive to the detector, this way is possible to count the electrons for different ranges of E_K (Figure 2.8)

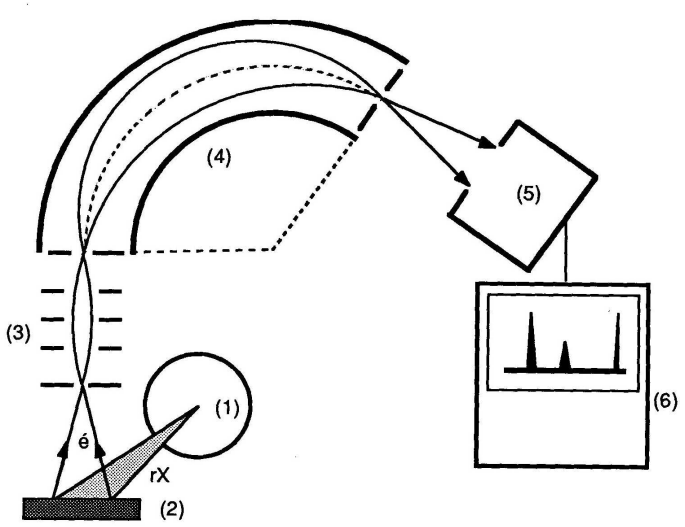

Figure 2.8: Scheme of interactions of a XPS

(1) Source of X-rays (2) Sample (3) electric lenses (4) capacitance (5) electron detector and (6) acquisition program

X-ray diffraction (XRD)

This technique corresponds to a beam of x-ray (that for our case, it will correspond to the Cu K-α emission of 1.54 Å wavelength) arriving to the surface of a crystal to study. The x-rays that reflect with a plane of the crystal will interfere with the ones reflected in a parallel plane, the angle of reflection will determine if the interference is constructively or destructively resulting in many beams that give the name diffraction to this phenomena (from Latin *diffractus) "to shatter, to break into pieces"*. The *Bragg law* correlates the x-ray wavelength λ, the angle of diffraction θ an the inter-planar distance d (Figure 2.9).

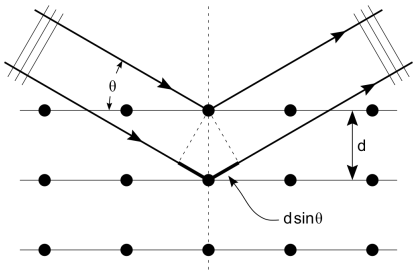

Figure 2.9: Scheme of x-ray diffraction

A specific crystal lattice has a set of different parallel planes, so it will diffract in a specific angles allowing to reconstruct the crystal cell using the angles of refraction θ and the x-ray wavelength λ.

2.5.2 Synchrotron techniques

When charged particles at relativistic speed (very close to the speed of light) experience a change of velocity (as when they are forced to rotate under the effect of a magnetic field by Lorentz force), they emit photons which are more energetic as the particle goes faster. Synchrotron radiation is emitted when relativistic charged particles are subject to an acceleration perpendicular to their velocity ($\sim a \perp \sim v$). This radiation was discovered in 1947 in a General Electric laboratory in New York [71]. The synchrotron was then about thirty centimeters in diameter and the magnetic field was less than 1 T.

Nowadays, in an accelerator like the European Synchrotron Radiation Facility (ESRF) or the *Source Optimisée de Lumière d'Énergie Intermédiaire du LURE* (SOLEIL), electrons are injected into a Linear particle accelerator (LINAC) from which they join a second circular accelerator, the booster. When their energy is sufficient (a few GeV), they are then sent to the storage ring (Figure 2.10), which

is sometimes several hundred meters in diameter (113 m for SOLEIL, 269 m for the ESRF). Several injections from the LINAC and the booster are necessary to reach a sufficient current in the storage ring (a few hundred mA).

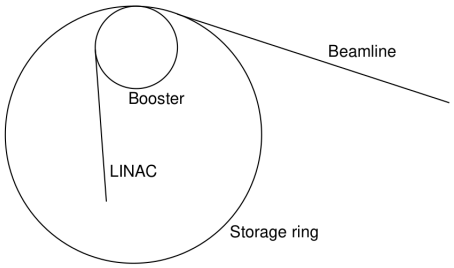

Figure 2.10: Scheme of Synchrotron

Block diagram of a synchrotron accelerator. A single beamline is shown here for clarity. In reality, many beamlines are arranged tangent to the storage ringm

Bending magnets and undulators (also called insertion devices) placed in the storage ring allow the emission of synchrotron radiation, recovered in beamlines where various optical devices (monochromators, polarizers, lenses...) allow the use of the X-rays produced. The rapid change of trajectory of the electrons by the undulators allows the emission of many photons (Figure 2.11).

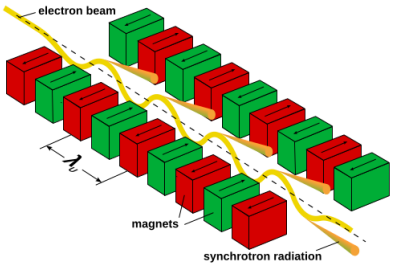

Figure 2.11: Scheme of an undulator

The electrons enter at the top left and are deflected many times by the magnets. At each deviation, photons are emitted.

DEIMOS beamline at SOLEIL synchrotron operates in the range 350 eV-2500 eV [72] while ID12 beamline at ESRF synchrotron operates in the range 2000 eV-15 000 eV [73]. Which element edges can be measured in which beamline depend on their x-ray absorption energy, as reported in the table 2.2.

Element	Edge	X-ray absorption Energy	Beamline
Fe	L3	707 eV	DEIMOS-SOLEIL
	L2	720 eV	DEIMOS-SOLEIL
	K	7112 eV	ID12-ESRF
Rh	M	307 eV	DEIMOS-SOLEIL
	L3	2967 eV	ID12-ESRF
	L2	3324 eV	ID12-ESRF

Table 2.2: X-ray absorption energies

X-ray absorption energies and the respective beamline where it can be measured for different edges of Fe and Rh [74].

X-ray absorption spectroscopy (XAS)

The X-ray absorption spectroscopy (XAS) as the name suggest is the measurement of the X-ray absorbed by the sample, that can be correlated with the current originated by emited electrons called total electron yield (TEY) or, the emitted X-ray when a electron decay to a lower level called fluorescence (FLUO) (Figure 2.7). TEY needs a conductive sample to measure the current.

X-ray magnetic circular dichroism (XMCD)

XMCD is a spectroscopy technique providing quantitative information on the magnetic properties through the analysis of circularly polarized x-ray absorption spectrum. Thanks to its chemical selectivity, its capacity to separate the orbital and spin moments and its high sensitivity, XMCD becames a reference technique in the 1990s to study thin films and magnetic multilayers [75–77].

The concept of the XMCD was first established in 1975 when mathematical calculations predicted the difference in the absorption of a polarized light as a function of the magnetization of Ni [78]. The first experimental realization was obtained twenty years later [79]. The general XMCD theory was only recently developed allowing direct and quantitative measurement of the spin and orbital magnetic moments [80, 81].

This technique consists in exposing the sample to circular polarized X-ray, to measure the electrons removed from core levels. The interaction between the polarized X-ray and the electrons adds an interaction potential that is lower if the electron magnetic moment is aligned with the X-ray polarization resulting in a difference of intensity in the X-ray absorption for circular right ($\mu+$) and circular left ($\mu-$) polarized X-ray.

In order to explain the treatment, first is necessary to establish certain values

(using the notation of Chen [82]):

- N_h is the number of 3d holes.
- μ_+ is the X-ray absorption for circular right polarized incoming X-ray
- μ_- is the X-ray absorption for circular left polarized incoming X-ray
- μ_0 is the X-ray absorption for non polarized incoming X-ray, and is the same as the X-ray absorption average of both polarized signals $\mu_0 = (\mu_+ + \mu_-)/2$
- q is the integral of the the difference between μ_+ and μ_- in the range of energy of the L core level $q = \int_L \mu_+ - \mu_- dE$
- p is the integral of the the difference between $\mu+$ and $\mu-$ in the range of energy of the L_3 core level $p = \int_{L_3} \mu_+ - \mu_- dE$. The ranges of the L_3 and L_2 are delimited by the minimum of μ_0 between this two peaks.
- w is the *white line* a double step function and the L_3 peak and L_2 peak with step hight of 2/3 and 1/3 of the difference of intensity between $L3$ pre-edge and $L2$ post-edge.
- r is the integral of the difference between μ_0 and w in the range of energy of the L core level $r = \int_L \mu_0 - w dE$

Then is possible to obtain the orbital magnetic moment m_{Orb} and the spin effective magnetic moment m_{Seff} by applying the sum rules in the following way:

$$m_{Orb} = -\frac{2q}{3r} N_h \tag{2.8}$$

$$m_{Seff} = -\frac{3p - 2q}{r} N_h \left(1 + \frac{7 \langle T_z \rangle}{2 \langle S_z \rangle}\right)^{-1} \tag{2.9}$$

The Tz term corresponds to the dipolar operator that has relevance for systems of $\sim$ 10 atoms but in bigger scales is neglected [83], leaving the expression for m_{Seff}:

$$m_{Seff} = -\frac{3p - 2q}{r} N_h \tag{2.10}$$

The calculation of the associated error for the XMCD measurements is indicated in Anexe A.

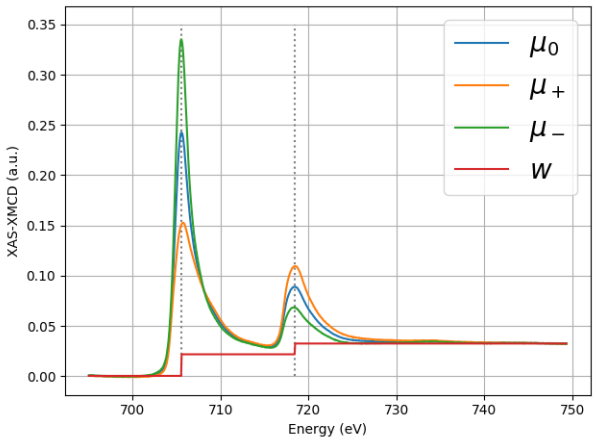

Figure 2.12: Spectres used for XAS/XMCD at Fe edge

Example of the and XAS/XMCD spectra with the average XAS μ_0 (blue), the polarized circular right μ_+ (orange) the circular polarized left μ_- (green) and the white line w (red). As a dashed lines are marked the L_3 and L_2 peaks used to stablish the steps in the white line.

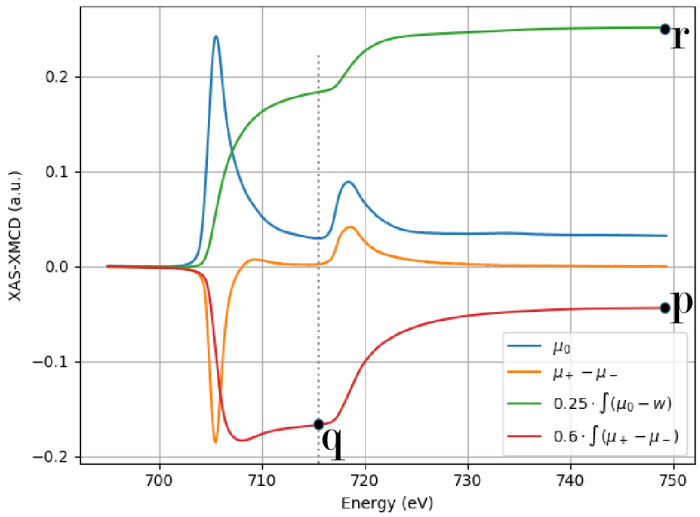

Figure 2.13: XAS/XMCD with their integrasl for Fe edge

Example of the and XAS/XMCD spectra with the average XAS μ_0 (blue), XMCD signal as $\mu_+ - \mu_-$ (orange), the integrals of the difference between the XAS and the white line $\int(\mu_0 - w)$ (green) and the integral of the XMCD signal $\int(\mu_+ - \mu_-)$ (red). The points r, p and q used for the sum rules are indicated as dots .Both integrals curves were multiplied by a factor for better visualization.

Grawing incidence x-ray difraction (GIXRD)

Grazing incidence x-ray diffraction share the same principles as the x-ray diffraction, by being grazing it implies that prove only the surface of the sample and it proves the in-plane crystalline orientations and higher energy beam allows better presicion. On the BM32 beamline at ESRF syncrotron facility is used x-ray at 1.58 keV that correspond to a wavelength of 0.78 Å.

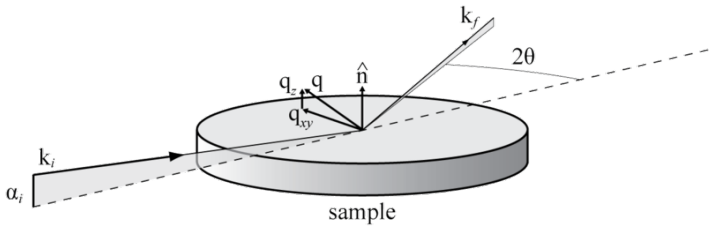

Figure 2.14: Scheme of GIXRD

Sheme of GIXRD. X-ray incoming to the substrate at vertical angle α_i and wave-vector k_1, the diffracted x-rays have an in plane angular deviation 2θ and vertical angle α_f and a wave-vector k_f. The change in the wave-vector after diffraction is due to the scattering vector q that can be decomposed to his in plane q_{xy} and normal to the plane q_z contributions

Is possible to reconstruct a map of the in plane using the intensity of the outgoing x-rays and the angle as radius, then rotating the sample to observe the diffraction pattern in different directions. Same way as XRD different patterns will implies different crystalline structure with the advantage that resolve in which direction is orientated the crystal (Figure 2.15).

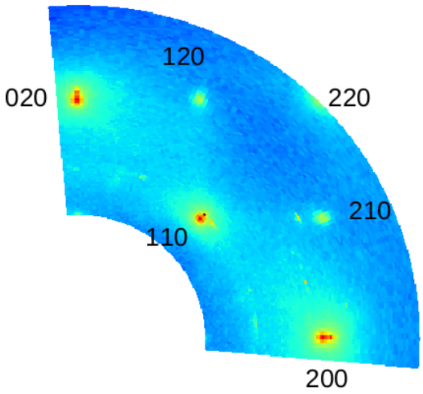

Figure 2.15: Example of in-plane GIXRD

Example of in-plane GIXRD. This correspond to STO(001).

Chapter 3

FeRh nanocluster in carbon matrix

This chapter corresponds to the characterization and properties of FeRh nanoparticles embedded in a carbon matrix. The objective is to probe the intrinsic quality of large FeRh nanoparticles and to see if it is possible to acieve the B2 phase necessary for a metamagnetic transition.

Hillion et al [48] explored a system of FeRh nanocluster a monomer size of 3 nm embedded in a carbon matrix, revealing a persistence of the ferromagnetic domain. In this chapter larger monomer sizes will be studied and two different densities will be explored in order to achieve a larger size by coalescence. This study requires a complete characterization of the samples (shape, distance ...) in order to determine how comparable they are.

3.1 Sample preparation

Samples of mass-selected FeRh nanoclusters with a nominal diamater of 7 nm were prepared by LECBD-MS (Section 2.2) on Si substrate. In order to study the size and distribution of supported nanoparticles, twin samples deposited on a TEM grid instead of Si (Section 2.4) were prepared with the same conditions of cluster deposition.

To see the effect of the magnetic interaction between nanoparticles, samples were prepared in pairs: one of the two with 0.1 nm of equivalent thickness, which will be referred to as low-density sample (LD), and the other one with 1 nm of equivalent thickness, which will be referred to as high-density sample (HD). All samples were covered with an amorphous carbon capping to avoid oxidation, as it was done by Hillion et al [48].

Both samples were annealed in an annexed furnace in UHV conditions at 700 °C for 3 hours in order to achieve the B2 phase. Size, distance and crystallinity were studied for annealed and non-annealed samples.

3.2 Crystalline phase

EDX measurements provided a first idea of the chemical concentration, since it has a limited resolution of 10%. This measurement indicates values for the atomic concentration fluctuating around Fe 50% Rh 50%.

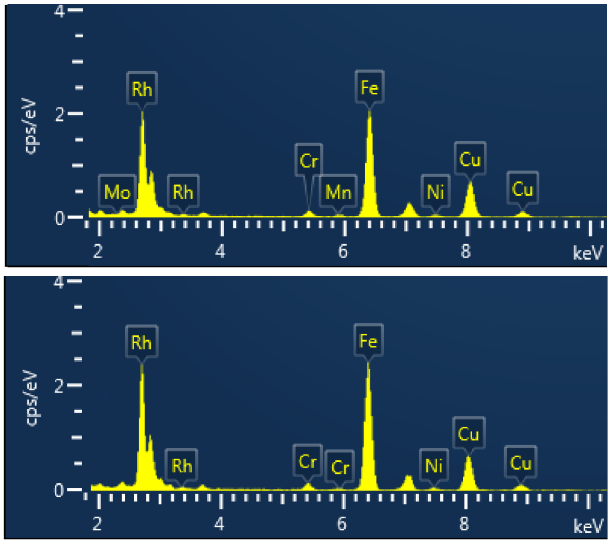

Figure 3.1: EDX for FeRh nanocluster in TEM grid.

EDX for a FeRh diluted nanocluster embedded in carbon matrix, with a relative atomic concentrations of Fe 47% and Rh 53% ±10% (top) and Fe 52% and Rh 48% ±10% (bottom).

High resolution TEM was performed on closer zoom to the nanoparticles in order to observe the crystalline lattice. In Figures 3.2 (a) and (c) we can observe the crystal planes for as-prepared and annealed nanoparticles, respectively, where it is possible to notice the roundness of the annealed nanoparticle and the homogeneity of the crystal domain.

Fast Fourier Transform (FFT) reveals the presence of the A1 phase in the as-prepared nanoparticle with 3.7 Å of lattice parameter and the B2 phase for the annealed nanoparticle with 3.0 Å of lattice parameter (Figures 3.2 (a) and (c) inserts). It is corroborated that the A1 phase is globally present in the as-prepared sample by the position of a diffuse diffraction ring observed by electron diffraction,

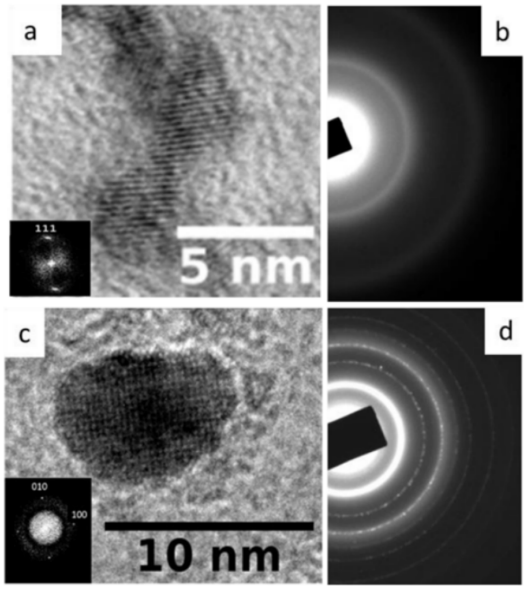

Figure 3.2: High resolution TEM and electron diffraction before and after annealing.

High resolution TEM image (a and c) with the respective fast Fourier transform inserted, and their electron diffraction rings (b and d) before and after annealing respectively.

the same way the B2 phase pattern is globally observed in the annealed sample (Figures 3.2 (b) and (d)).

On the diffraction rings for annealed FeRh nanocluster is possible to observe all the peaks corresponding to the FeRh B2 phase (Figure 3.3).

Then the question left to address is the FeRh concentration in the samples and whether it is really FeRh 50%/50%. The shown EDX results reveal a chemical nanoalloy composition varying from FeRh 52%/48% to the reverse 47%/53%, with a precision of 10%. The TEM and electron diffraction measurements of the B2 phase and lattice parameter indicate that these nanoparticles should be in a nearly equiatomic concentration. Moreover, one should not forget that for 7 nm nanoparticles, the surface atoms represent around 16% of the total (section 1.3), meaning that the nanoparticle chemical termination could give a wide range of concentrations. For samples with more matter, as the nanocluster assembled film presented in Chapter 4, this question will be addressed in a better way from RBS measurements, which give around 50%/50%±4% for the nanogranular FeRh thick film composition. Since all the samples are prepared with the same setup, one could extrapolate that any nanoparticle possesses the same mean Fe/Rh ratio.

Moreover, one can also underline the fact that the phase diagram for the bulk

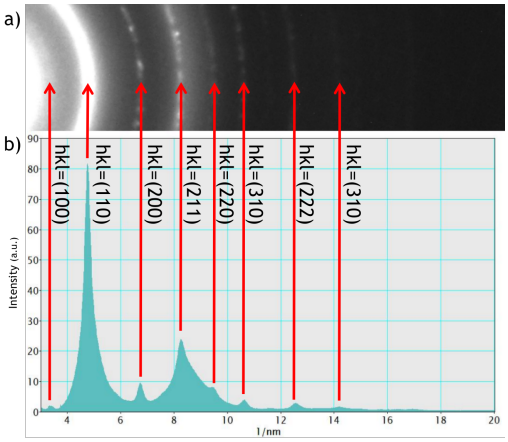

Figure 3.3: Diffraction rings for FeRh nanoclusters

Electron diffraction rings with intensity for FeRh nanocluster embedded in carbon matrix. On red arrows is marked the FeRh diffraction peaks and miller indexes reported in *ICDD 04-002-2003*

can not be fully extrapolated for bimetallic nanoparticles. As an example, in the work of *Yu Yu Ko et al*1.16 (presented on the Chapter 1 Figure 1.16) [47], a metamagnetic transition was observed for $Fe_{39}Rh_{61}$ nanoparticles concentration in the 10 nm and 15 nm size range, even if the phase diagram for the bulk indicates one should not expect any metamagnetic transition at that concentration. Thus, this Fe/Rh ratio is probably not so critical at nanoscale where concentration differences could be absorbed by core@shell morphology [84].

3.3 Size distribution

The size distribution is measured from TEM images (see TEM section) using the program *ImageJ* with the *Fiji* extension. First, a filter in the Fourier space is applied in order to remove and soften the noise in the nanoparticles boundary; Then, the nanoparticles that touch the edges of the image are removed. After saving each image in binary format, a custom *python3* program generates the histogram and fits a N-Gaussian curve for different values of histogram bin, in order to save the N-Gaussian fit and histogram bin with less discrepancy and minimize the error.

The histogram was divided into three groups: D_1 that corresponds to the bins in the monomers, D_2 which are the dimers, and D_{3+} which are the trimers or larger. This allows to know how many nanoparticles are in each group relative to the total amount of nanoparticles measured.

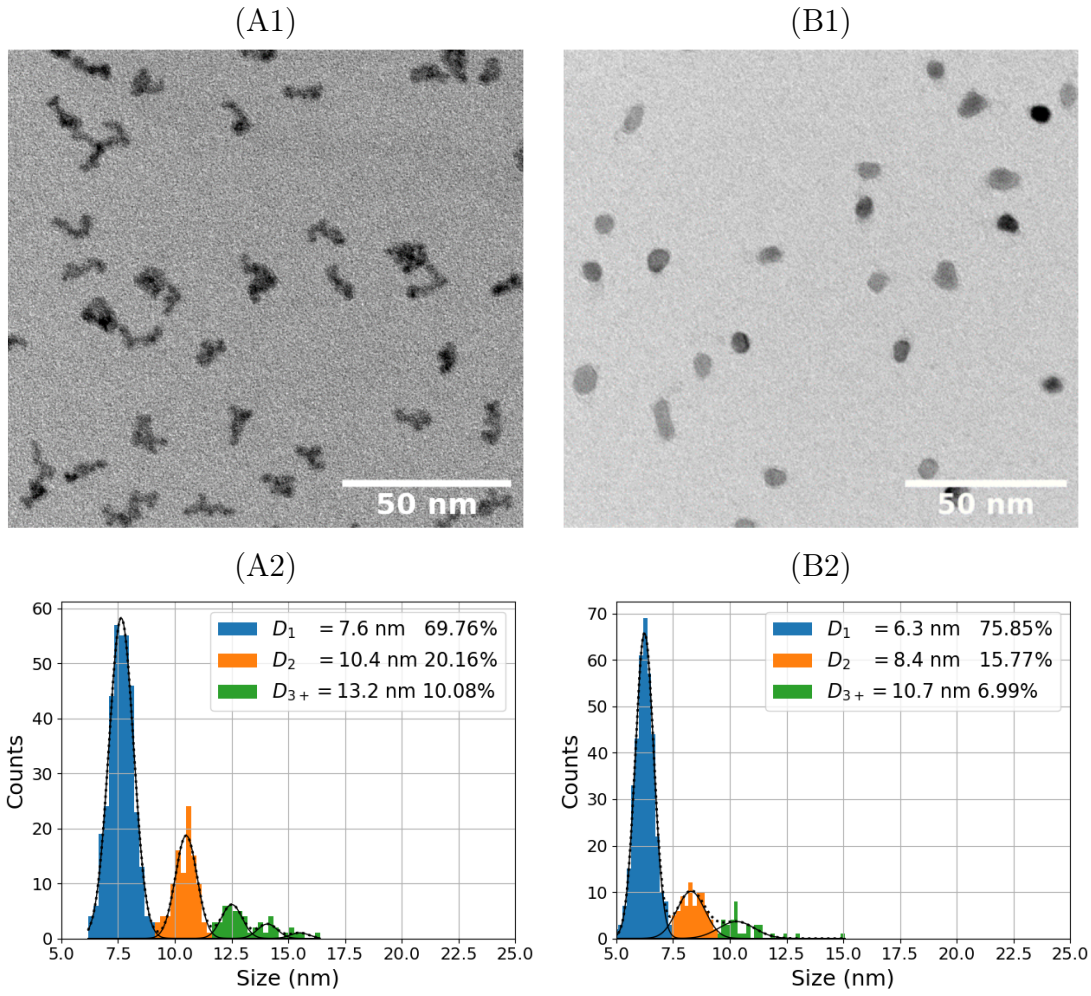

Figure 3.4: TEM image and size distribution for a LD sample.

TEM image for the LD sample as prepared (A1) and annealed (B1) with the respectives size hystpgram (A2) and (B2) fitted by a N-Gaussian and divided in 3 population D_1, D_2 and D_{3+} for study the percentage of each group

For the LD sample, the in-plane mean size (D_{mean}) is reduced after annealing (Figure 3.4) from 8.7 ± 0.1 nm to 6.9 ± 0.1 nm. This phenomenon is due to the fact that as a nanoparticle gets spherical, its outside plane projection increases. As an example, a dimer made of non-coalesced spherical monomers is expected to have a size of $D_2 = \sqrt[2]{2}D_1$ while the coalescence of 2 monomers into a spherical shape after annealing leads to $D_2 = \sqrt[3]{2}D_1$, reducing the measured size of the nanoparticle (See section 1.3).

The reduction of the D_2 and D_3 population after annealing in the LD sample can be attributed to the separation of nanoparticles that were non coalesced but

in touch.

In Figure 3.5 we can see that the HD sample presents a similar behavior and D_1 size to the LD sample, but with a reduction of the mean size from 10.4 ± 0.5 nm to 8.9 ± 0.5 nm. We notice that the only difference in preparation between both samples is the time of nanocluster deposition, so the monomer size should be similar for both samples.

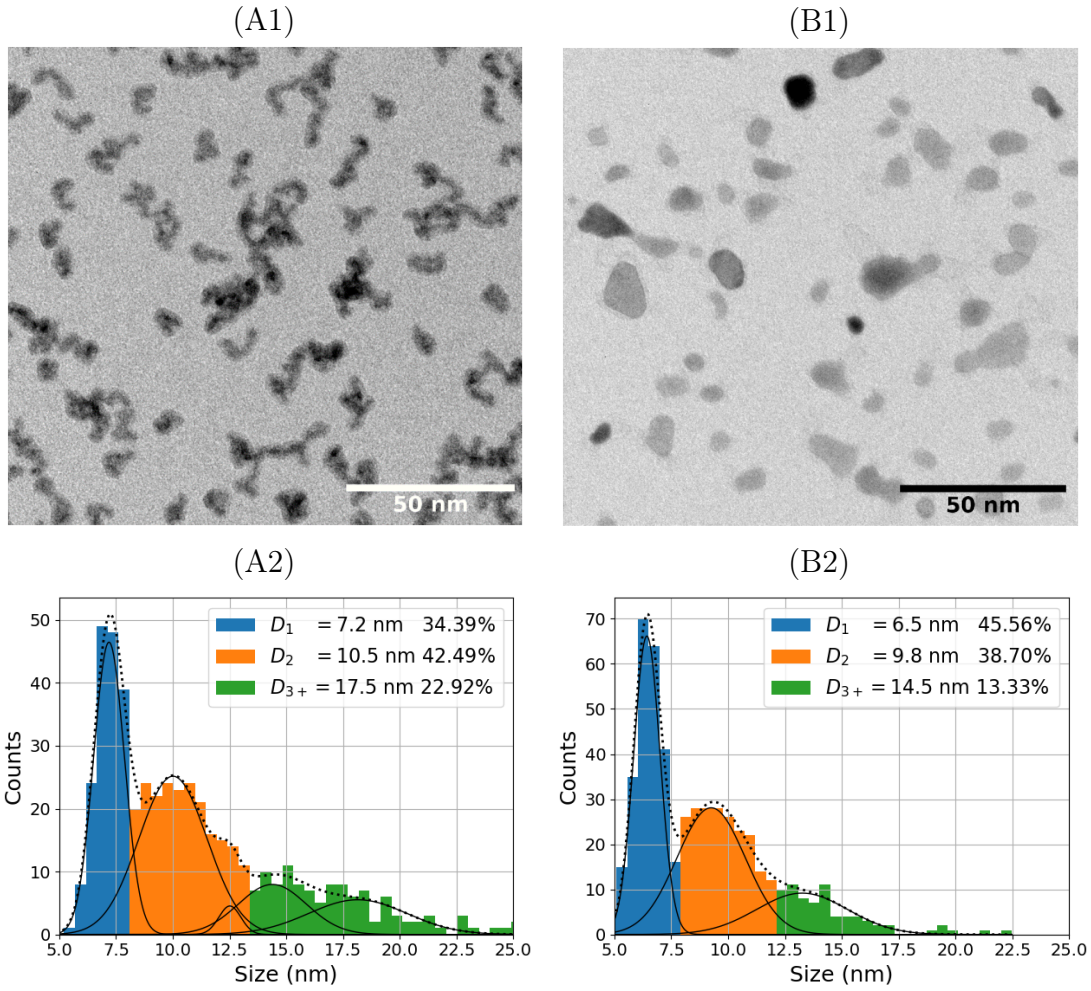

Figure 3.5: TEM image and size distribution for a HD sample.

TEM image for the HD sample as prepared (A1) and annealed (B1) with the respective size histogram (A2) and (B2) fitted by a N-Gaussian and divided in 3 population D_1, D_2 and D_{3+} for study the percentage of each group

On the other hand, for the higher density samples, size distribution changes as it is more probable to have dimer or N-mer with $N > 2$, thus increasing the percentage of D_2 and D_{3+}.

The fact that the D_1 size remains similar for both densities after annealing indicates the absence of Oswald ripering [85]. This means that the nanoparticles can either merge or split but they do not gradually exchange mass between them.

3.4 Shape description

It is possible to observe that the annealing makes the nanoparticles more rounded. To quantify this property the aspect ratio (AR) and the circularity (C) have been estimated (see section 1.3.3).

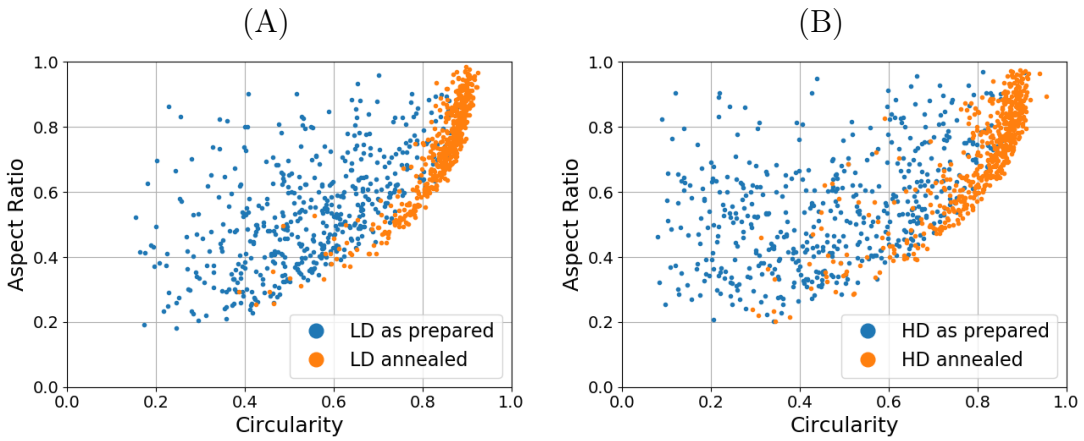

Figure 3.6: Aspect ratio and circularity before and after annealing
Map of aspect ratio vs circularity before annealing (blue) and after annealing (orange) for LD (A) and HD (B).

In Figure 3.6 we can see that for both samples after annealing, C increases noticeably, while AR increases but still covering approximately half of the range. For the LD sample, the obtained values were $C = 0.55$ and $AR = 0.54$ before annealing, and $C = 0.83$ and $AR = 0.73$ after annealing. For the HD sample, the obtained values were $C = 0.48$ and $AR = 0.55$ before annealing, and $C = 0.80$ and $AR = 0.71$ after annealing. These values reveal that the shape of the nanoparticles is quite similar for both densities, while the main difference is the percentage of D_1, D_2 and D_{3+}.

3.5 Surface occupation and distance between neighbors

To correlate magnetic behavior with the interactions between nanoparticles, it is necessary to have an indicator of the distance between the nanoparticles. We considered the nearest neighbor (NN) distance. For each nanoparticle on a TEM image, the NN distance was defined as the smallest distance between all paths from any point in the boundary to any point on the neighbors boundary, only if such distance is smaller than the distance to the boundary of the image.

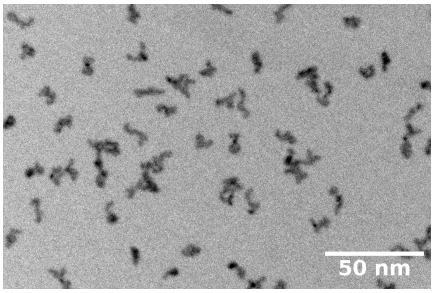

(A1)TEM image of a LD sample as prepared.

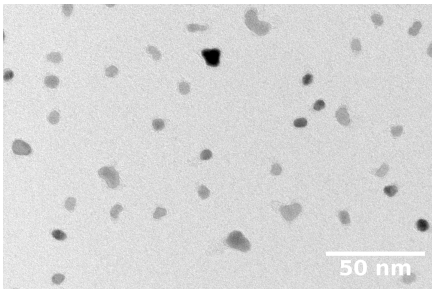

(B1) TEM image of a LD sample annealed.

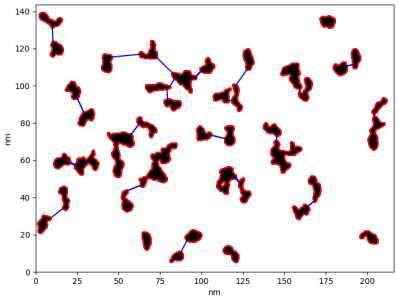

(A2) Boundaries and NN for the TEM image of a LD sample as prepared.

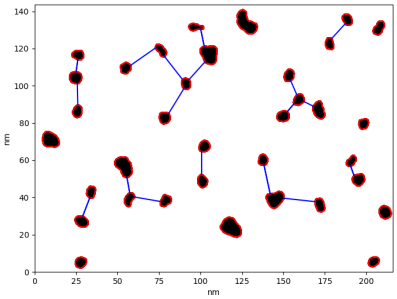

(B2) Boundaries and NN for the TEM image of a LD sample annealed.

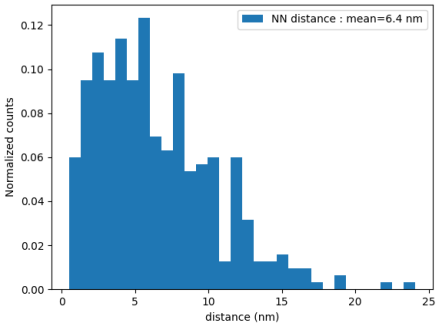

(A3) Histogram of NN for the TEM image of a LD sample as prepared.

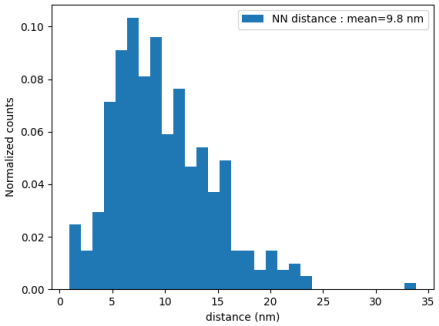

(B3) Histogram of NN for the TEM image of a LD sample annealed.

Figure 3.7: Image treatment for the identification of the distance to nearest neighbor (NN)

LD sample as prepared (A) and annealed (B) with the original TEM image (1), the image after treatment with touching edges nanoparticles removed, boundaries in red and distance NN in blue, and the NN distance histogram (3).

Note that the NN distance gives one path per nanoparticle, but the same path can be repeated between two nanoparticles.

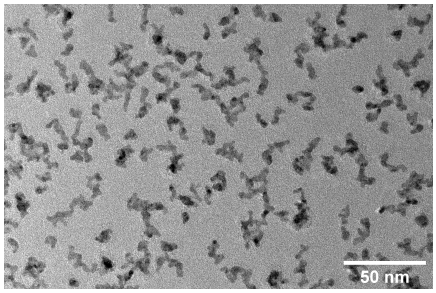

(A1)TEM image of a HD sample as prepared.

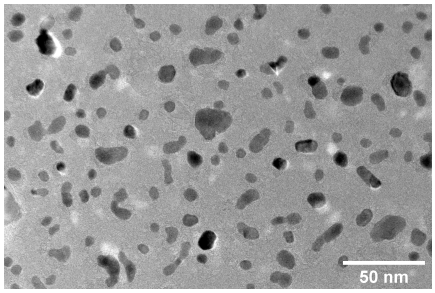

(B1) TEM image of a HD sample annealed.

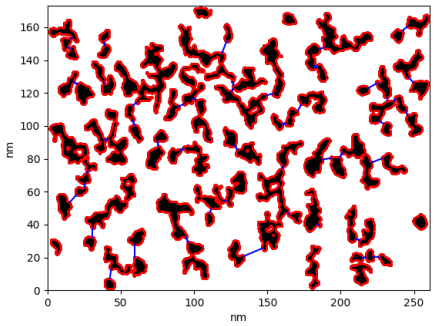

(A2) Boundaries and NN for the TEM image of a HD sample as prepared.

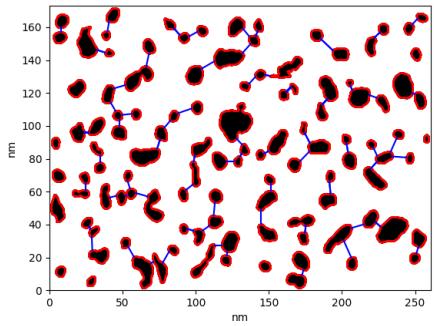

(B2) Boundaries and NN for the TEM image of a HD sample annealed

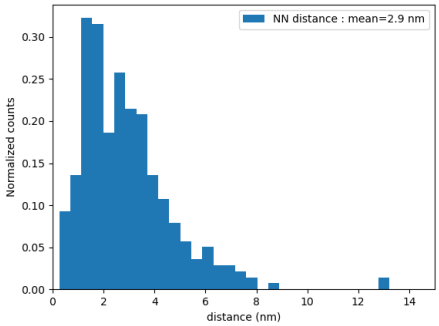

(A3) Histogram of NN for the TEM image of a HD sample as prepared.

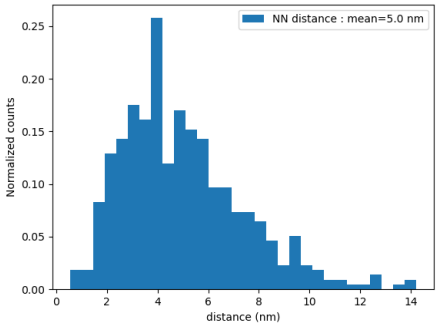

(B3) Histogram of NN for the TEM image of a HD sample annealed.

Figure 3.8: Image treatment for the identification of the distance to nearest neighbor (NN)

HD sample as prepared (A) and annealed (B) with the original TEM image (1), the image after treatment with touching edges nanoparticles removed, boundaries in red and distance NN in blue, and the NN distance histogram (3).

Over the same images, processed as indicated in Section 3.3, a *python3* program identifies all boundaries, the path, and NN distance for each nanoparticle.

In Figures 3.7 and 3.8, the results for a LD sample and a HD sample, respectibely, are shown. We can see two different phenomena: the expected higher NN distance for the LD sample, and the increase of the NN distance after annealing.

Sample	Status	D_1 (nm)	σ_1 (nm)	D_{mean} (nm)	NN (nm)	ρ (NPs/μ^2)
LD	as prepared	7.6±0.1	0.5±0.1	8.7±0.1	6.4±0.1	1300±100
	annealed	6.3±0.1	0.4±0.1	6.9±0.1	9.8±0.1	1200±100
HD	as prepared	7.2±0.5	0.7±0.5	10.4±0.5	2.9±0.5	2200±100
	annealed	6.5±0.5	0.6±0.5	8.9±0.5	5.0±0.5	2600±100

Table 3.1: Summary of size and density obtained for LD and HD samples

D_1 and σ_1 is the monomer diameter and the respective deviation from a Gaussian fit on the size for spherical approximation on histogram with mean value D_{mean}, NN is the distance to the nearest neighbor and ρ the density of nanoparticles per area.

3.6 Magnetic properties

In order to measure the magnetic properties of LD and HD samples, it is necessary to use multilayer samples since SQUID detection requires around 2 nm of equivalent thickness for magnetic matter. To perform the magnetic measurement of the LD system, a 15-layer sample of intercalated FeRh of equivalent thickness of 1.3 Å and nominal nanoparticle size of 7 nm, separated by a spacer of amorphous carbon has been fabricated. This sample is called LD2. For the HD system, we fabricated a 2-layer sample of FeRh of equivalent thickness of 10 Å and a nominal nanoparticle size of 7 nm, separated by two amorphous carbon layers. This sample is called HD2.

In all the SQUID measurements, the magnetic signal of the Silicon substrate has been estimated and substracted.

Field-cooling / zero-field cooling (FC/ZFC) susceptibilities have been measured at 5 mT for both samples (Figure 3.9).

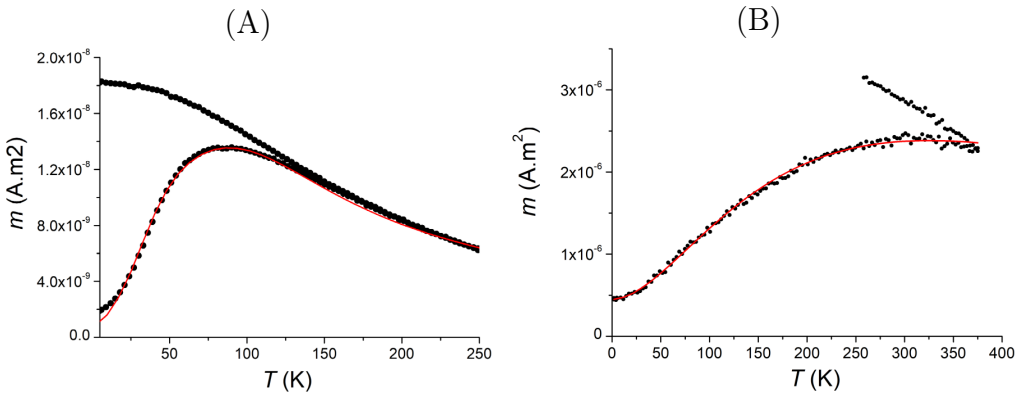

Figure 3.9: FC/ZFC for FeRh nanocluster embedded in carbon matrix.

Field-cooling/zero-field-cooling suceptivility curves for LD2 (A) and HD2 (B) with the experimental data in black and fit in red. The Field-cooling down was performed at 5 mT.

FC/ZFC curves on LD2 and HD2 reveal the characteristic super-paramagnetic behavior and the blocked regime of FM nanoparticles with $T_{max} = 80$ K for LD2 and $T_{max} = 300$ K for HD2 (Figure 3.9). Since T_{max} is related to the energy barrier $\Delta E = K_{eff}V$ (with K the effective anisotropy constant and V the volume), the tendency of higher T_{max} is in agreement with the higher average size observed for HD2 samples.

A fit over the FC/ZFC curves performed by a semi-analytical model [86] leads to simulated data of $D_1 = 6.3$ nm and $D_2 = 7.4$ nm, which is in good agreement with TEM experimental sizes. The effective anisotropy constant fitted for

LD2 is K_{eff} =120 kJ/m^3, with 38% of anisotropy dispersion. The same order of magnitude (K_{eff} =133 kJ/m^3) has been found in a previous work for 3 nm FeRh nanoclusters [48]. For the HD2 simulation, a value of K_{eff} =98 kJ/m^3, with 46% of anisotropy dispersion, has been used.

The decrease of K_{eff} as density increases can be attributed to the fact that the larger nanoparticles have less K_{eff} [43]. On the other hand, anisotropy dispersion can be explained by the higher dispersion of nanoncluster shape and size in HD2 (Figure 3.4 and 3.5).

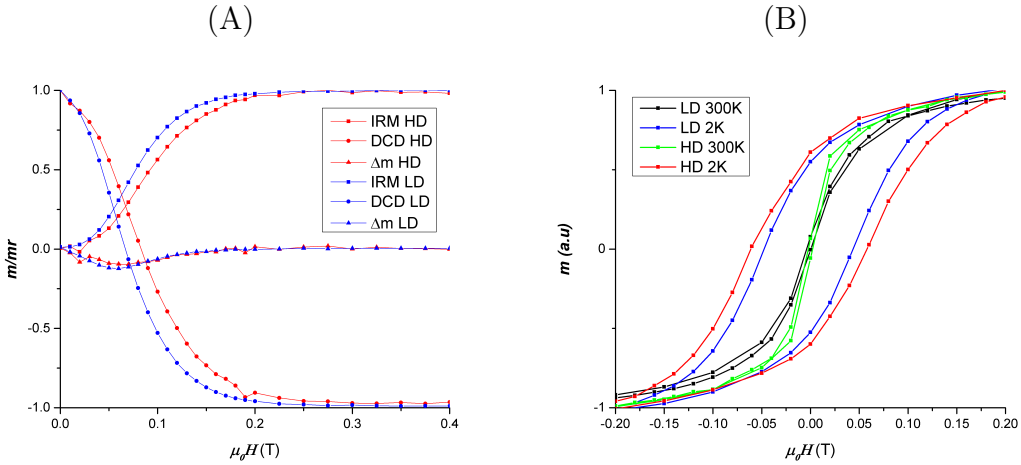

Figure 3.10: IRM-DCD and the hysteresis loops for LD2 and HD2 samples.

Inverse remanent magnetization and direct current demagnetization measured (IRM-DCD) at 2 K (A) with hysteresis loops performed at 2 K and 300 K

On IRM/DCD remnant magnetization curves (Figure 3.10 A) measured on annealed LD2 and HD2 samples, we also report the Δm defined as:

$$\Delta m = DCD(H) - (m_r - 2IRM(H)) \tag{3.1}$$

First of all, one can mention that for both annealed samples, Δm, defined as the difference between the isotermal remanent magnetization (IRM) and direct current demagnetization (DCD), is no longer zero. This reveals that the randomly oriented macrospin model of Stoner-Wohlfarth is no longer valid because magnetic interactions exist between nanoparticles [87], [66]. Even if there is no simple theoretical description for interacting nanoparticle assemblies, negative Δm is generally attributed to dipolar interactions between separated nanomagnets. On the contrary, exchange correlations between NPs in direct contact have negligible effects on Δm curves [66]. By referring to TEM observations, we found that for LD

samples the proportion of N-mers strongly decreases after annealing and the mean distance increases between FeRh clusters. This leads to high dipolar interactions for the LD2 sample. While there is more multimers in the as-prepared HD1 sample, in favour of direct exchange interactions upon annealing. This could explain a slight difference leading to : Δm(LD2) $>\Delta m$ (HD2).

On the hysteresis loops (Figure 3.10 B), it is possible to observe the persistence of the ferromagnetic domain even at low temperatures, indicating that the triggering size to achieve the metamagnetic transition is larger than 12 nm (approximately 85% of the nanoparticles in the HD2 annealed sample, as can be observed in Figure 3.5). HD2 approaches saturation more abruptly than LD2, in agreement with the higher direct magnetic interaction observed on IRM and ZFC curves (Figure 3.10 A and Figure 3.9)).

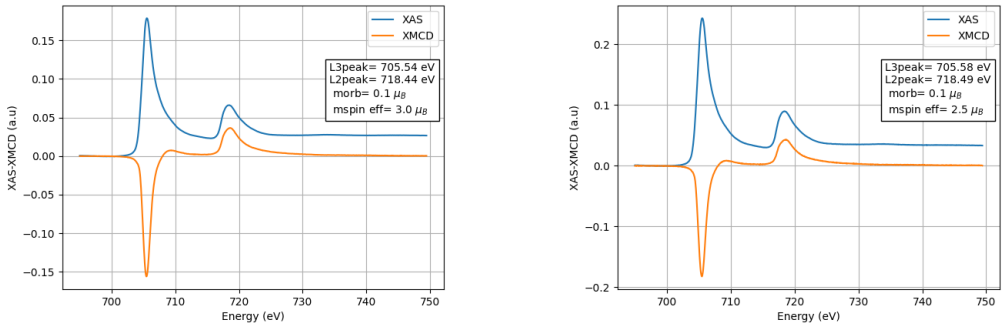

Figure 3.11: XMCD for FeRh nanoparticles in normal incidence configuration.

XMCD for FeRh nanoparticles of 7 nm for temperatures at 4 K (left) and 350 K (right) for normal incidence X-rays. More scans are displayed on Appendix D

For the HD2 sample, additional studies were performed in DEIMOS-SOLEIL synchrotron facilities. An XMCD measurement at the Fe L-edge with an external magnetic field of 1 T was performed at both normal (Figure 3.11) and 50° grazing incidence (Figure 3.12). The metallic Fe peak can be observed, with a magnetic moment decreasing as the temperature increases for both configurations. This is an indicator of the persistence of the ferromagnetic regime in the whole range of temperatures from 4 K to 350 K

It is possible to observe that the magnetic moment outside the plane is larger than in plane (Figure 3.13), but that the orbital magnetic moment is larger in plane as (see table 3.2). This indicates an out-of-plane anisotropy.

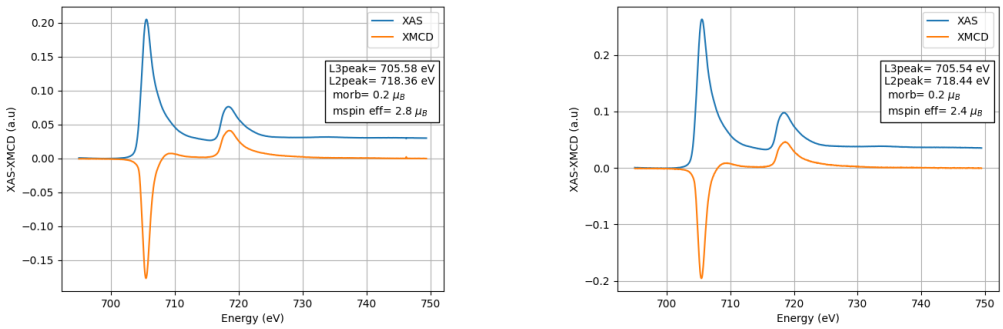

Figure 3.12: XMCD for FeRh nanoparticles in grazing incidence configuration.

XMCD for FeRh nanoparticles of 7 nm for temperatures at 4 K (left) and 350 K (right) for grazing incidence X-rays. More scans are displayed on Appendix D

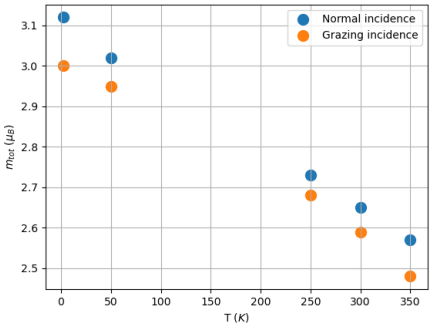

Figure 3.13: Magnetic moment of Fe on FeRh 3 nm nanocluster on carbon matrix.

Magnetic moment as function of the temperature for FeRh 3 nm nanocluster embedded in carbon matrix.

Temperature	Normal incidence			Grazing incidence		
	m_{orb} (μ_B)	m_{seff} (μ_B)	m_{tot} (μ_B)	m_{orb} (μ_B)	m_{seff} (μ_B)	m_{tot} (μ_B)
2 K	0.1±0.1	3.0±0.1	3.1±0.1	0.2±0.1	2.8±0.1	3.0±0.1
50 K	0.1±0.1	2.9±0.1	3.0±0.1	0.2±0.1	2.8±0.1	3.0±0.1
250 K	0.1±0.1	2.7±0.1	2.8±0.1	0.2±0.1	2.5±0.1	2.7±0.1
300 K	0.1±0.1	2.6±0.1	2.7±0.1	0.1±0.1	2.5±0.1	2.6±0.1
350 K	0.1±0.1	2.5±0.1	2.6±0.1	0.2±0.1	2.4±0.1	2.6±0.1

Table 3.2: Magnetic moment for FeRh nanocluster embedded in carbon matrix.

Magnetic moment obtained with XAS/XMCD at the Fe L edge for FeRh nanocluster embedded in carbon matrix

3.7 Discussion

We have proved that large FeRh nanoparticles as-prepared by low energy cluster deposition present a main A1 phase with complex shape, probably due to coalescence before and after mass selection. However, after annealing, nanoparticles successfully achieve more rounded shapes in the B2 phase, as revealed from TEM images as well as electron diffraction pattern techniques.

Upon this crystalline phase transformation and chemical ordering, there is no sign of segregation. Monomer size as well as the mean size, decreases due to the reduction of the area projected when a nanoparticle gets rounded in order to reduce surface energy.

In addition, the percentage of N-mers with $N \geq 3$ decreases while the percentage of monomers increases. This means that N-mers can be cut into individual monomers by heating. This last observation represents a drawback for the size limit that can be reached by nanoparticle coalescence. After annealing, all FeRh-nanoparticle samples have approximately the same monomer size, while the percentage of nanoparticles with size below 12 nm is respectively ≈100% for low density samples and ≈80% for high density samples. In this regard, 12 nm can be assumed as the largest nanomagnet size.

Concerning the fact that the ferromagnetic regime persists at low temperatures and inhibits the metamagnetic transition, this could be attribute to surface effects. This would be similar to other low-dimension systems presented in chapter 1, where residual ferromagnetism at the surface has been observed in thin films [30] and wires [31]. This phenomenon may be attributed to the reduced coordination number at the surface, which is, from the Stoner criterion, in favor of FM stability. In our case, it could also be due to finite size effects where relaxation in nanoparticles (implying fluctuations of the lattice parameter at surface) opposes the lattice contraction expected to accompany AFM state formation with complete spin compensation.

Another option is to evaluate if the dipolar interaction between nanoparticles may play a role in favor or against the metamagnetic transition. *Hillion et al* explored the case of 3-nm FeRh nanoparticles with low magnetic interactions that remain ferromagnetic at any temperature. In this chapter, we have shown that larger FeRh nanoparticles with both low and high densities present similar Δm, which is usually an indication of dipolar interaction. In the LD case, the sample possesses higher NN distances and fewer nanoparticles per area. The fact that Δm is slightly higher than for HD sample may indicate that there are more multimers in the as-prepared HD sample, in favour of direct exchange interactions upon annealing which have negligible effects on Δm.

Consequently, the dipolar interaction may not be a determining factor to favor the antiferromagnetic state but it may have influence on, and even be an impediment for the metamagnetic transition.

In the following chapters, on one hand, FeRh nanocluster-assembled films are explored, addressing the possibility that the metamagnetic transition depends on nanocluster size and/or magnetic interactions (Chapter 4). On the other hand, FeRh nanoparticles under epitaxy are also explored (Chapter 5).

The case of FeRh nanoparticles embedded in a binding matrix could be explored in the future as an extension of this work.

Chapter 4

FeRh nanocluster assembled film

Another configuration explored in this PhD thesis is a FeRh nanocluster assembled film of nominal thickness of 150 nm, corresponding to nanoclusters randomly stacked on the substrate, forming a porous percolated film (Figure 4.1). This system has the advantage of having a higher amount of material, easy to measure by SQUID magnetometry.

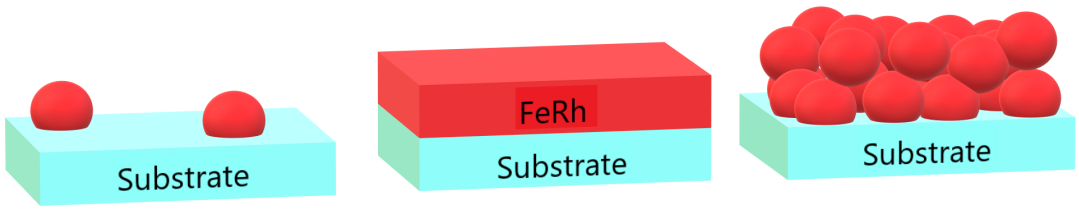

Figure 4.1: Scheme of samples with different mass organization

On the left a nanocluster on a substrate, on the middle a monocrystalline film and on the right a nanocluster assembled film

4.1 Sample preparation

FeRh nanocluster assembled films were deposited over Si(100) substrate by LECBD technique without mass selection (Section 2.2) with a nominal equivalent thickness of 150 nm. After a short transfer in air, the sample was covered with 15 nm of amorphous carbon capping. In an external UHV chamber, this sample was subsequently annealed at 500 °C for 2 hours, then at 700 °C for 3 hours in order

to achieve the B2 phase. In the following, this annealed sample will be named T1 sample.

4.2 Morphological and crystallographic characterization

As a reminder, previous works revealed that our laser vaporization technique produces stoichiometric nanoclusters with a probability density function described by a log-normal size distribution between 2 nm and 10 nm [88]. Therefore, a thick sample as prepared is initially mainly formed by crystallites in that size range.

In collaboration with Bruno Canut from INL, Rutherford backscattering spectrometry (RBS) experiments revealed that nanoalloy equiatomic stoichiometry is conserved in this T1 sample, even after cluster coalescence upon annealing (Figure 4.2). The RBS measurements were performed with $_4He^+$ ions of 2 MeV and a detector at 165° and 21 keV of resolution.

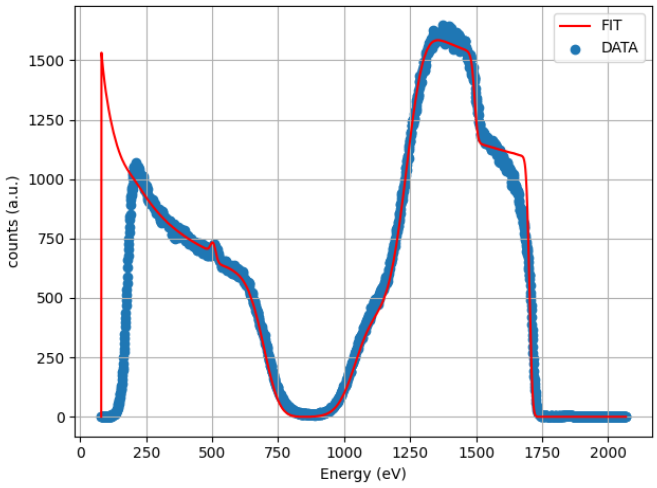

Figure 4.2: Rutherford back-scattering spectroscopy for a FeRh thick sample

Rutherford back-scattering spectroscopy for the 150 nm FeRh nanoclusters assembled film over Si (blue) and the respective fit (red)

The simulated curve presented in Figure 4.2 was obtained by taking into consideration the following model for the sample: a carbon capping on top, then a $C_XFe_YRh_Z$ region, and the Si substrate surface. The discrepancy between experimental data and fit at low energies is attributable to the fact that $_4He^+$ ions do

not probe experimentally as deep as the Si substrate thickness considered in the simulation.

For the carbon capping, the best fit gives 250×10^{15} atoms/cm^2. By considering the atomic mass of carbon m_C =12.011 u with *atomic mass unit* given by u =1.660 054 $\times 10^{-24}$ g, this corresponds to 5×10^{-6} g/cm^2 of carbon. In consequence, if we consider that annealing tends to graphitize the amorphous carbon layer, and using a bulk density of 2.26 g/cm^3, this implies an equivalent thickness of 22 nm for the carbon capping.

For the $C_XFe_YRh_Z$ region, the fit gives the ratio y/z= 1/1, but it is unfortunately not possible to assume bulk values in this region, since it is a porous combination of different phases that don't include the presence of oxide. Nevertheless, it gives a good atomic composition estimation of Fe/Rh= 50%/50% with an error bar of $3-4\%$.

Conventional specular XRD in $\theta/2theta$ mode has been performed to identify phase transformation after annealing (Figure 4.3) on the T1 sample. All the peaks corresponding to a main B2 phase were observed, with a lattice parameter of 2.98 Å (same as FeRh B2 phase bulk [7] and ICDD 04-002-2003). Notice that identical values have been obtained from high resolution transmission electron microscopy (TEM) and electron diffraction on diluted FeRh nanocluster prepared in the same conditions [89]. Less intense peaks are also observed in Figure 4.3 that correspond to the non chemically-ordered A1 phase with a lattice parameter of 3.77 Å (approximately 1% more than the FeRh A1 phase bulk reported in ICDD 04-011-5204).

Using the Scherrer formula [90] we estimate a crystallite size of 27 nm and 14 nm from FeRh B2-(011) and FeRh A1-(111) peaks, respectively (Figure 4.3). This is in agreement with the smaller domes observed in atomic force microscopy on the T1 sample, corresponding to a grain length of ∼30 nm (Figure 4.4). This demonstrates that this sample retains its granular morphology even upon annealing, knowing that as-prepared nanoclusters films done in the same conditions have about 60% of the bulk density [91], closer to a hard spheres model [92].

Is important to remember that in Figure 4.4 the vertical value observed (≈4nm) is a relative height to the neighbours top, so it actually doesn't give information unless we know the relative position between a nanoparticle and the neighbour.

A cross-section lamella of the T1 sample was prepared by conventional focused ion beam milling and lifted-off by David Troadec from IEMN at Villeneuve d'Ascq. In collaboration with Matthieu Bugnet from MATEIS, scanning transmission electron microscopy (STEM) was performed on this cross-section lamella at the Consortium LYon - St-Etienne de Microscopie (CLYSEM) by using the FEI

(A) (B)

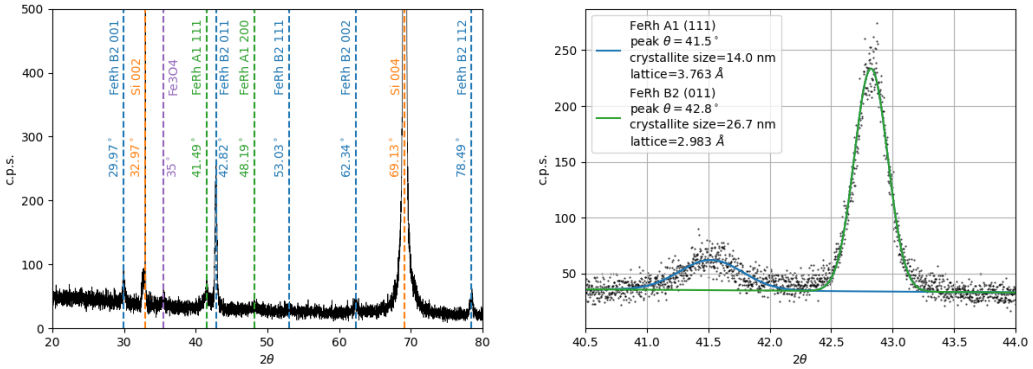

Figure 4.3: XRD obtained on the annealed FeRh nanocluster assembled film (named T1)

XRD in $\theta/2\theta$ mode for the FeRh nanocluster assembled of 150 nm of nominal thickness (A) and a zoom around $2\theta = 40°$ with a fit using Scherrer formula (B)

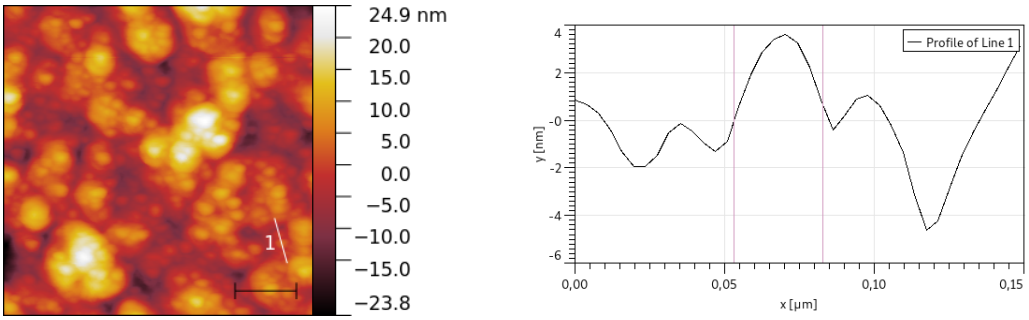

Figure 4.4: a) Atomic force microscopy image of the FeRh nanocluster assembly film (T1 sample). The scale bar is 200 nm. b) Topoplogy profile over grains of ∼ 30 nm along the line profile in a)

Titan ETEM G2, operated at 300 kV.

Note here that the nominal thickness of 150 nm of T1 sample corresponds to that of a dense film, however, the high porosity resulting from nanocluster assembly induces a much larger FeRh apparent thickness of ∼ 315 nm, as shown in the cross-section STEM-HAADF image of the T1 sample in Fig. 4.5, with 20 nm for the amorphous carbon capping in agreement with RBS. The film is highly porous, and by taking into consideration the height roughness observed from atomic force microscopy, the nominal/apparent thickness of this annealed nanogranular sample corresponds to a total volume occupation of 50%: less than the 60% observed for as-prepared Fe clusters assembled film [91]. Moreover, one can underline that the

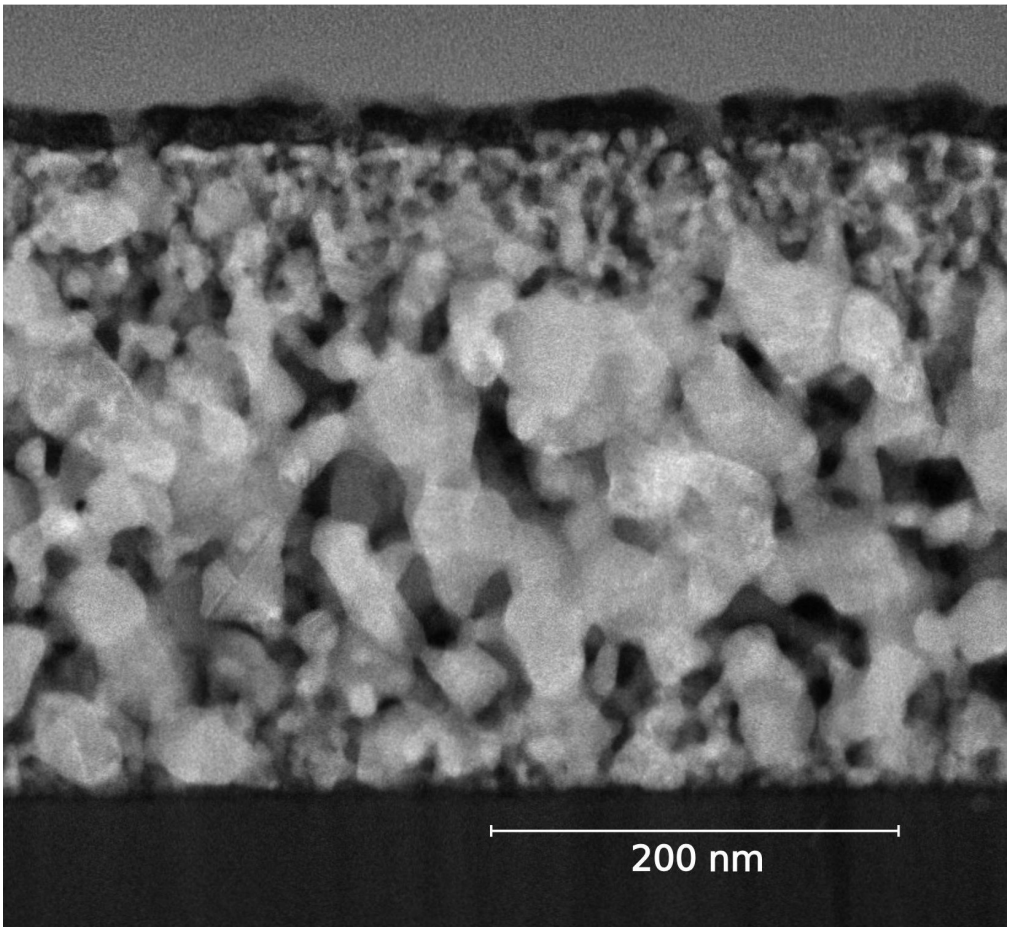

Figure 4.5: STEM cross section of a FeRh nanocluster assembled film

STEM cross section for a FeRh nanocluster assembles film of nominal 150 nm (assuming bulk density and no porosity) covered with 20 nm of amorphous carbon

smaller grains are located at the top surface sample and at the interface with the native silicon oxide of Si substrate. The alloyed FeRh composition of larger grains is clearly observable in Fig. 4.6 from EDX map performed on the cross section lamella of the T1 sample.

Some Fe_XO_{1-X} rich region can be identified near alloyed FeRh nanoparticles observed in the EDX map (Figure 4.6). So, even if such region may give a small contribution to the magnetic signal, this also implies that the FeRh B2 phase regions do not possess a 50%/50% ratio. However, this may not be actually part of the sample measured under magnetometry, due to the fact that is a cross section lamella and it is exposed to air.

To corroborate the effect of the annealing process and potential oxidation, a

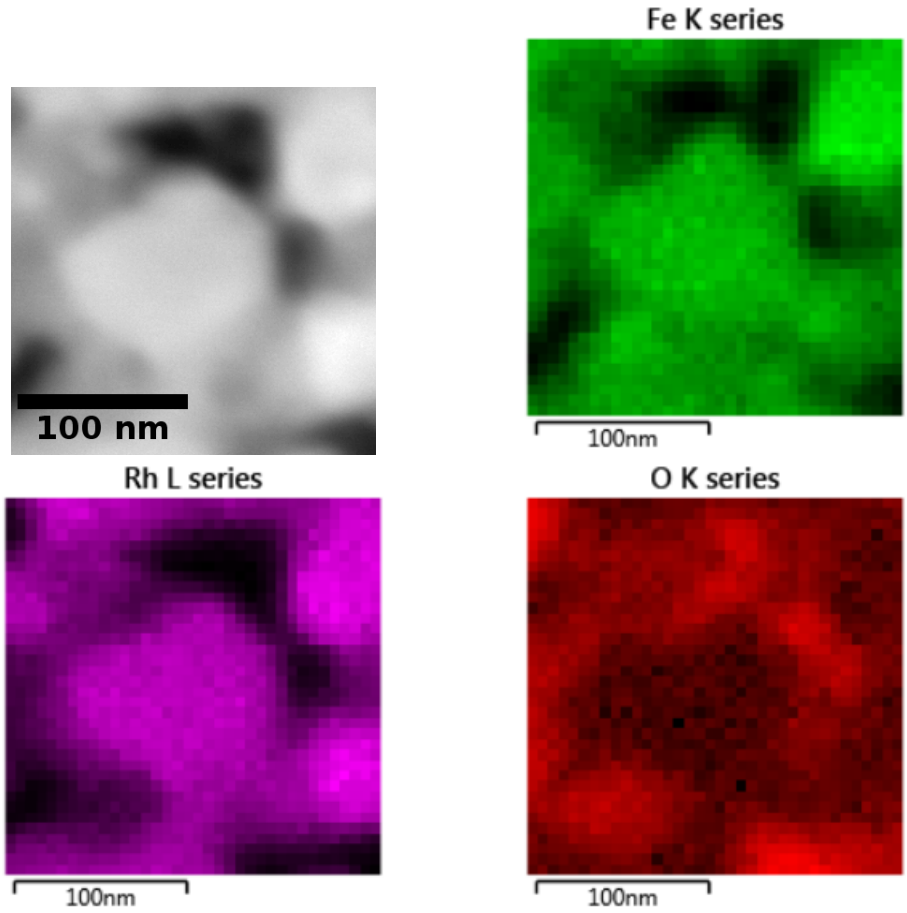

Figure 4.6: EDX map performed on the FeRh thich sample cross section lamela

In white the TEM cross section over a FeRh nanocluster assembled lamella and the EDX maps for Fe (green), Rh (purple) and O (red).

thick sample of FeRh 150 nm nanocluster assembled without carbon capping. We will call it the T2 sample.

From XRD measurements performed before and after annealing (Figure 4.7), we can see that the T2 sample starts as FeRh A1 nanocrystalline phase (we observe a large A [111] peak) and an oxidized contribution (probably as disordered Fe_3O_4 phase) indicating the existence of oxidation for the A1 phase.

After annealing at 700 °C for 3 hours, the T2 sample crystallizes mostly in FeRh B2 phase by conserving a small iron oxide contribution. Even if the A1 [111] peak is difficult to observe (because it is wider and right next to the B2 [011] peak), this residual A1 phase corresponds to smaller crystallites of the annealed T2 sample compared to T1 one, according to the Sherrer formula. On the other

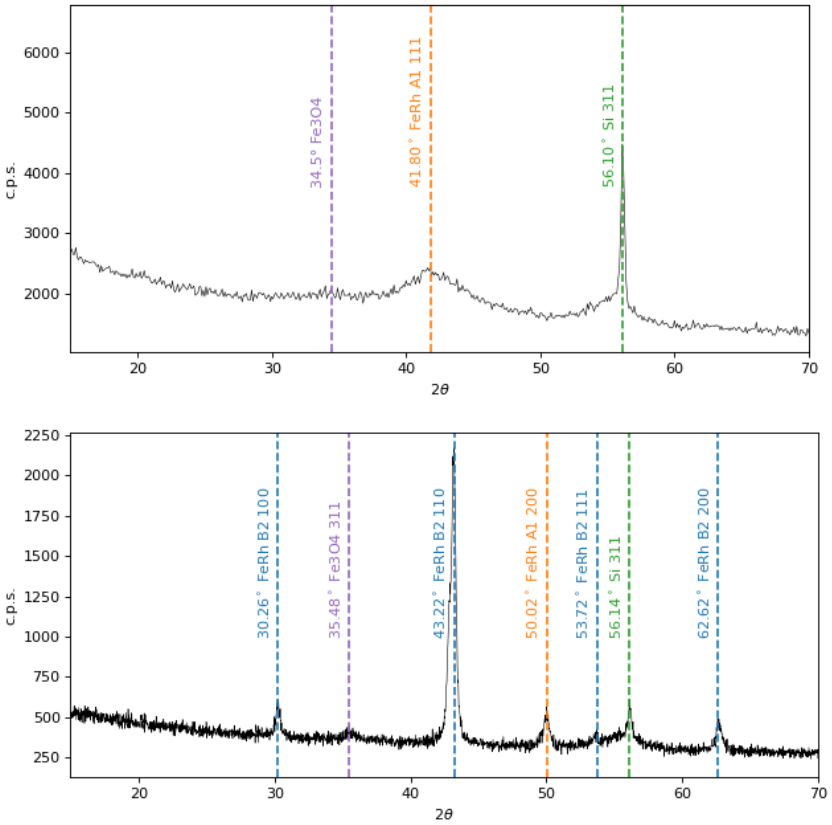

Figure 4.7: XRD obtained on the as prepared and annealed FeRh nanocluster assembled film without carbon capping (named T2)
XRD in $\theta/2\theta$ mode for the FeRh nanocluster assembled of 150 nm of nominal thickness before (top) and after annealing at 3 H 700 °C (below)

hand, for the B2 phase crystallite size has been found to be around 20 nm for the annealed T2 sample without carbon capping, which is smaller than the 25 nm for B2 crystallites found for T1 sample (Figures 4.8 and 4.3).

In order to compare the annealed FeRh thick samples either with or without carbon capping, Table 4.1 reports the values of the lattice parameter with the corresponding mean crystallite size, extracted from the [111] peak for the FeRh A1 phase, and from the [011] peak for the B2 phase, in both T1 and T2 samples.

From Table 4.1, one could note that the oxidation (clearly observable in T2 sample without capping) does not prevent the A1-to-B2 transformation. However, grain boundaries are probably an obstacle to the coalescence of the crystallites by avoiding the formation of crystallite sizes larger than > 25 nm, as reached in T1 capped sample.

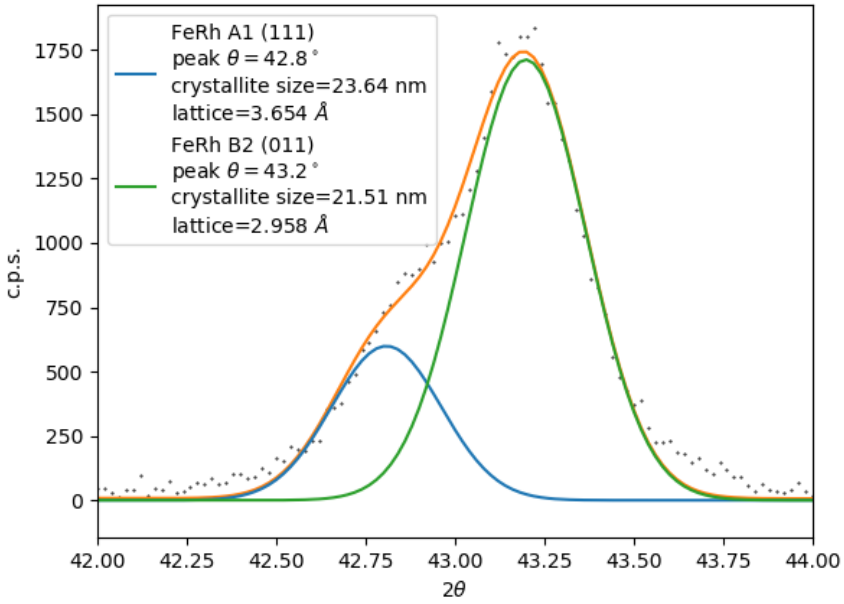

Figure 4.8: Sherrer fit fot sample T2

XRD zoom for sample T2 around $2\theta = 40°$ with a fit using Scherrer formula

Sample	Phase	plane	lattice parameter (Å)	crystallite size (nm)
T1	A1	[111]	3.76	14.0
	B2	[011]	2.98	26.7
T2	A1	[111]	3.65	23.6
	B2	[011]	2.96	21.5

Table 4.1: Scherrer fit for T1 and T2

Fitting parameters for the Scherrer formula over the peaks A1 [111] and B2 [011] for the sample T1 and T2

In order to study the phase transformation in terms of the local electronic structure, we prepare a new as-prepared capped thick sample (named T3 sample), equivalent to T1 sample but before annealing.

Both capped samples, T3 (as prepared) and T1 (annealed), were studied by X-Ray absorption near-edge structure (XANES) spectroscopy at the Fe K edge (7.113 k eV) and at the Rh L2 edges (3.139 keV) at ID12-ESRF synchrotron facilities.

On the top of Figure 4.9, XANES performed on both samples at Fe K edge reveal two different crystallographic signatures, characteristic of the chemically disordered FCC phase and of a BCC-like phase, respectively. This indicates that

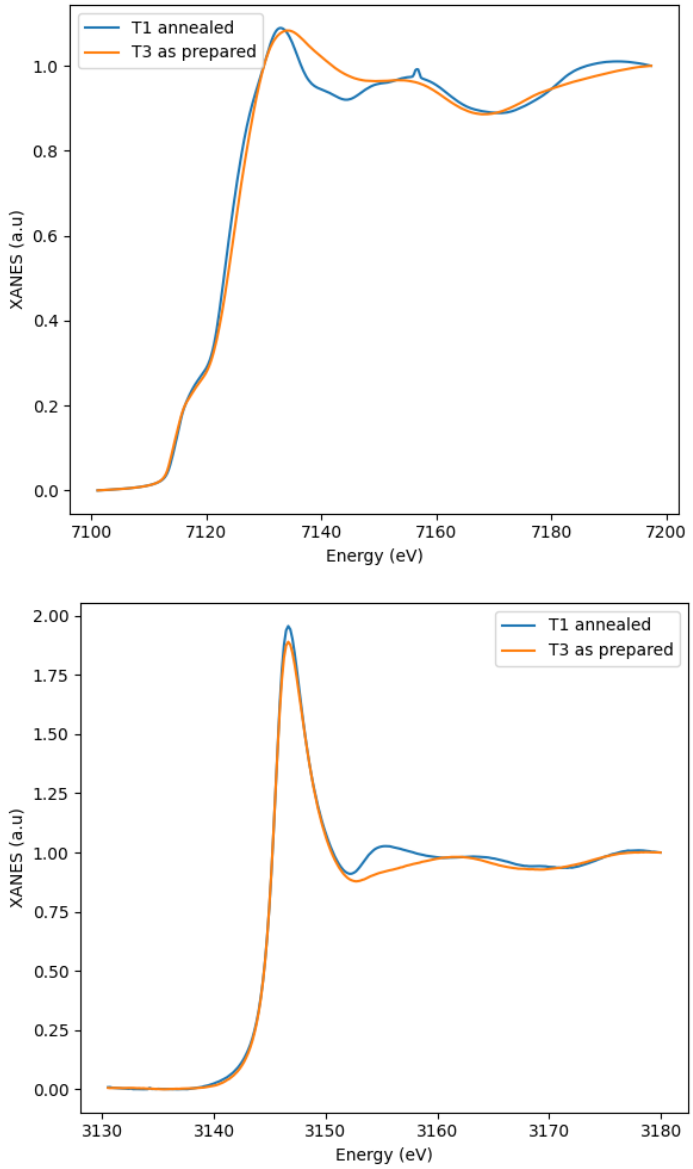

Figure 4.9: XANES at Fe K edge and Rh L_2 edge for annealed and as prepared thick sample

XANES at the Fe K edge (top) and Rh L_2 edge (bottom) for the sample T1 and T2 with 7 T at 320 K and 15° of incidence

the as-prepared T3 sample is in A1 phase (soft XANES oscillations due to chemical disorder), as previously observed in as-prepared A1 CoPt clusters. On the other hand, the annealed T1 sample is in B2 phase (very well structured XANES as in a BCC-like structure) due to chemically-ordered CsCl structure ([93, 94]).

On the bottom of Figure 4.9, by comparison with experimental references, same identifications have been done at the Rh L2 edge, where the XANES spectrum presents differences clearly attributed to the fact that T3 is in A1 phase [95], while T1 is in B2 phase [96]. These references are exposed on Appendix E.

4.3 Magnetic properties

SQUID thermal magnetization measurements regardless of the applied magnetic field $\mu_0 H$ performed on the T1 sample, systematically reveal a broad and asymmetric metamagnetic transition around room temperature with a sharp transition from AFM to FM in heating mode and a smooth transition from FM to AFM in cooling mode. Is the widest FeRh transition observed having separated branches from 100 K to 400 K [97].

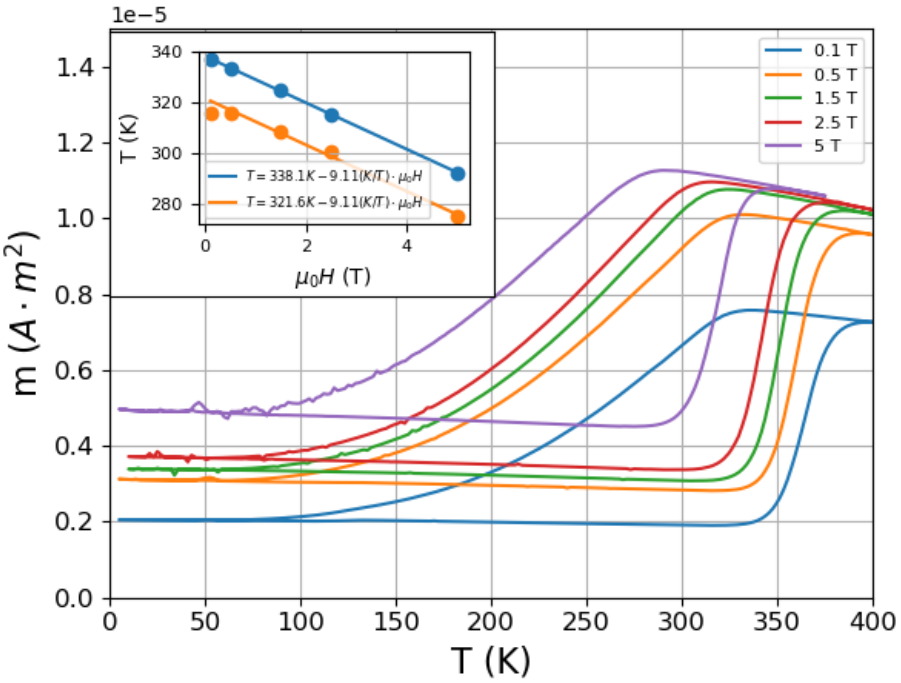

Figure 4.10: Magnetization as function of the temperature for a FeRh nanocluster assembled film (T1 sample)

Magnetization as function of the temperature for external fields between 0.1 T to 5 T. On the insert the transition temperature as the minimum (blue) and maximum (orange) magnetic moments with respectives fits $T = 338.1K - 9.11(K/T)\mu_0 H$ for the minimun magnetic moment and $T = 321.6K - 9.11(K/T)\mu_0 H$ for the maximun magnetic moment.

Interestingly, despite the peculiar nanogranular microstructure of this sample, we obtain the same linear dependence of the transition temperature versus $\mu_0 H$ (Figure 4.10 insert) as reported for continuous thin films, of around -9 K/T [24]. Moreover we obtain higher residual ferromagnetic signal at 2 K for higher applied magnetic field (Figure 4.10).

The remained presence of the ferromagnetic regime is also observable in the hysteresis loops M(H) (Figure 4.11). It is possible to see that the sample does not fully saturate for temperatures equal or lower than 300 K, indicating also the presence of a non ferromagnetic component.

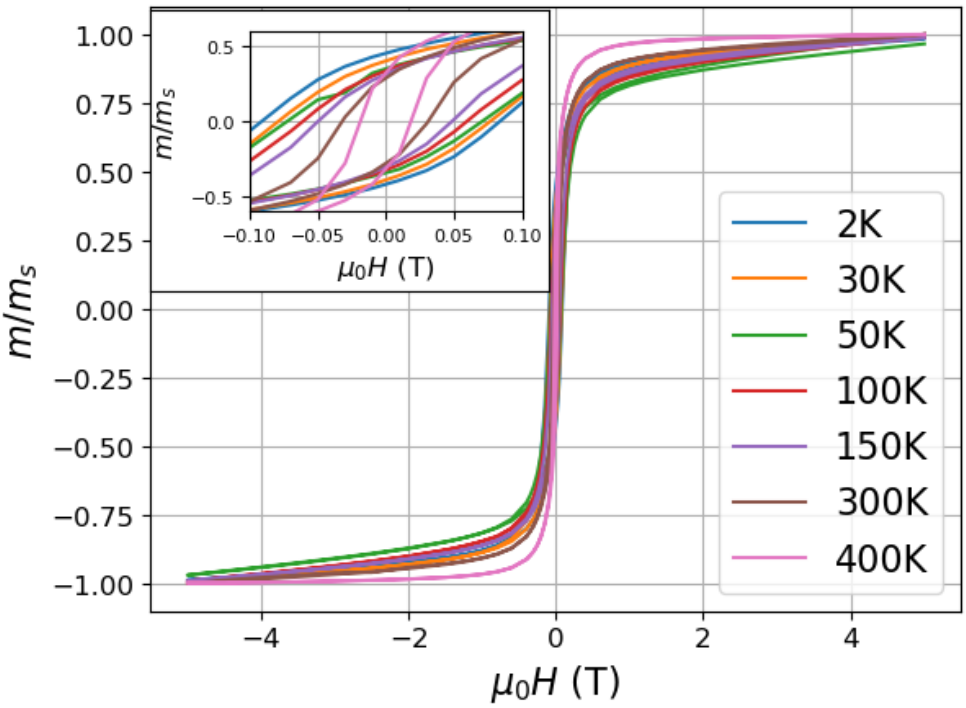

Figure 4.11: Magnetization as function of an applied magnetic field for a FeRh nanocluster assembled film

Magnetization as function of an applied magnetic field for temperatures between 2 K to 400 K. On the insert the transition temperature as the minimum (blue) and maximum (orange) magnetic moments.

From the hysteresis loops (Figure 4.11), we observe that the remanent magnetizations increase for temperatures higher than 200 K as the beginning of the metamagnetic transition. Moreover, M(H) curves measured at 2 K present a higher remanent magnetization than the rest of the points below 200 K that is an indication of possible superparamagnetic state for some components (Figure 4.12).

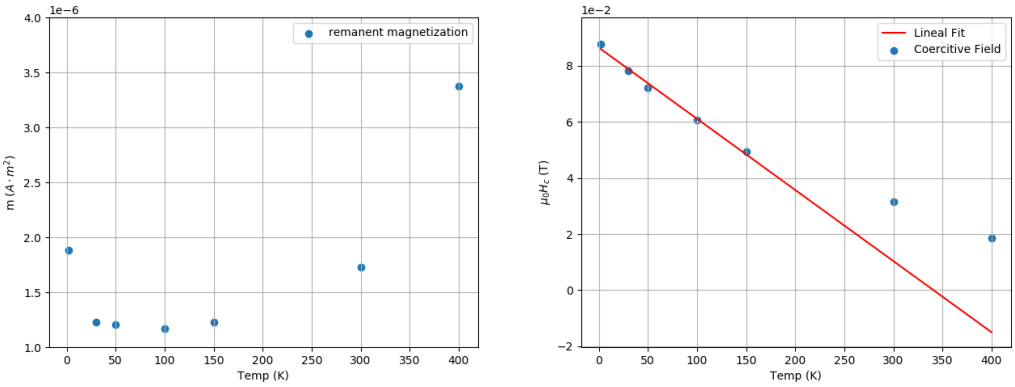

Figure 4.12: Remanent magnetization and Coercitive field as function of the temperature for FeRh 150 nm thick film

for a 150 nm FeRh nanocluster assembled film; Remanent magnetization as funtion of the temperature (left) and coercitive field as function of the temperature (right)

Since the B2 phase crystallites are around 30 nm (Figure 4.3) and the sample is porous and granular (Figure 4.5) then it could be possible to have interactions between magnetic metallic nanocrystal and oxide AF boundaries known as Exchange bias. So the hysteresis loop at 10 K for the Field Cooling and Zero Field Cooling branches was measured in SQUID. We have found that the difference of the ZFC/FC coercitive field (typical of exchange bias) only corresponds to 0.095 T indicating a very small interaction between magnetic lattice/boundaries (see Figure 4.13).

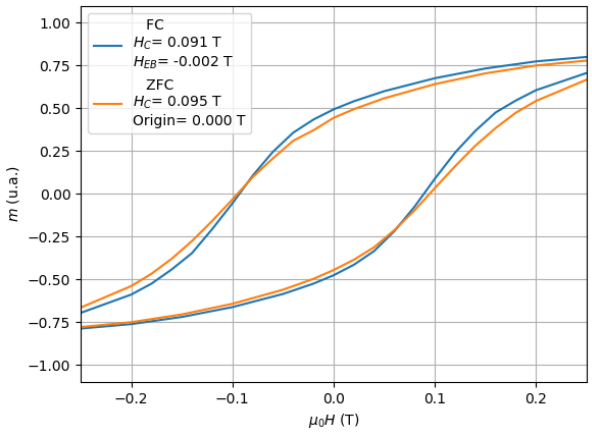

Figure 4.13: Exchange bias for a FeRh nanocluster assembled film

Hysteresis loop at 10 K for field cooling (blue) and zero field cooling (orange) branches.

We propose that this residual magnetization could be attributed to a non-switchable component remaining in the FM phase regardless the temperature probably correlated to heterogeneities in the T1 sample. By considering two FM contributions for the temperature dependence of the magnetic moment, and assuming the same Curie point for both, $m(T)$ curves were extrapolated to get the percentage of switchable/non switchable components in absence of applied field as presented in the Fig. 4.14. The magnetic contribution that remains FM regardless the temperature represents 25% of the total magnetization.

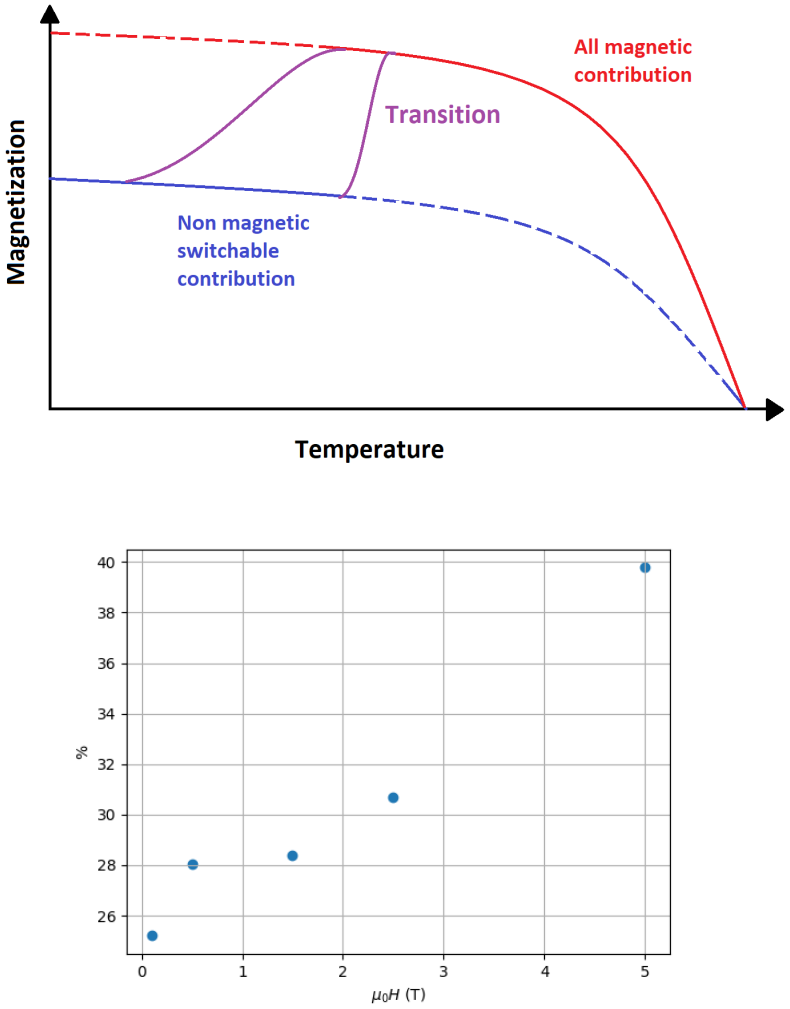

Figure 4.14: Scheme of Switchable/Non Switchable contributions model

Model used to estimate the magnetic component that presents the metamagnetic transition and the component thats remains ferromagnetic (top), and the obtained percentage on the magnetic contribution of the component with metamagnetic transition (bottom)

To study the metamagnetic transition of the T1 sample, we explored what happens if we try to go from the cooling down branch to the heating up branch and *vice versa* by controlling the applied magnetic field. Therefore, the thermal magnetization was measured continuously for 1.5 T and then the same loop was repeated but stopping at certain temperatures to measure hysteresis loops. The detailed procedure presented in (Figure 4.15) is the following:

- Starting form 400 K 1.5 T
- Cooling down to 250 K
- Moving field to 5 T, then to −5 T, then to 5 T and then going back to 1.5 T.
- Cooling down to 4 K
- Heating up to 250 K
- Moving field to 5 T, then to −5 T, then to 5 T and then going back to 1.5 T.
- Heating up to 325 K
- Moving field to 5 T, then to −5 T, then to 5 T and then going back to 1.5 T.
- Heating up to 400 K

On the Figure 4.15 we can notice many things:

- When we did the hysteresis loop in the cooling down branch (point 1 to 2) the magnetization decreases but it does not go to the heating up branch
- When we cool down starting between branches then the magnetization remain constant until it goes to the cooling down branch (point 2)
- If we do the hysteresis loop in the heating up branch but far from the metamagnetic transition (point 3) then it ends with the same magnetization
- If we do the hysteresis loop in the heating up branch near the metamagnetic transition (point 4 to 5) then the magnetization increases but does not go to the cooling down branch
- When we heat starting between branches then the magnetization remain constant until it goes to the heating up branch (point 5)
- The hysteresis loop near the abrupt metamagnetic transition in the heating up branch at 325 K posses an opening in the saturation region.

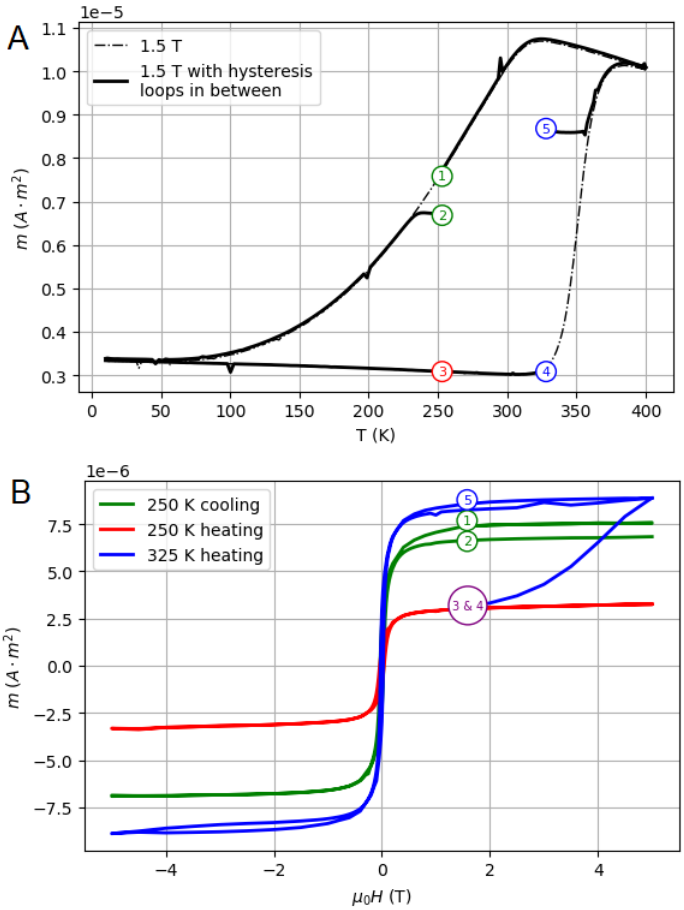

Figure 4.15: Hysteresis loops at different point of the magnetization versys temperature curve for 1.5 T

Magnetization as function of the temperature (left) for 1.5 T and continues (black) and interrupted (red) to perform hysteresis loops (right) between 5 T and −5 T at 250 K cooling (green curve starting in point 1 and finishing in point 2), 250 K heating (red curve starting and finishing in point 3) and 325 K heating (blue curve starting in point 4 and finishing in point 5)

To go further in the understanding of the coexistence of different magnetic features that may be attributed to spatial heterogeneity, particle size distribution or/and surface oxidation, we used the chemical selectivity of X-ray absorption spectroscopy (XAS) and X-ray magnetic circular dichroism (XMCD) techniques performed on complementary french X-rays synchrotron facilities : SOLEIL and ESRF.

The DEIMOS beamline at SOLEIL synchrotron has been used to study and access to quantitative evaluation of local spin and orbital magnetic moment at

Fe L-edge (around 707 eV) and qualitative at M-Rh edge (around 590 eV). Both energies correspond to soft X-rays region with short penetration depth where the TEY is the most powerful detection method that gives a high surface sensitivity with a sampling depths of ∼3 nm. While Fluorescence yield (FY) probes deeper than TEY, but the signal is low in the soft x-ray region.

The ID12 beamline at ESRF has been used to reach a structural signature more deeply from XAS at Fe-K edge (around 7000 eV) and at Rh-L edge (around 3000 eV) including a more quantitative magnetic moment evaluation of 4d electron in Rhodium. This range of absorption energies corresponds to hard x-rays region that offer large penetration depth where FY is generally used in grazing incidence for a film.

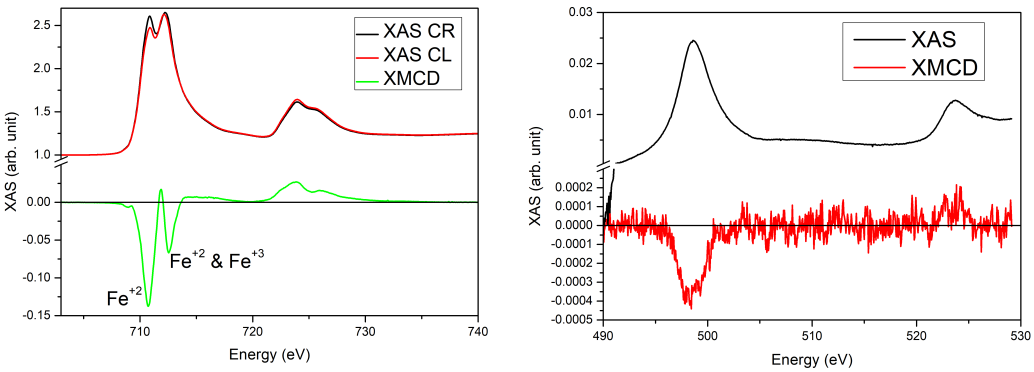

Figure 4.16: X-ray absorption spectroscopy (XAS) and X-ray magnetic circular dichroism (XMCD) obtained on the annealed FeRh T1 sample at the Fe $L_{2,3}$ (top) and at the Rh $M_{2,3}$ (down) edge at room temperature and under 1.5 T.

First of all, XAS/XMCD experiments have been performed on the thick FeRh annealed T1 sample at the DEIMOS beamline of SOLEIL synchrotron where only metallic contribution has been detected at the Rh M-edge but iron oxide clearly seen at the Fe L-edge (Figure 4.16). More precisely, an induced magnetic moment on Rh due to hybridization with Fe is in favour of FM B2 FeRh alloy while the Fe_3O_4 signature clearly identified on XAS/XMCD at the Fe L edge [98] but not observable in the XRD pattern (Figure 4.3), is in favour of oxidization at the sample surface or deeply at the grain boundary in the form of amorphous or weakly crystalline magnetite shell at the cluster surface, which passivates the FM bimetallic B2 core [99, 100].

Notice that the presence of such Fe_3O_4 was also observed on an equivalent thick FeRh sample prepared without carbon capping (named T2 sample) from X-Ray diffraction (XRD) and X-ray Photoelectron Spectroscopy (XPS) where we verified that oxidized surface can be reduced by in-situ UHV annealing at temperature T

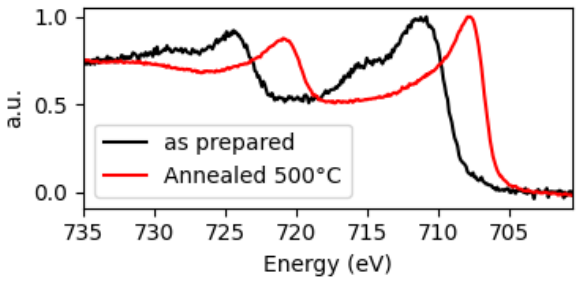

Figure 4.17: XPS on reduction for a FeRh thick T2 sample non C-covered.

XPS for a 150 nm FeRh film non covered and annealing in situ UHV at 500 °C

around 500°C (Figure 4.17) as already observed in Fe surface nanoparticles [100]. This is also consistent with the previous observations of a Fe_3O_4 peak in both as prepared A1 sample T2 (Figure 4.7) and annealed B2 phase sample T1 (Figure 4.3).

The magnetism for uncovered as-prepared sample T2 where the main magnetic signal corresponds to both A1 FeRh phase and oxide, it has been found a magnetization of around two order of magnitude lower than the one obtained for covered annealed sample, even after several annealings (Figure 4.18). So this implies that even with residual FeRh A1 phase and iron oxide, the main magnetic contribution is controlled by the FeRh B2 phase. It also reveals that for the A1 to B2 transformation the oxide may impede the phase transformation

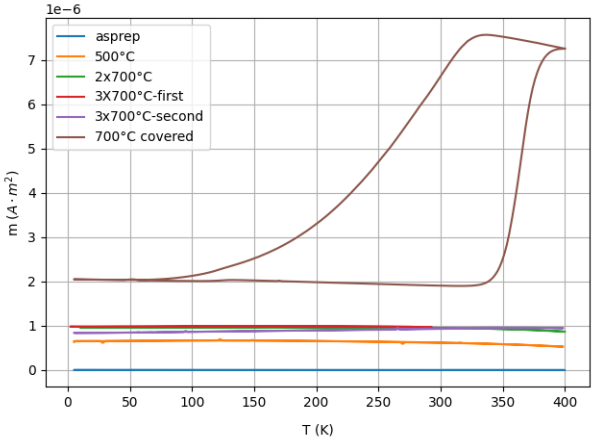

Figure 4.18: Effect of C capping on the magnetization as function

Magnetization as function of the temperature for the non covered sample T2 at different annealings and the covered sample T1 at 0.1 T.

In order to try to reduce the oxide in the sample T1 capped with carbon, we perform new XAS/XMCD measurements at the Fe L and Rh M edges with in situ UHV annealing. In the Figure 4.19, we present XAS/XMCD measurements in TEY mode obtained on the T1 sample after in situ annealing during 5 hours at 600°C.

The Figure 4.19 reveal a partial reduction with a metallic contribution around $75 \pm 5\%$ and also a metamagnetic transition with high remanent ferromagnetic contribution. The orbital and spin magnetic moments per Rh and Fe atom at different temperature are given in Table I by using the sum rules [80, 81] with FeRh bulk alloy number of d holes, equal to 3.51 in the Fe 3d band and equal to 2.34 in the Rh 4d band [48, 101].

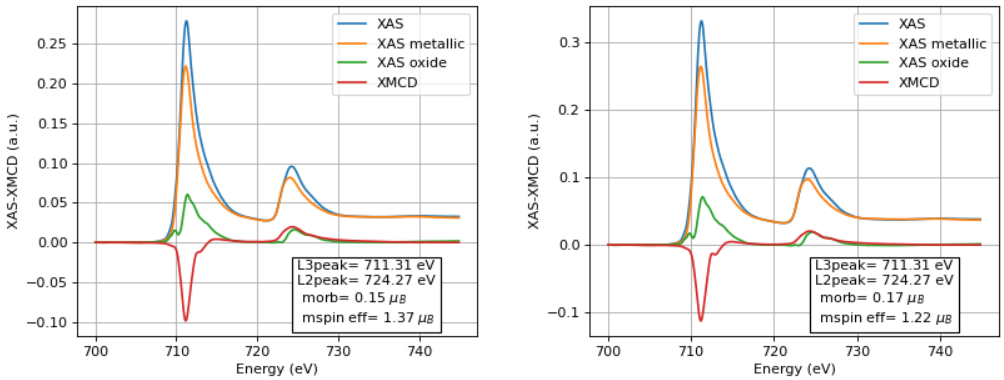

350K 4K

Figure 4.19: XMCD for FeRh thick sample in the cooling down branch.

XMCD at 350K, 300K, 250K, 200K, 100K and 4K in the cooling branch down for the 150nm thick FeRh nanocluster assembled film after being reduced in situ UHV

From XMCD at Fe $L_{2,3}$ edge TEY measured in the cooling mode (Figure 4.19 and in Appendix D) under 6 T, we observed the same behavior as the one obtained from global metamagnetic transition where the residual magnetization correspond to $25 \pm 5\%$ of B2 population that is not switchable.

At first sight, qualitative analysis of results suggest that nanoalloy effects involving metallic Fe are responsible to the metamagnetic transition shape in B2 FeRh nanogranular system. In particular iron oxide cannot explained the residual magnetization at low temperature.

On Figure 4.20 is presented the total magnetic moment obtained from Figures 4.19 at 2K and 350K, others XAS/XMCD presented at diferent temperatures of the cooling down branch and heating up branch are exposed in the appendix D Figure. The presence of the metamagnetic transition is noticed, but it posses

some differences when is compared with the results on SQUID (Figure 2.3): The residual component is around 70% of the total magnetization and the loop is closed at 300 K for 6 T far from what we observed in SQUID that the loop is closed at 350 K for 5 T.

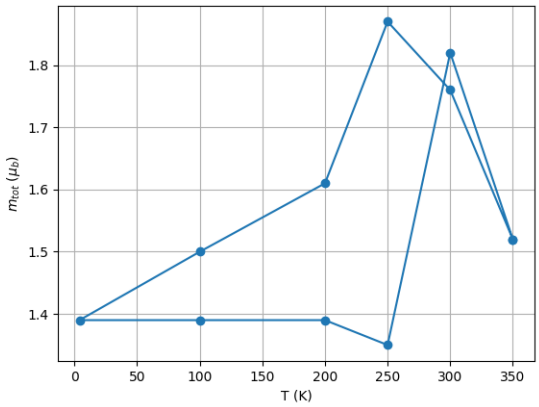

Figure 4.20: Fe L edge magnetic moment as function of the temperature

Magnetic moment as function of the temperature for a FeRh thick film obtained from XMCD at the Fe L edge

The presence of a strong oxide peak in fluo make no possible to properly remove the oxide signal due that the process used assumed a low contribution to the XMCD from the oxide. To compare in volume vs in the upper regions signals it was used the ratio of the XMCD over the XAS in the L_3 peak as a first approximation. This remark a heavily difference on the metamagnetic transition (Figure 4.21)

Finally, complementary experiments at ID12-ESRF synchrotron facilities were performed over the T1 sample to probe the thermal magnetic moment evolution at the Rh L edge. The XANES/XMCD spectra reveal the presence of magnetic signature at the Rh L edge (Figure 4.23) with 0.28 μ_B at 2K and 0.6 μ_B at 320K, corroborating the observed one in the Rh M edge (Figure 4.16). Also the Figure 4.23 show an increase of magnetic moment when heating from 4 K to 320 K indicating the presence of metamagnetic transition.

A on-the-fly XMCD measurement over the Rh L2 peak reveals the same shape for the metamagnetic transition (Figure 4.24) as the one observed from SQUID measurements (Figure 4.10): broad, asymmetric and with a residual ferromagnetic component. Using the magnetic moment obtained at 2 K and 320 K (Figure 4.23) there is around 57% of residual ferromagnetic component for 7 T that is consistent with the percentage deduced from SQUID metamagnetic transition which is 50% of ferromagnetic component for 5 T and increasing. The percentage of residual

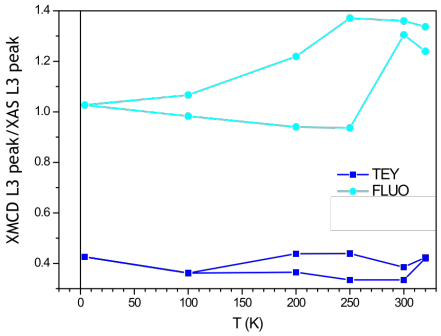

Figure 4.21: XMCD/XAS ratio at L_3 peak.

FeRh magnetic signal estimated as the ratio of XMCD/XAS at the L_3 peak for the Fluo and TEY signals at 6 T.

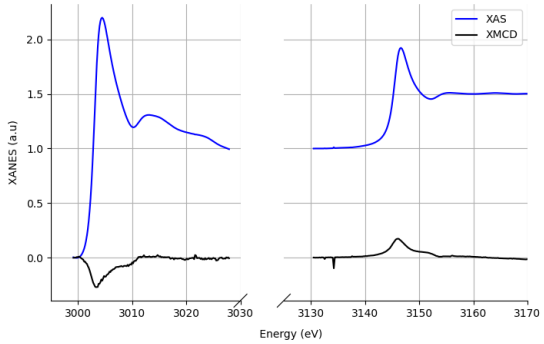

Figure 4.22: XANES/XMCD at 320K for FeRh nancluster assembled film.

For the 150 nm nanocluster assembled covered with amorphous carbon the XANES (on blue) and XMCD (on black) on the Rh L edge at 2 K, 7 T with 15° of incidence X-ray beam.

ferromagnetic component does not match the one observed at the Fe L edge (Figure 4.20) but notice that the TEY has a probing deepness of only few nanometers, so XMCD measurements at the Fe L edge correspond to a measure of the top part of the film that posses smaller grains as is observed by STEM (Figure 4.5).

On the Figure 4.11 the hysteresis loops measure on SQUID shown that in the saturation region the hysteresis loops present slope and as the temperature increasing the slope decrease achieving a full saturation at 400 K. A similar behaviour is observed in the hysteresis loops on the Rh L edge (Figure 4.24) where there is a slope for the 2 K hysteresis loop but not for the 320 K hysteresis loop.

On the Figure 4.15 is also noticeable that the hysteresis loop performed near

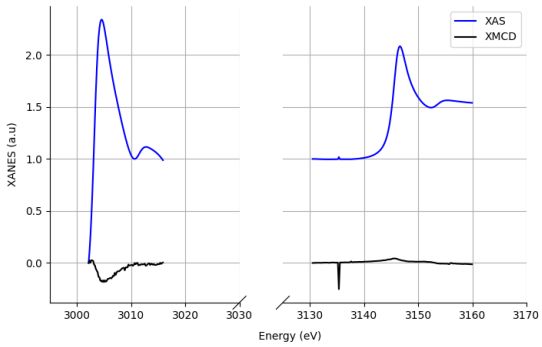

Figure 4.23: XANES/XMCD at 320K for FeRh nancluster assembled film.

For the 150 nm nanocluster assembled covered with amorphous carbon the XANES (on blue) and XMCD (on black) on the Rh L edge at 320 K, 7 T with 15° of incidence X-ray beam.

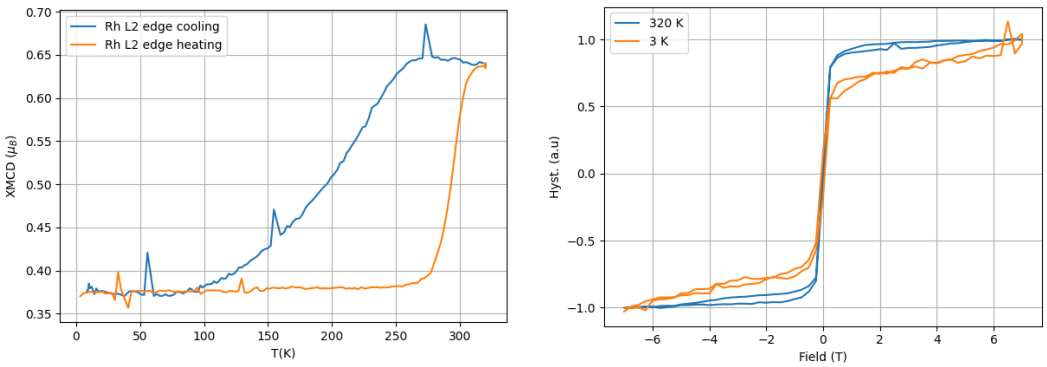

Figure 4.24: Magnetic moment as function of the temperature and hysteresis loops

Magnetic moment as function of the temperature for 7 T (left) and the hysteresis loop normalized for 3 K and 320 K (right)

the metamagnetic transition at 325 K in the heating up branch posses an opening in the saturation region, this phenomena is also observed in the Rh L edge (Figure 4.24) for 320 K. This opening is also shown for FeR 150 nm film over MgO done by sputtering [28](Figure 1.5) suggesting that this opening is observable when a hysteresis loop is performed in the region of the metamagnetic transition.

All the magnetic moment obtained from XAS/XMCD at the Fe L edge are summarized in the table 4.2.

Banch	Temp	m_{Seff} (μ_B)	m_{Orb} (μ_B)	m_{Total} (μ_B)
Cooling	350 K	1.4±0.1	0.1±0.1	1.5±0.1
	300 K	1.6±0.1	0.2±0.1	1.8±0.1
	250 K	1.7±0.1	0.2±0.1	1.9±0.1
	200 K	1.4±0.1	0.2±0.1	1.6±0.1
	100 K	1.4±0.1	0.1±0.1	1.5±0.1
	4 K	1.2±0.1	0.2±0.1	1.4±0.1
Heating	100 K	1.2±0.1	0.2±0.1	1.4±0.1
	200 K	1.2±0.1	0.1±0.1	1.4±0.1
	250 K	1.3±0.1	0.1±0.1	1.4±0.1
	300 K	1.6±0.1	0.2±0.1	1.8±0.1
	350 K	1.4±0.1	0.2±0.1	1.5±0.1

Table 4.2: Magnetic moment for Fe in FeRh nanocluster assembled.

Summary off all the magnetic moment obtained from XAS/XMCD at the Fe L edge for FeRh 150 nm nanocluster assembled film

4.4 Discussion

Thanks to RBS, now we know that the FeRh concentration of the nanocluster assembled film is 50%/50%±4%, and since the cluster preparation technique used in this thesis is always the same, we can assume that the same concentration is obtained for all samples studied in Chapter 3 and Chapter 5.

Anyway it is quite possible to have Fe_XRh_{1-X} with X<50% as iron oxide is also observed in XRD, leading to Rh in excess. From the phase diagram for FeRh bulk [9] it may be removed 9% of the iron giving a relative concentration of Fe/Rh 45%/55% in B2 phase, being in the limit to have metamagnetic transition. So, even if 9% of the iron atoms are remove in a FeRh nanoparticles with size ∼100 nm it may still has metamagnetic transition. Moreover, as it was mentioned previously in chapter 3, the bulk phase diagram may not be extrapolated at nanoscale.

Regardless the concentration of the FeRh B2 phase, the metamagnetic transition is observed. From cross section observations, we can speculate that it may exist a critical radius that determine if a nanoparticle posses metamagnetic transition or not. Bigger size nanoparticles may correspond to the magnetic contribution that switch between antiferromagnetic and ferromagnetic while the small nanoparticles remain at the ferromagnetic regime as it happens for diluted nanoclusters (See chapter 3).

If this is the case the top region (and the lower region in contact with SiO) may contribute mostly with ferromagnetic signal while the inner region with the metamagnetic transition. This can be observed comparing FY (that carried information from all the sample) vs TEY (that carried information of the first layers)

due to the fact that FY prove all the sample while TEY only probe the upper part.

But since is not possible to remove the oxide component for the FY signal it can be used as the XMCD/XAS ratio at the L_3 peak was used and it is noticeable a big diference in the opening of the metamagnetic transition corroborating that the inner portion contribute with most of the metamagnetic transition (Figure 4.21).

Chapter 5

Nanocluster over perovskite substrates

In this chapter is studied the magnetic, crystalline and chemical properties of FeRh nanocluster when they are deposited on perovskite substrates as STO and BTO, including the study of the phase transition from A1 to B2 phase, metamagnetic transition and epitaxy.

5.1 Sample preparation

Commercial $SrTiO_3$ or STO (100) were used as substrate, the surface was treated at *École Centrale de Lyon* (ECL) using buffered oxide etch for 30 sec (BOE) and then annealed at 1100 °C for 2 hours in the air. Then the substrates are transported to PLYRA where they are pre-annealed at 440 °C for 30 minutes in-situ where the FeRh nanoclusters were deposited in the UHV chamber.

Before pre-annealing at PLYRA the substrates present well defined 1-cell step (3.9 ± 0.1 Å) observed in atomic force microscopy at the *Centre Lyonnais de Microscopie* CLYM (See Figure 5.1 A, C and D). The height distribution over one terrace indicates variations of one crystalline cell at most (See Figure 5.1 B).

After the substrate is pre-annealed at PLYRA it keep the steps height and, the shape of the terraces get squared due to the crystal shape of the STO (See Figure 5.2).

To corroborate the proper deposition of FeRh nanoparticles and their attachment on the substrate, a non-covered FeRh nanocluster film with 3 nm monomer size and 2 Å of equivalent thickness, was deposited on the STO substrate.

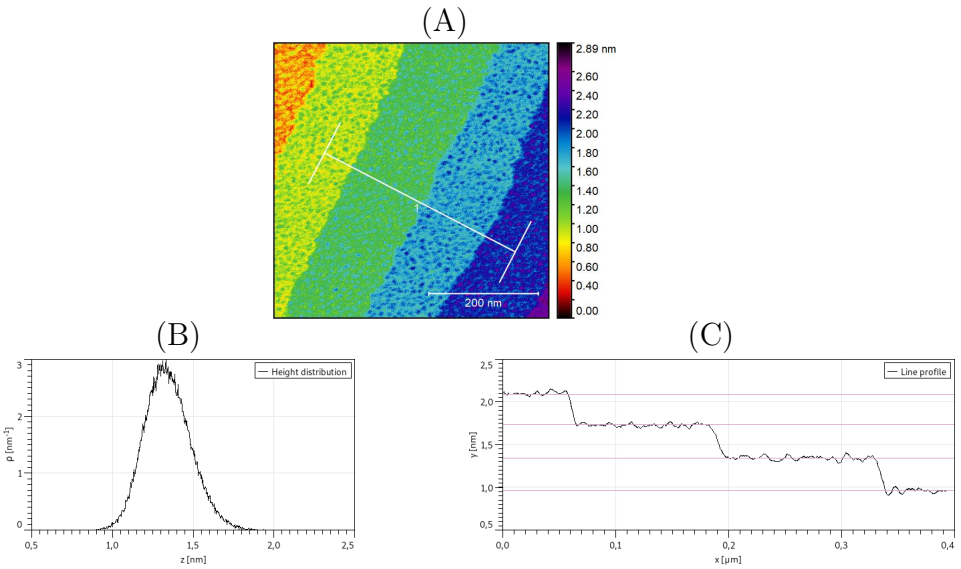

Figure 5.1: Atomic force microscopy image of a STO substrate after treatment at ECL.

Atomic force microscopy image of STO (A) with the size distribution over the terrace at 1.3 nm (B) and the line profile (C) before preannealing.

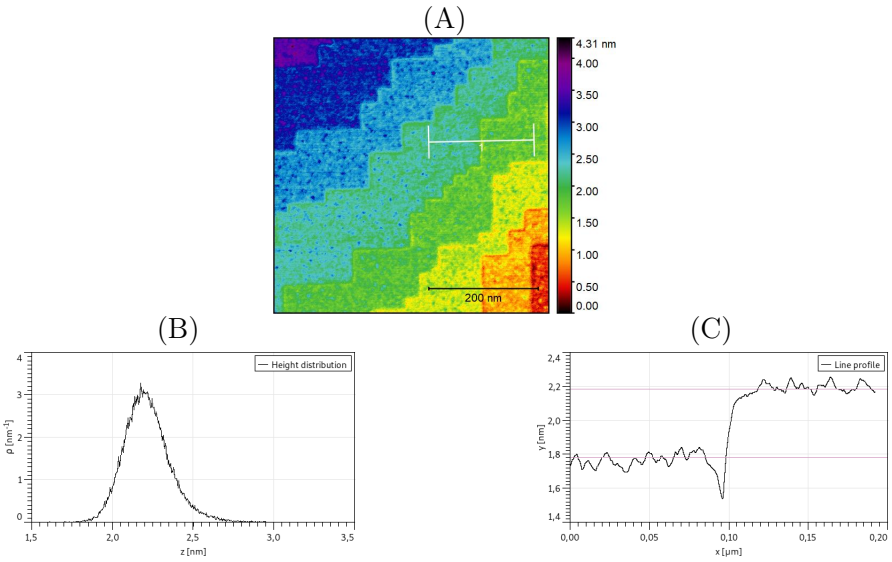

Figure 5.2: Atomic force microscopy image of a STO substrate after pre-annealing at PLYRA.

Atomic force microscopy image of STO (A) with the size distribution over the terrace at 1.3 nm (B) and the line profile (C) after preannealing.

On atomic force microscopy is possible to observe the nanocluster and the substrate step behind for the sample as prepared. The linear relation between the area and the perimeter indicate the necklace model (Figure 5.3 A and B).

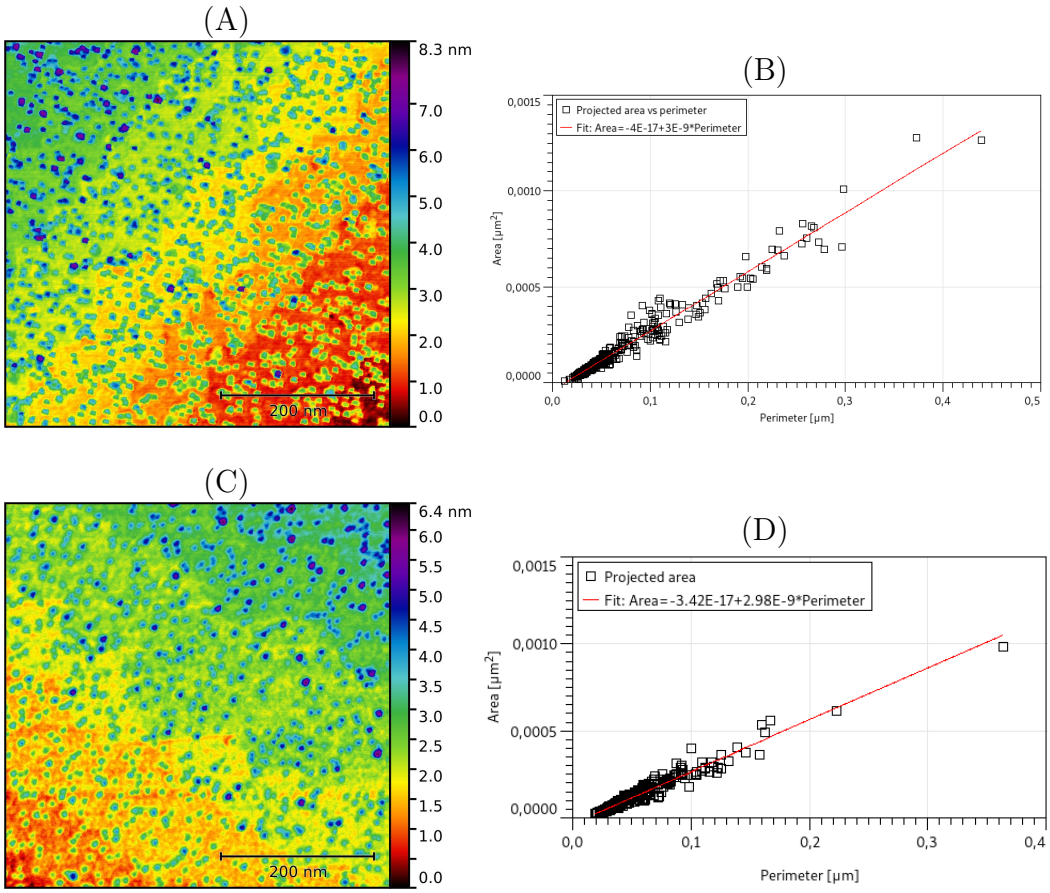

Figure 5.3: Atomic force microscopy image of a STO substrate.

Atomic force microscopy image of FeRh nanocluster of 3 nm monomere size over as prepared over STO (A) with the correspondent the area vs perimeter relation (B) and for the same sample annealed at 700 °C for 3 hours the AFM image (C) with its area vs perimeter relation (D).

After annealing at 700 °C for 3 hours in UHV, the sample remains without coalescence described by the necklace model (Figure 5.3 C and D), this is an indicator that the FeRh nanoparticles over STO posses less mobility than FeRh nanoparticles in carbon matrix annealed in the same condition where coalescence clearly occurred (Figure 5.3)

For BTO substrates, the preparation process at *École Centrale de Lyon* corresponds to radiofrequency sputtering at atmosphere of Ar_2:O_2 4 to 1 ratio and 10×10^{-2} mbar.

All samples have been prepared at PLYRA using the LECBD technique. Some samples were covered with amorphous carbon layer in-situ at UHV after deposition. Nevertheless, we systematically detected oxide contribution for all samples deposited on perovskite oxides after being transfer in air from XAS and XPS measurements at Fe edge.

5.2 Oxide reduction

In order to understand more about the oxidation of the NP and to determine a procedure to reduce them back to their metallic state, we followed the steps.

1. The NbSTO substrate was introduced in the UVH chamber and cleaned by a simple UHV 200°C annealing.
2. 1.4 Å of non mass selected FeRh nanocluster were deposited.
3. The sample was in-situ annealed at 470 °C for 1 hour.
4. The sample was in-situ annealed at 560 °C for 1 hour.
5. sample was exposed to air and reintroduced in the UHV chamber.
6. The sample was annealed at 400 °C for 1 hour.
7. The sample was annealed at 700 °C for 2 hour.

Between each step, XPS spectra of the main core levels of the FeRh/STO surface were measured, without breaking the vacuum. For these measurements, a standard non monochomatized XPS source with Al anode is used at the PLYRA. The measurements of the Fe 2p core level spectra of the FeRh nanoparticles after the steps 2 to 7 are presented in the Figure 5.4.

On Figure 5.4 there is no noticeable difference at the Fe2p edge between as-prepared and annealed sample up to 560 °C before its transfer in air where spontaneous iron oxidation occurs. The shift can produced by oxidation can be observed in the work of Ruwisch [103] and the value of the metallic Fe L3 peak of 707 eV was taken from the *Handbook of X-Ray photoelectron Spectroscopy* of John F. Moulder *et al* [102].

After UHV XPS sample re-introduction, a narrow metallic peak have been recorded after B2 phase transition upon *in situ* annealing 2 hours at 700 °C. This means that no chemical reactivity occur during UHV annealing at the interface between metallic FeRh nanoparticle and perovskite oxide.

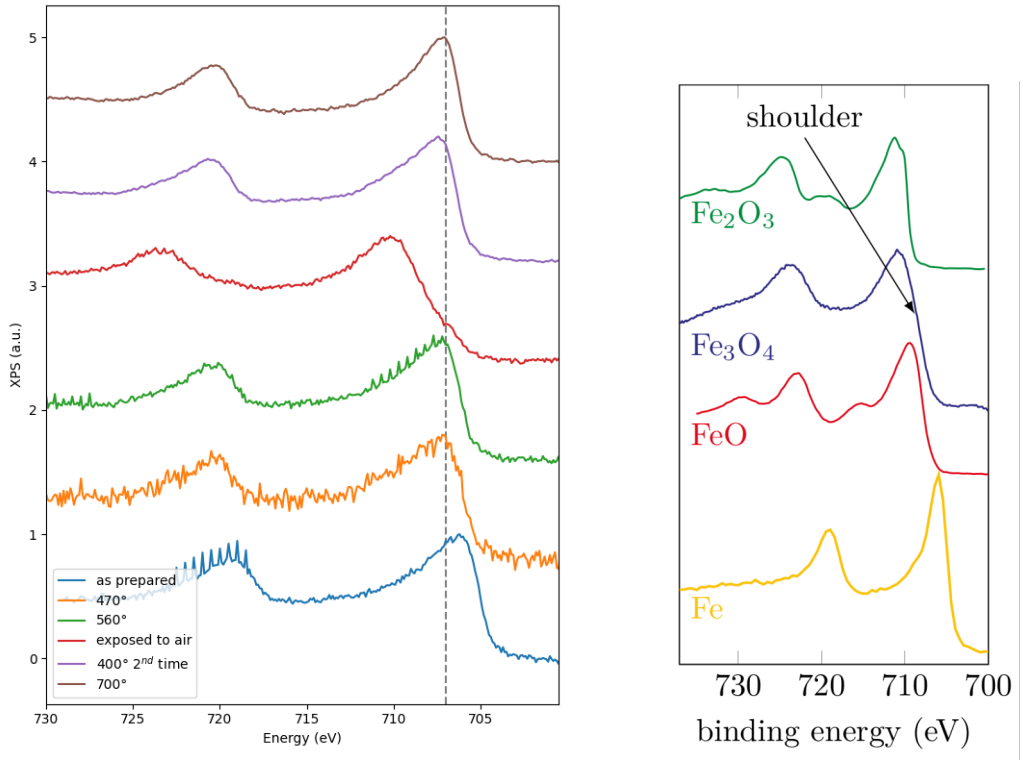

Figure 5.4: XPS at different annealing for FeRh non mass selected nanocluster.

On the left XPS for a non mass selected FeRh nanocluster over STO without carbon capping *in situ* as prepared in UHV (blue), after been annealed *in situ* at 470 °C (orange) for 1 hour, after been annealed *in situ* at 560 °C for 1 hour (green), after been exposed to the air (red), after been re-inserted in UHV and annealed at 400 °C for 1 hour and then been annealed at 700 °C for 2 hours. On grey dashed line is the reported value for the Fe metallic L3 peak [102]. On the right the Fe L edge XPS reference used by Ruwisch *et al* [103] for different configuration of iron oxides.

But how to explain that samples over perovskites with carbon capping are oxidized after been exposed to the air and that iron oxide can also be reduced by annealing in the same way as for the sample non covered by carbon capping. This phenomena may suggest that the carbon capping is not a good protection against the oxidation for FeRh nanoparticles deposited on oxide perovskite contrary to samples on Si substrate.

The best hypothesis is that the carbon capping behave differently over different substrates, being efficient for Si substrate as seen for FeRh nanoparticles embbeded in carbon matrix on inert Si substrate (Figure 3.11) but not over perovskite substrate.

By raising the question of how the oxidation occurs in FeRh nanoparticles deposited on STO with carbon capping, some assumptions are proposed below:

1. The carbon capping has low adherence on the perovskite and peels off from the substrate in some regions.
2. When in contact with perovskite and metallic FeRh NPs, the carbon capping perceives chemical or structural changes that make it permeable to the air oxygen at the sample surface.
3. The perovskite substrate is the source of iron oxidation due to oxygen transfer via carbon coating.
4. Charge decompensations in the substrate make it release oxygen [104].

In order to discard some hypotheses the following reasoning/procedure were done:

- Hypothesis 4 was discarted due to the fact that test done over a grounded sample reveal no difference in the oxidation process.
- Hypothesis 3 implies a chemicall process over the carbon capping across its 2 nm thickness, if there is no released element is unlikely to have an surface interaction that make all 2 nm Carbon capping permeable.
- And if there is Oxygen released by the substrate, corresponding to hypothesis 2, it does not explain the absence of oxidation in FeRh peak observed in XPS before transfer in air (Figure 5.4).

Is also worth to mention that Catrou et al [105] have shown that a limited reaction occur at the interphase between Fe and STO, leading the formation of Oxygen vacancies at the interphase with a charge concentration.

Notice that extensive studies on oxide-supported metal catalysts suggest that complex Strong Metal Support Interactions (SMSI) influenced by the nature of metal/oxide interface commonly occur to explain for example, loss of chemisorption capacity toward H_2 and CO of noble metal nanocatalysor as platinium [106]. In particular, they mention that encapsulation processes are observed for TiO_2- supported metals NPs with high surface energy, such as Pt ($2.7\,J/m^2$), Fe ($2.9\,J/m^2$), Pd ($2.0\,J/m^2$), and Rh ($2.8\,J/m^2$), but not for metal with low surface energy, such as Au ($1.6\,J/m^2$). They show that upon high-temperature annealing under ultra-high vacuum (UHV) conditions, supported Pt-group NPs with larger sizes were more facile to be encapsulated by TiO_{2-X} overlayers but that encapsulation process

did not occur upon vacuum annealing below 500 °C. Such phenomenon are also observed for Pd nanoparticles on Nb-STO substrate [107].

So finally the hypothesis 1 seems to be the most feasible hypothesis, since it may be not a complete peel off. Even if a black carbon capping shadow is visible by eyes on the top of sample, we can notice from optical microscopy that gray tones contrast regions are visible that may correspond to areas with and without carbon capping (Figure 5.5).

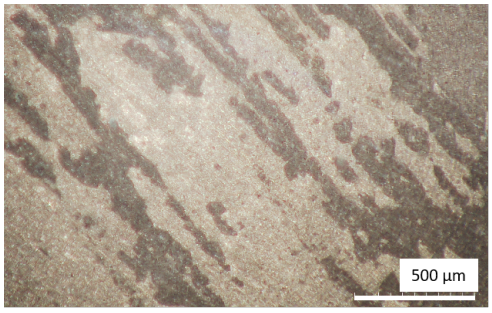

Figure 5.5: Optical microscope image of the carbon capping on STO.

Nevertheless, the *in situ* annealed has proven to be an effective way to reduce the oxidation on FeRh nanoparticles over STO.

5.3 Epitaxy

GIWAX was performed on a sample of FeRh nanocluster with 3 nm of nominal nanoparticle size and 5 Å of equivalent thickness and capped with carbon at BM32-ERSF Synchrotron facilities. Using x-ray at 1.58 keV for 0.78 Å wavelength with incidence angle $\alpha = 0.118464°$.

Two main epitaxies were identified. The first one is FeRh[110]//STO[010] and FeRh[1$\bar{1}$0]//STO[100] presented in the Figure 5.8 which correspond to the most stable configuration of epitaxy for bcc metals over STO and it will be called epitaxy $E1$. While the second epitaxy identified is FeRh[100]//TO[100] with FeRh[010]//STO[010] presented in Figure 5.7 is the second most stable configuration for bcc metals over STO (and the most stable for fcc metals over STO) and it will be called epitaxy $E2$ [108, 109]. Both epitaxies are represented in the Figure 5.6.

The stability of the epitaxy for metal films (that form islands) grown over TiO_2 terminated STO according to Werner [108, 109] is determined by the oxygen affinity of the metal as well the respective surface energy. But the samples prepared

in this work does not grown in the substrate neither are films, they correspond to nanoparticled formed in gas phase and deposited on substrate at low energy (section 2.3). Nevertheless the fact that the same epitaxies are observed may be an indicator of the positioning of Fe over the Oxygen atoms as observed from our X-ray spectroscopy experiments.

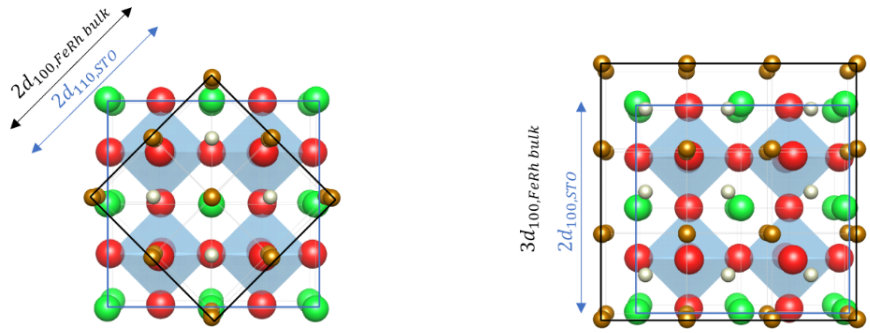

Figure 5.6: Epitaxies found by GIWAX for FeRh nanocluster on STO

On the left, the $FeRh[110]//STO[010]$ and $FeRh[1\bar{1}0]//STO[100]$ (E1) epitaxy and on the right the $FeRh[100]//STO[100]$ and $FeRh[110]//STO[110]$ (E2) epitaxy.

The presence of the B2 FeRh diffraction rings observed by average GIWAXS techniques techniques on a numerous annealed nanoparticles (as seen in Figures 5.7 and 5.8) indicates that not all nanoparticles present epitaxy.

To identify local epitaxy and potential deformation on a single nanoparticle due to the epitaxy, high resolution STEM was performed (Section 2.4) on a cross section lamella of FeRh nanocluster with 3 nm monomer size and 0.8 Å of equivalent thickness over STO[001] and covered by amorphous carbon (Same as the sample used for GIWAX but with lower density of nanoparticles). This is presented in Figure 5.9.

In Figure 5.9 (A) we see the original STEM-HAADF image of the 3 nm nanoparticle on zone axis $[11\bar{1}]$ with epitaxy in the direction FeRh[011]//STO[010] along the fast Fourier transform. While in the Figure 5.9 (B) we see the positions detected with the angle reference used in the analysis.

The epitaxy configuration observed in Figure 5.9 and represented in Figure 5.10is not one of the options considered in Figure 5.7 and Figure 5.8, neither and configuration reported [108, 109]. This observation suggests that minor epitaxial relationships exist in the system FeRh nanoclusters on STO different from the main ones determined using GIWAXS.

In the table 5.1 are presented the epitaxies observed in GIWAX (Figure 5.7 and 5.8) and by STEM cross section (Figure 5.9). It can be noticed that up to 13% of

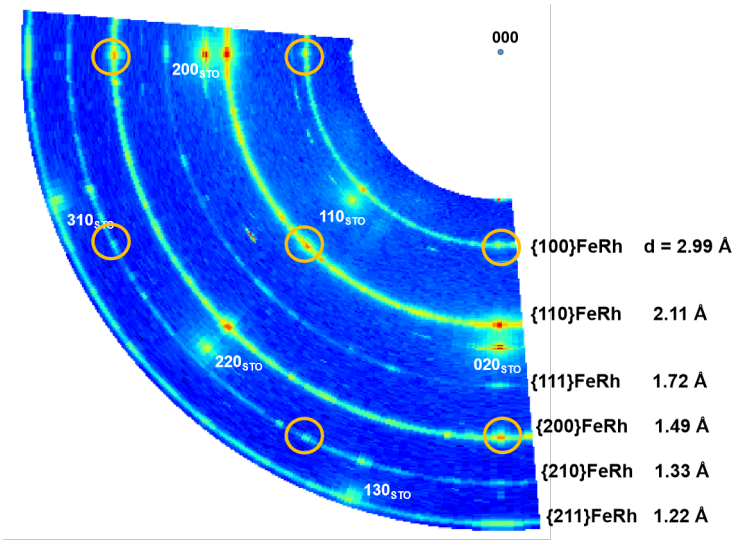

Figure 5.7: GIWAX for FeRh nanocluster on STO

GIWAX for FeRh 3 nm nanocluster over STO, in yellow rings is indicated the epitaxy FeRh[100]//STO[100] with FeRh[010]//STO[010]

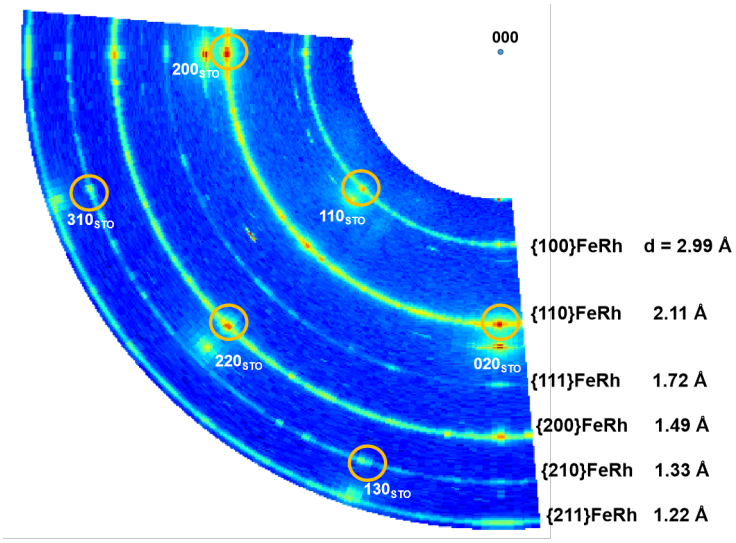

Figure 5.8: GIWAX for FeRh nanocluster on STO

GIWAX for FeRh 3 nm nanocluster over STO, in yellow rings is indicated the epitaxy FeRh[100]//STO[110] with FeRh[110]//STO[010]

misfit can be achieved, this implies strong strains in the FeRh nanoparticles.

On the Figure 5.11 is shown STEM-EELS images for the Fe L and Ti L edges, where is possible to observe the absence of encapsulation to Ti around the nanopar-

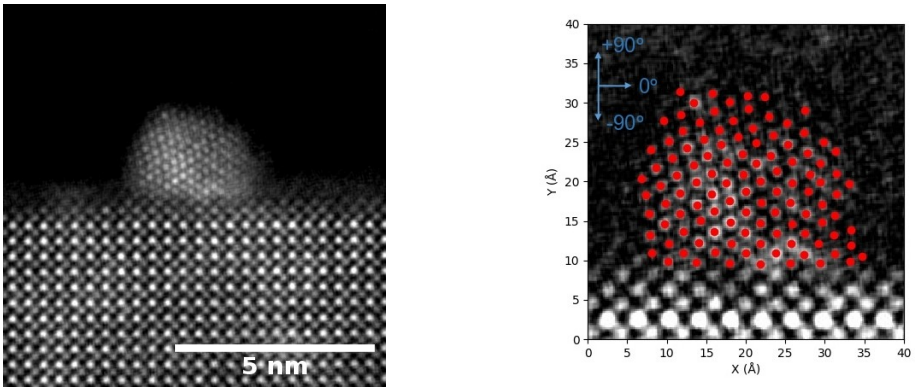

Figure 5.9: STEM cross section of a 3 nm FeRh nanoparticle over STO[001]

(Left) High resolution STEM-HAADF image of a 3 nm FeRh nanoparticle over STO[001] and (right) the positions of FeRh columns identified by the program are indicated by red circles, the reference coordinates used to measure the angle of the path to the first neighbo rare indicated in blue.

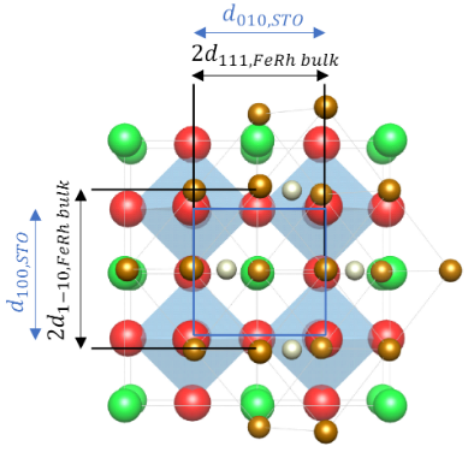

Figure 5.10: Epitaxy found by STEM cross section for one FeRh nanoparticle on STO

Thehe FeRh[011]//STO[100] & FeRh[11$\bar{1}$]//STO[010] (E3) epitaxy.

ticle contrary to the observed in other work on Metals over titanates [104,107,110].

On the HAADF image 5.12 is possible to observe that the substrate is Ti terminated in the interface with the nanoparticle.

To study potential relaxation effects on the nanoparticle observed in Figure 5.9 (A) it was registered each position found. On the Figure 5.9 (B) is marked in red each position detected and for each of them the distance and angle of each

Notation	Epitaxy	Misfit direction	Misfit
E1	FeRh[110]//STO[010] & FeRh[1$\bar{1}$0]//STO[100]	$\epsilon_{110/010}$	-7.43%
E2	FeRh[100]//STO[100] & FeRh[010]//STO[010]	$\epsilon_{100/100}$	-12.73%
E3	FeRh[011]//STO[100] & FeRh[11$\bar{1}$]//STO[010]	$\epsilon_{011/100}$ $\epsilon_{111/010}$	-7.42% 13.39%

Table 5.1: Epitaxies observed for FeRh nanoparticles over perovskite

Epitaxies configurations with their respective misfit for FeRh nanocluster over STO

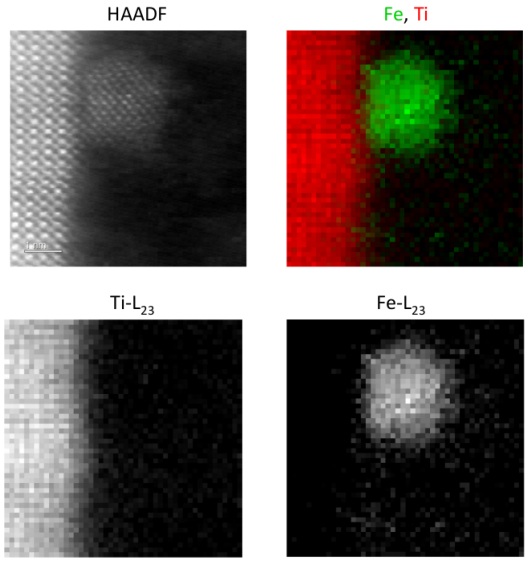

Figure 5.11: STEM-EELS over a 3 nm FeRh nanoparticle over STO.

STEM-EELS at the Fe L edge and Ti L edge for a cross section lamella of FeRh 3 nm nanocluster over STO annealed 3H 700°

path to first neighbor was measured. The reference coordinate system used for the angles is presented in the corner. It is important to notice that the path to the first neighbor does not have a preferred direction so the angle can be defined in a range of 180°.

Each path obtained from Figure 5.9 (B) was plotted in Figure 5.13 to identify the most frequent paths in the nanoparticle. It is possible to observe that five main cloud of path configuration are present.

To simplify the obtained groups of path to the first neighbor in Figure 5.13, a density map of path configurations was done, this allow the fit of 2D gaussians. The best fit was done with five 2D gaussians as presented in the Figure 5.14 and the respective fitting values are in the table 5.2.

One hexagonal-like pattern should have 3 distance/angle configurations for

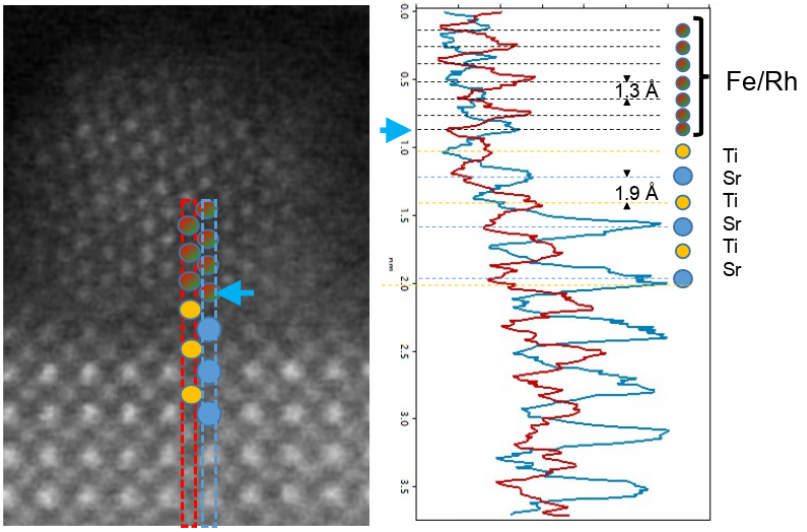

Figure 5.12: HAADF over a 3 nm FeRh nanoparticle over STO.

HAADF for a cross section lamella of FeRh 3 nm nanocluster over STO annealed 3H 700°

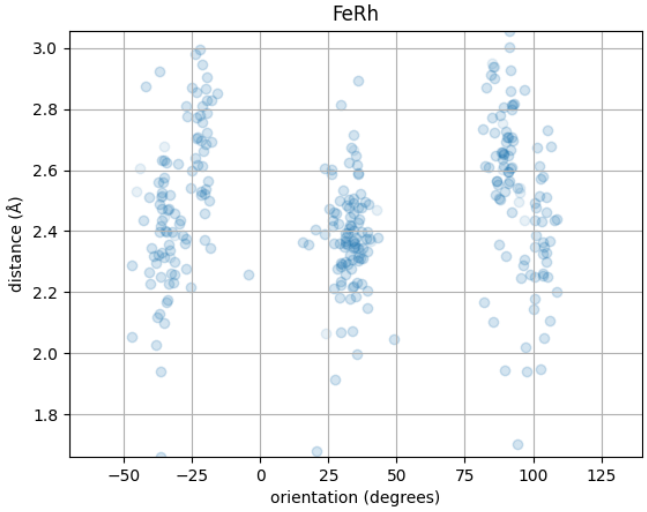

Figure 5.13: Distance and orientation for paths to first neighbor.

Map of pairs angle/distance for all path to first neighbors detected in Figure 5.9.

paths to first neighbors (under the angle reference established in Figure 5.9). From the Figure 5.9 we can clearly identify that all the nanoparticles posses hexagonal-like pattern, but on the Figure 5.13 and table 5.2 is exposed 5 main distance/angle configurations for paths to first neighbors. This indicates the presence of more than

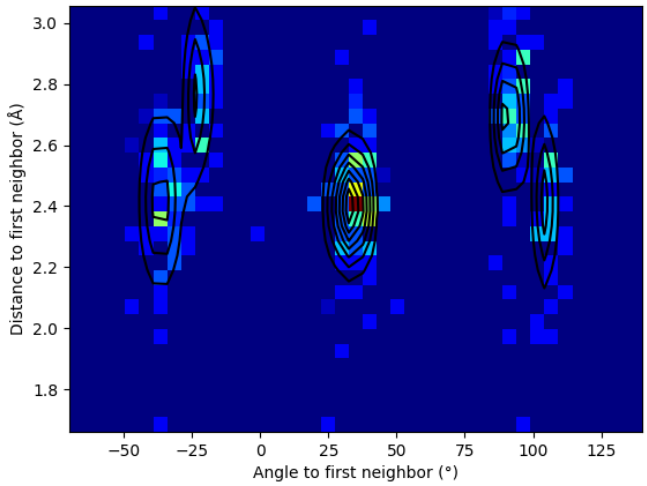

Figure 5.14: Density map of the distances vs angle for paths to first neighbors

Density map version of the Figure 5.13, where red indicate the most recuent configuration and blue the absesnce of that configuration. On black the contour lines of a five - 2D Gaussians fit

$Mean_{Angle}$	σ_{Angle}	$Mean_{Distance}$ (Å)	$\sigma_{Distance}$ (nm)	Amplitude (a.u.)
33°	7°	2.4	0.2	12.0
-23°	5°	2.7	0.3	5.0
105°	4°	2.4	0.2	5.4
91°	5°	2.7	0.2	7.7
-36°	7°	2.4	0.3	5.5

Table 5.2: Parameters of the gaussian fit for the density map of distances vs angle

For each gaussian fit on the density map the fitted value of the angle ($Mean_{Angle}$), the angle deviation (σ_{Angle}), the fitted value of distance ($Mean_{Dinstance}$), the distance deviation ($\sigma_{Distance}$) and the amplitude of the respective gaussian fit.

one hexagonal-like pattern.

Exploring options of 2 hexagonal-like patterns with one common distance/angle configuration it was found the hexagonal-like patterns:

- 1: 33° 2.4 Å, −23° 2.7 Å, 105° 2.4 Å
- 2: 33° 2.4 Å, −36° 2.4 Å, 91° 2.7 Å

If we mark the hexagonal-like pattern 1 as blue and the hexagonal-like pattern 2 as red we obtain the Figure 5.15 where we can observe that we retrieve the

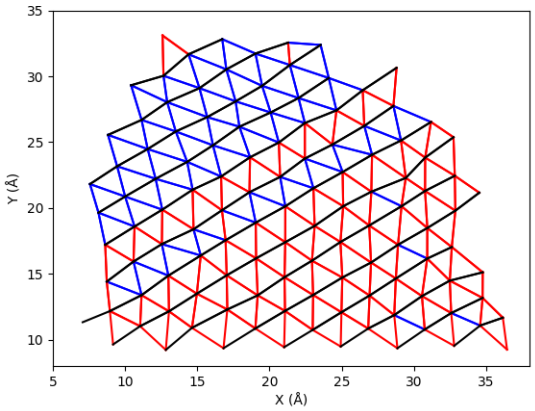

Figure 5.15: Structural analysis of a FeRh NC in epitaxy on STO (001).

All paths to first neighbor in the nanoparticle observed by STEM cross section. $-23°$ and $105°$ in blue, $-36°$ and $91°$ in red and $33°$ in black.

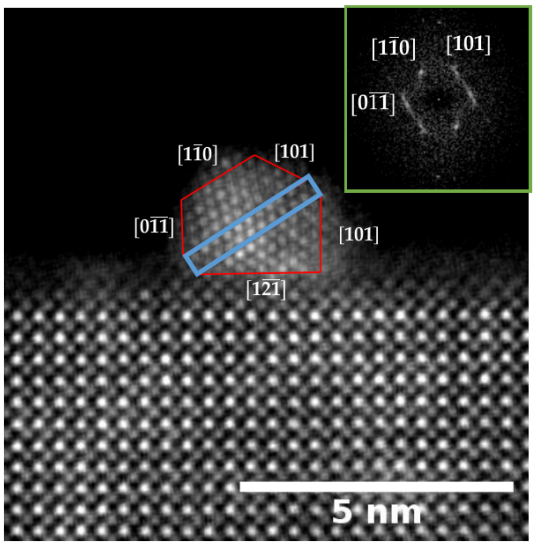

Figure 5.16: Crystalline regions identified for Figure 5.9.

On blue the twinning region, on red the plane directions mirrored on the twinning region, and on the insert the FFT for the FeRh nanoparticle over STO

twinning on the nanoparticle. Both configurations indicate a deformation of the nanoparticle crystal, but there is no sign of higher strain in a particular position of the nanoparticle.

The twining domains can also be identified by eye in the Figure 5.9, on the Figure 5.16 is indicated the twining regions and the transition region with the

respective crystalline planes. The obtained twinning is not a possible configuration of a perfect bcc crystal [111], indicating that the twinning is a proof of the deformation by stress over the nanoparticle.

5.4 Magnetic properties

Samples over perovskite substrates correspond to only one layer of FeRh nanocluster (with equivalent thickness lower than 1nm), this implies that the amount of FeRh is low and not enough to measure the magnetic properties from SQUID magnetometry, because of this the magnetic properties of FeRh nanocluster were measured by high sensitive X-ray magneto-optic spectroscopy techniques in DEIMOS-SOLEIL synchrotron facilities.

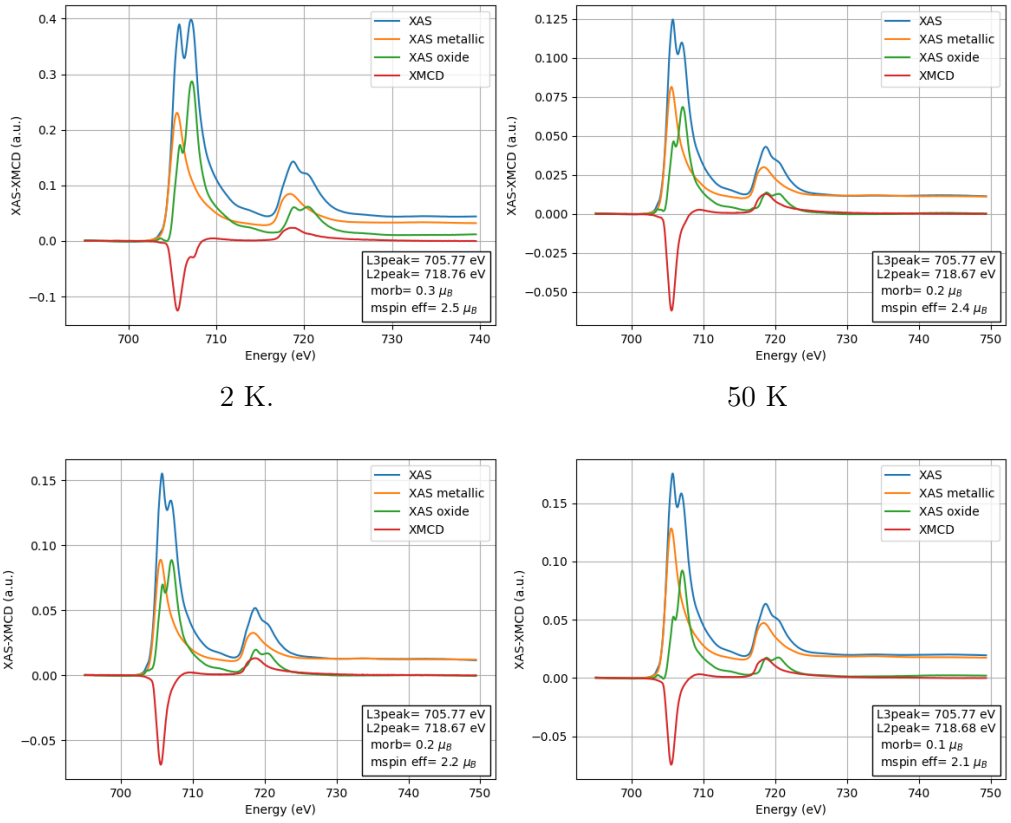

2 K. 50 K

250 K 350 K

Figure 5.17: Normal incidence XMCD for P1

XMCD treatment for temperatures from 4 K to 300 K for normal incidence X-rays

A sample of FeRh 3 nm monomer size nanocluster with nominal equivalent thickness of 5 Å over STO and covered by two layers of carbon capping (4 nm nominal thickness) was measured from XAS/XMCD. This sample will be refered as P1. For normal incidence X-ray is possible to observe the Fe L edge XAS/XMCD spectra in Figure 5.17.

To separate the metallic contribution from the oxidized one in the XAS signal of FeRh samples on perovskite, we used as reference the metallic XAS obtained on FeRh nanocluster in carbon matrix previously showed in Chapter 4 (see Figure 3.11). Then the following steps were done:

- The reference XAS Fe L3 peak was shifted to match the energy of the negative peak of the XMCD
- The reference was multiplied by a factor to make the reference XAS intensity as big as possible without surpassing the XAS of the data to treat.
- To determine the magnetic moment, it was assumed that the contribution of the oxidized Fe to the XMCD signal is negligible: It was used the XAS of the reference with the XMCD of the data to treat to perform the sum rules as mentioned in Chapter 1.

It is possible to observe in the Figure 5.17 that the sample presents a considerable oxide contribution at all temperatures, but also that the XAS intensity at the metallic on to Oxide ratio at the Fe L3 edge is lower at 2 K, making the XMCD contribution of the Oxidized Fe notorious.

We have also measured the XAS/XMCD for the sample P1 at grazing incidence, 40° inclination from the zenith, plot in the Figure 5.18

On Figure 5.19 we can see that for both configurations, the sample P1 presents a ferromagnetic behaviour. The increase of magnetic moment at 2 K over the ferromagnetic tendency can be attributed to the fact that the XMCD contribution from oxide is not negligible at that temperature (See Figures 5.17 and 5.18)

The same process has been realized on an other FeRh sample with 7 nm monomer size nanocluster, a nominal equivalent thickness of 10 Å over BTO and covered by two layers of carbon capping (4 nm nominal thickness), this sample will be refered as P2.

In Figure 5.20, it can be observed the XAS/XMCD spectra for the sample P2 at different temperatures for normal incidence X-ray. On this image we can notice that the behaviour for Sample P2 over (BTO and 7 nm nominal monomere size) does not present a relevant different behaviour compared to the one of P1 over

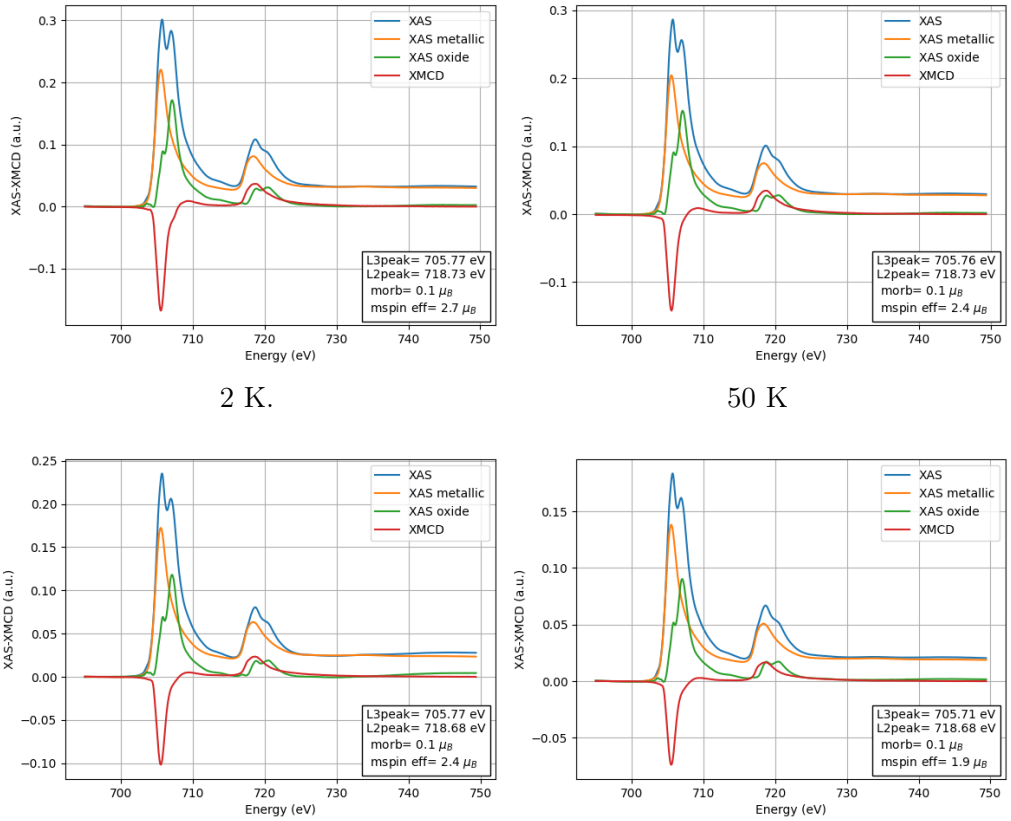

2 K. 50 K

250 K 350 K

Figure 5.18: Grazing incidence XMCD for P1

XMCD treatment for temperatures from 4 K to 300 K for grazing incidence X-rays

(STO and 3 nm nominal monomere size). Even the oxide component obtained in the XAS at the Fe L edge posses similar shape.

Finally, the Curie temperature was explored on a low density sample of FeRh 3 nm monomer size with 0.5 Å of equivalent thickness over NbSTO after *in situ* annealed up to 1000K, this sample will be called P3.

XMCD valley at the L3 region were measured on-the-fly for P3 while increasing the temperature from 350K to 640 K. A XAS/XMCD at the Fe L region (Figure 5.21) was used to obtain a magnetic moment as reference for the on-the-fly measurement observed in the Figure 5.22 .

It is possible to observe in the Figure 5.22 that a ferromagnetic behaviour is qualitatively observed in all the range of temperature.

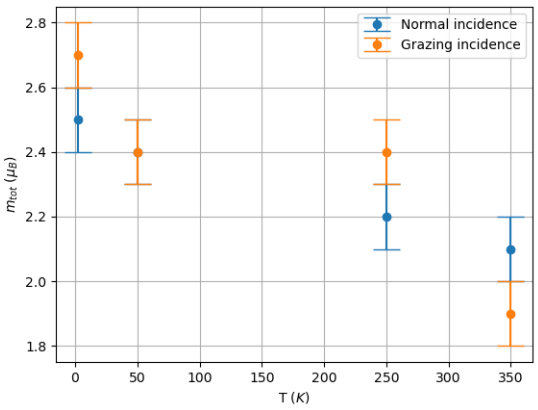

Figure 5.19: Magnetic moment for P1.

Magnetic moment as function of the temperature for FeRh 3 nm nanocluster over STO covered with carbon layer.

Surprisingly, the fit on Figure 5.22 reveals that the curie temperature is around 650 °C as the value found in the phase diagrams of bulk FeRh but with the persistence of the ferromagnetic regime at low temperature for FeRh nanoparticles over STO. (see Figure 1.1)

On the talble 5.3 is shown the magnetic moment obtained for each XAS/XMCD measurement at the Fe L edge.

Sample	Temperature	Incidence	m_{Seff} (μ_B)	m_{orb} (μ_B)	m_{Tot} (μ_B)
P1	2 K	Normal	2.5±0.1	0.3±0.1	2.8±0.1
	50 K	Normal	2.4±0.1	0.2±0.1	2.6±0.1
	250 K	Normal	2.2±0.1	0.2±0.1	2.4±0.1
	350 K	Normal	2.1±0.1	0.1±0.1	2.2±0.1
	2 K	Grazing	2.7±0.1	0.1±0.1	2.8±0.1
	50 K	Grazing	2.4±0.1	0.1±0.1	2.5±0.1
	250 K	Grazing	2.4±0.1	0.1±0.1	2.5±0.1
	350 K	Grazing	1.9±0.1	0.1±0.1	2.0±0.1
P2	2 K	Normal	2.7±0.1	0.5±0.1	3.2±0.1
	50 K	Normal	2.4±0.1	0.2±0.1	2.6±0.1
	250 K	Normal	2.2±0.1	0.0±0.1	2.2±0.1
	350 K	Normal	2.0±0.1	0.1±0.1	2.1±0.1

Table 5.3: Magnetic moment for FeRh nanocluster over perovskite

Magnetic moment obtained from XMCD at the Fe L edge for FeRh Nanocluster over perovskite.

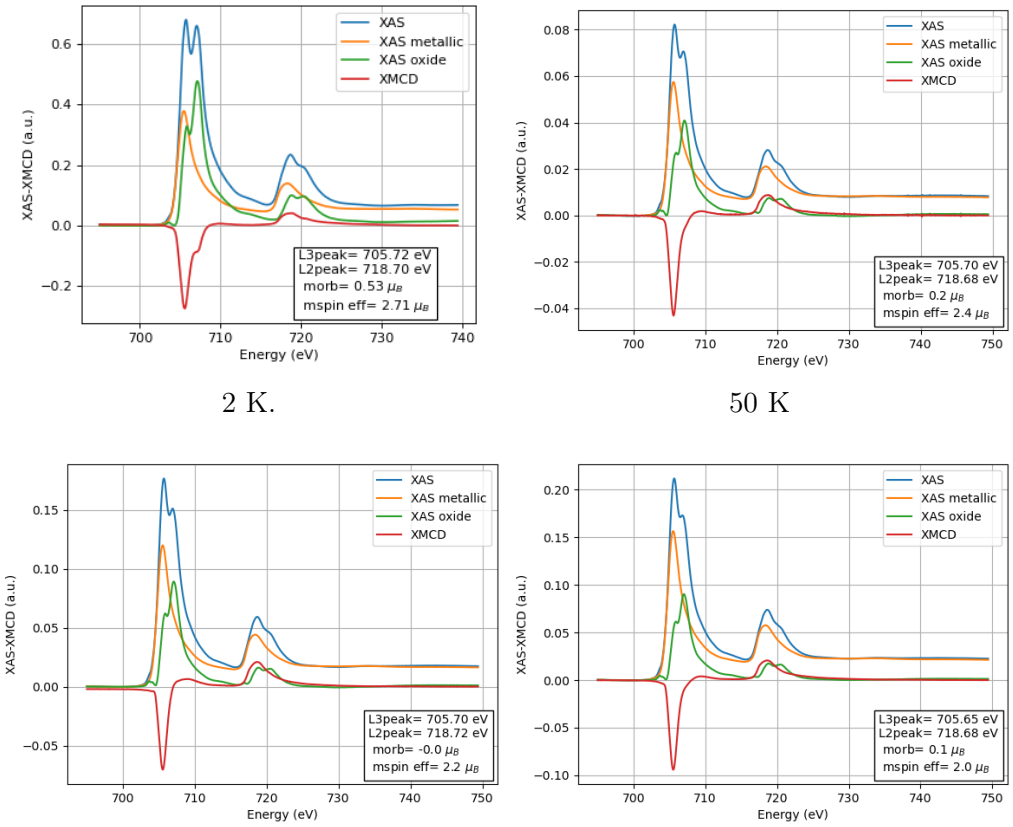

2 K. 50 K

250 K 350 K

Figure 5.20: Normal incidence XMCD for P2

XMCD treatment for temperatures from 4 K to 300 K for normal incidence X-rays

Figure 5.23 reveal that at low temperature there is no change in the hysteresis loop between for samples in carbon matrix and over STO.

5.5 Discussion

Due to the numerous factors that can affect the metamagnetic transition in such complex multiferroic system, here I'd like to evaluate each part, even if many questions remain unanswered.

From Chapter 4 we showed that the magnetic signal of the oxidized part is significantly lower than the one of FeRh B2 metallic phase, meaning that there is a small portion of Fe removed from the FeRh B2 phase. A small quantity of Fe

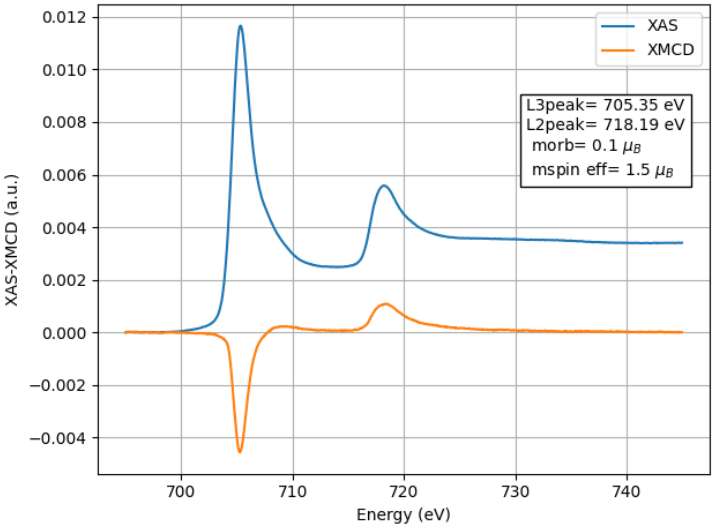

Figure 5.21: Normal incidence XMCD for P3

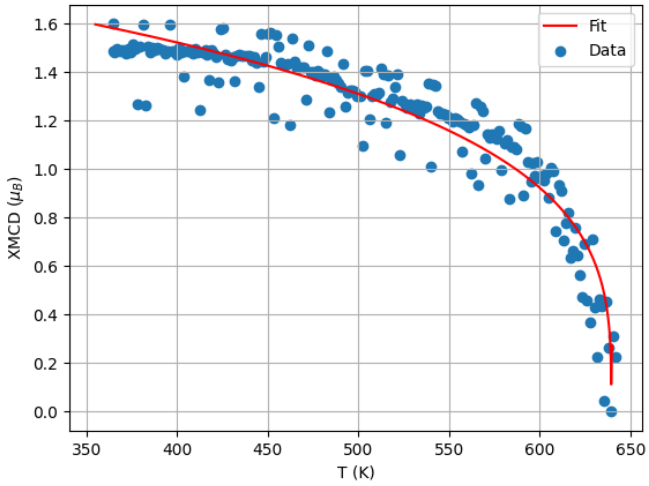

Figure 5.22: Magnetic moment as function of the temperature for P3

Magnetic moment obtained for on-the-fly XMCD measurement over sample P3 using XMCD done at 350 K as reference from Figure 5.21 with a fitting curve $C(1-t/t_C)^P$ with $C = 2\mu_B$, T_C =639 K and $P = 0.28$.

atoms removed from the FeRh B2 phase may change drastically the concentration, specially for 3 nm size nanocluster where the atoms at surface represent 35% of all atoms. According to the STEM-EELS cross section image (Figure 5.11) it does

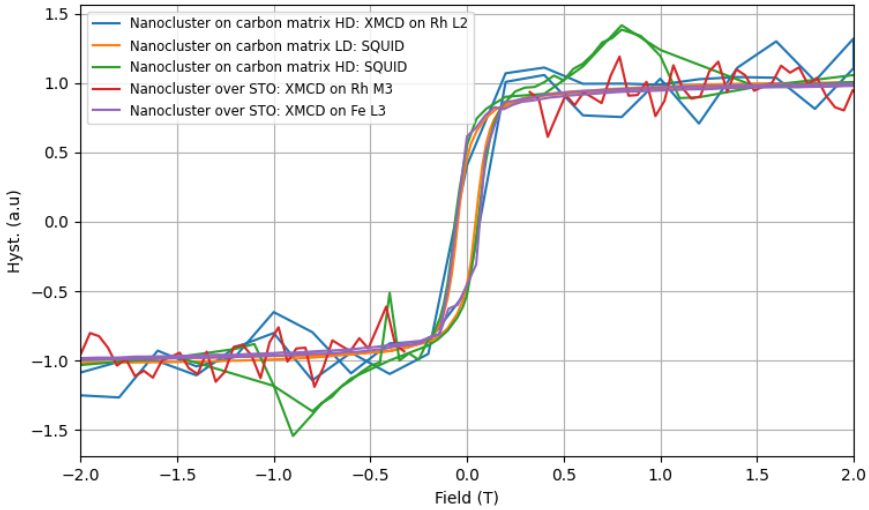

Figure 5.23: Hysteresis loops for different configurations

Hysteresys loops at 2K for FeRh nanocluster embedded in carbon matrix with both densities and FeRh nanocluster over STO, measured with SQUID and XMCD.

not seems that iron oxide is located at the FeRh surface.

Also the XAS oxide peak observed for FeRh nanocluster at Fe L3 edge looks similar to the one observed for the thick sample before *in situ* annealing (Figure 4.16) indicating that the portion of oxidation is not severally different.

A XMCD signature is always observed at both L and M Rh edge. As Rh is not magnetic by itself, the induced FM moment in Rh environment is a proof of the high hybridization between iron and rhodium by proximity effects. Moreover, the identical normalized m(H) hysteresis curves measured at L3 Fe edge (Figure 5.23) reveal as well a strong correlation between the magnetic behaviour of Fe and Rh species.

Regardless the oxidation, there are other factors that may change the magnetic behaviour for FeRh nanoparticles over perovskite, this is the fact that it posses epitaxy and the perovskite may contribute with a surface electron gas.

In the case of the epitaxy due to strain, we can notice that the nanoparticle observed in HAADF does not posses exactly the lattice parameter of perfect B2 crystal. Moreover the cross section technique is not enough to extrapolate a 3D crystal without incorporating any assumption or additional information due to the fact that in the image we observe a 2D projection of a crystal which correspond to four variables, and a 3D crystal has nine variables. In the Appendix F is explored how the crystal may look under one hypothetical cases. In 3D dimension, for such

epitaxy, we expect a contraction in the plane and a dilatation perpendicular to the surface contact (see table 5.1). From HAADF, the main configurations consisting in a contraction of the lattice parameter is only observed at the contact plane.

At first one could think that the epitaxy may change the magnetic anisotropy, and in effect is observed an in-plane magnetic anisotropy, but the same anisotropy is observed for nanoclusters in carbon matrix and so it can not be a product of the epitaxy, additionally is not observed magnetic anisotropy in diluted samples so everything indicate that the anisotropy of the system is an effect of in-plane the dipolar interaction.

Other difference between the FeRh nanoclusters in perovskite vs the FeRh nanoclusters in carbon matrix is the maximum magnetic moment achieve, being lower for the ones over perovskites even covering the same sizes. This indicates that there is an effect of the substrate on the nanoparticle magnetism.

A first option to explain the reduced maximum magnetization is the strain. For bulk the lattice parameter contraction is enough to switch from ferromagnetic to antiferromagnetic order; so is intuitive to think that the interatomic distance distortion can justify the different magnetic behavior in our case. To properly confirm this assumption, additional studies have to be done. It may be possible that for some epitaxies the nanoparticle achieve the $3\mu_B$ and for other epitaxies $O\mu_B$. To clarify this is necessary to study the magnetic behaviour of an individual nanoparticle in specific epitaxy and to corroborate with theoretical *ab-initio* calculations .

A second explanation correspond to the fact that the STO surface is not fully conductive, it has to be annealed in order to form oxygen vacancies and become conductive. So as the STO has not become enough conductive the charge released by XAS/XMCD will be trapped and in effectively charging the nanoparticle.

Chapter 6

General conclusions

On the different results presented in this work, it can be noticed a competition at nanoscale between the configurations at low temperatures of persistent ferromagnetic state and of stable antiferromagnetic state as expected in the bulk metamagnetic transition. The systems presented here explore different phenomena that may be essential for the metamagnetic transition, contrast them and derive new understandings.

In nanocluster embedded in carbon matrix, we confirm that dipolar interactions are not in favour of antiferromagnetic state at low temperature. Both density of nanoclusters per unit of area explored here as well other less dense nanocluster systems reported by others, maintain the persistent ferromagnetism regardless the method of preparation and the nanocluster shape. The fact that the diluted nanoclusters with 80% below 12 nm size remain ferromagnetic while the nanocluster assembled film with grains size of 25 nm does present the metamagnetic transition, shows that increase magnetic FeRh nanoparticle size is the main factor to induce this magnetic transition. Moreover, since the nanocluster assembled film presents a wide range of size, it is consistent with a non negligible fraction of ferromagnetic signal measured at low temperature. Then the triggering size D_T may be in the range 12 nm$< D_T <$25 nm.

Beyond the issue of size and of coordination effects, the study of nanoparticles over STO can bring valuable informations about surface interaction effects on the metamagnetic transition. Unlike to the films where the epitaxy is limited to 7% of misfit, the main result of our work is that many other epitaxies can be obtained for FeRh nanoclusters over STO (001) up to +/- 13 % of misfit. But the counter-productive result is that compression and expansion do not contribute in the same way according to the magnetic behaviour. Indeed we show that interface strain and change in lattice parameter, alter the direct surface exchange energy

leading to change in magnetization intensity but maintain in average the persistent ferromagnetism at all temperature.

More homogeneous volume constrain could be another possibility to explore by embedding the clusters in a compressive matrix. In that case, magneto-elastic energy related to a deformation of FeRh nanoclusters embedded in a matrix to constrain lattice fluctuation at the surface of the nanoparticle, could be in favor of antiferromagnetic order with more compensated spins.

The control of a system like FeRh metamagnetic transition is very important for prospects of using metamagnetic transition in devices. The voltage control contemplated in the VOLCONANO project aims to explore that. But other alternatives to re-shape the FeRh metamagnetic transition were found on this thesis. It was revealed that for FeRh nanocluster assembled film different behaviours, the persistent ferromagnetism as well the metamagnetic transition, may coexist. The residual ferromagnetism can be changed by the external field and but as well by the portion of small nanocluster bellow the trigering size. Moreover by controlling the external magnetic field is possible to achieve paths for each branch with many possible metamagnetic transitions. And if we take in consideration that the transition temperature is also modified then the shape of the metamagnetic transition present a wide range of potential modifications, allowing the option to engineer different metamagnetic transition using multi-size/shape configurations and specific temperature-field paths.

Appendix A

Magnetic moment obtained from XMCD

A series of scans alternating circular right and circular left polarization are acquired. These Scans are average to obtain an average over all scans that will be refereed as the XAS and the average for each polarization called CR (for circular right polarization scans) and CL (for circular left polarization scans).

A linear background is obtained from XAS in order to obtain a flat region post Fe L2. By definition this background will change the pre edge Fe L3 intensity, in order to keep comparable scales scales were shifted in intensity to left the pre-edge Fe L3 at 0.

If the sample does not present oxidation at this point is applied the sum rules.

To remove the oxidation it was used two assumptions:

- The XMCD signal can be assumed as originated only from the metallic Fe.

the XMCD signal can be assumed as originated only from the metallic Fe.

The error for a certain function of the form $F(x_1, ..., x_N)$ was obtained with the simplified version [112]:

$$\Delta F(x_1, ..., x_n) = \sqrt{\sum_{i=1}^{n} \frac{\partial F}{\partial x_i} \Delta x_i} \tag{A.1}$$

So for an integral I over an curve that correspond to the average of N scans, in a range E_{Range} with a total of P_{Range} points in that range and a noise of ΔX per point the error will correspond to :

$$\Delta I = \frac{1}{\sqrt{N}} \frac{1}{\sqrt{P_{Range}}} E_{Range} \Delta X \tag{A.2}$$

For the sum rules the integrals XAS, CR and CL in the ranges L_3, L_2 and $L_2, 3$ are used with $N/2$ scans for CR and CL for a total N scans for XAS. The white line was considered to have the same error as the XAS, that implies $\Delta r = \sqrt{2}\Delta XAS$.

Incorporing the error expresion for each integral used in the sum rules we obtain:

$$\Delta r = \sqrt{2} \frac{1}{\sqrt{N}} \frac{1}{\sqrt{P_{L_2,3}}} E_{L_2,3} \Delta X \tag{A.3}$$

$$\Delta q = \sqrt{2} \frac{1}{\sqrt{N/2}} \frac{1}{\sqrt{P_{L_2,3}}} E_{L_2,3} \Delta X \tag{A.4}$$

$$\Delta p = \sqrt{2} \frac{1}{\sqrt{N/2}} \frac{1}{\sqrt{P_{L_3}}} E_{L_3} \Delta X \tag{A.5}$$

$$\Delta m_{Orb} = m_{orb} \sqrt{\left(\frac{\Delta p}{p}\right)^2 + \left(\frac{\Delta r}{r}\right)^2} \tag{A.6}$$

$$\rightarrow \Delta m_{Orb}\% = 100 * \sqrt{\left(\frac{\Delta p}{p}\right)^2 + \left(\frac{\Delta r}{r}\right)^2} \tag{A.7}$$

$$\Delta m_{Seff} = m_{Seff} \sqrt{\left(\frac{\sqrt{3\Delta p^2 + 2\Delta q^2}}{3p - 2q}\right)^2 + \left(\frac{\Delta r}{r}\right)^2} \tag{A.8}$$

$$\rightarrow \Delta m_{Seff}\% = 100 * \sqrt{\left(\frac{\sqrt{3\Delta p^2 + 2\Delta q^2}}{3p - 2q}\right)^2 + \left(\frac{\Delta r}{r}\right)^2} \tag{A.9}$$

Each scan have around 900 points, cover up to 65 eV at most, correspond to 8 scans (4 CR and 4 CL) and the fluctuation per points in a non processed scan is around $\Delta X = 0.0006$ (figure). But to have a upper error value to apply over all results it was considered some approximation to over estimate the error: a higher $\Delta X = 0.002$ and highly sub estimated values $r, q, p = 0.002$. This result in an error of 2% for m_{Orb} and 3% for m_{Seff}, considering that each can not surpass the total magnetic moment for a bulk $3\mu_B$ then can be considered a global error of $0.1\mu_B$.

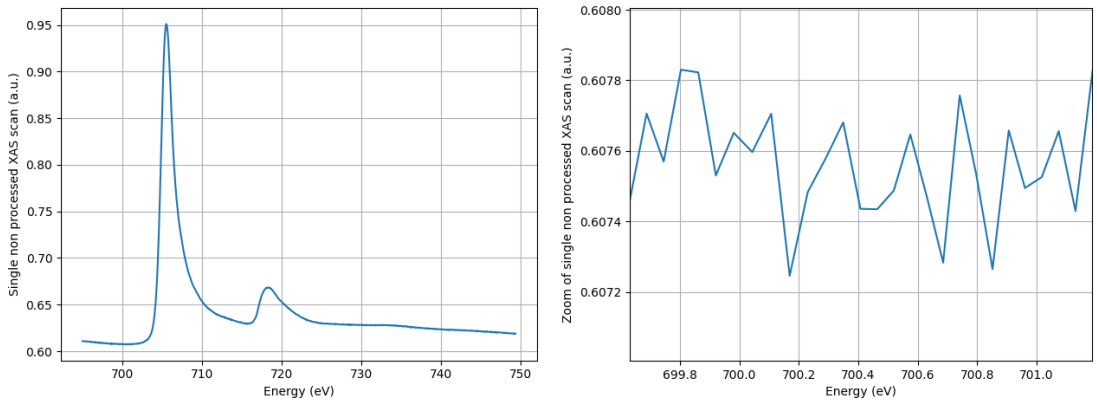

Figure A.1: Non processed scan of FeRh nanoparticle on carbon matrix.

A single non processed XAS scan (left) and a zoom over a flat region (right) indicating an error fluctuation of 0.0006 that correspond to around 0.2% of the total variation on the measurement.

For the case of oxide decomposition the reference also had the same error as the XAS signal since it correspond to the XAS of one sample obtaining a different Δr.

$$\Delta r = \sqrt{3}\frac{1}{\sqrt{N}}\frac{1}{\sqrt{P_{L_2,3}}}E_{L_2,3}\Delta X \tag{A.10}$$

(A.11)

The removal of the oxide component is not enough to change the 2% error for m_{Orb} and 3% error for m_{Seff}.

So globally can be considered an error of $0.1\mu_B$ for XMCD results. Notice that this is an overestimation of the error.

Notice that this correspond to the propagation of the experimental uncertainty. For the oxide removal is assumed that the XMCD signal correspond exclusively to the metallic component, assumption that may not be accomplished in all scans, as well the XAS shape of the reference may not be the same for the samples with oxide. Is not fully possible to determine the error associated with the oxide with the oxide removal, but we can try to get glimps of it:

The first is to observe that the XAS signal obtained for $Fe_{1\text{-}X}O_X$ is comparable to Fe oxides reported in other works. *Kleibert et al*

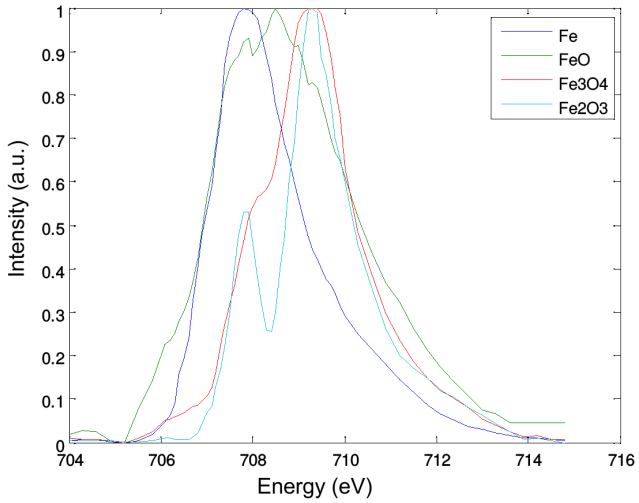

Figure A.2: Non processed scan of FeRh nanoparticle on carbon matrix.

XAS for metallic Fe and different kind of Fe oxided [100] (image taked from the supplementary material)

Appendix B

Magnetic characterization

B.0.1 Notations

In order to avoid ambiguity in mathematical expressions, in what follows is the notation for all the terms used in this work:

- $\overrightarrow{B}$: the magnetic induction.
- $\mu_0\overrightarrow{H}$: the applied magnetic field in the plane containing the sample, expresed in tesla (T).
- N_{tot}: total number of nanoparticles in the sample.
- $\overrightarrow{m}(T, \mu_0 H)$: the sample's magnetic moment expressed in Am^2 at the temperature T and in the applied magnetic field $\mu_0 H$.
- m_{sat} the magnetic moment at saturation.
- m_r the magnetic moment at remanence.
- $\overrightarrow{M}$: magnetization in Am, defined by $\overrightarrow{M} = \overrightarrow{m}/V$, where V is the sample volume.
- M_s: saturation magnetization.
- M_r: remanence magnetization.
- μ_0: the permeability in vacuum, that correspond to $\pi 4 \times 10^{-7}\,\mathrm{kgmA^{-2}s^{-2}}$.
- k_B: Boltzmann's constant, that correspond to $1.3807 \times 10^{-23}\,\mathrm{J\,K^{-1}}$.

- ΔE: the energy barrier to overcome so that a nanoparticle's magnetization switches. This energy quantity takes into account the particle's magnetic anisotropy (shape anistropy,volume and surface magneticristalline, magneto-elastic effects).

- χ: Sample's initial magnetic susceptibility, defined by $(\frac{dM}{dH})_{H\to 0}$. It is unitless by definition.

- D_{mag}: Is the median magnetic diameter, the size of the magnetic volume of the nanoparticles.

- $\rho(D)$ size probability distribution.

B.0.2 Energy sources

In this section, we will describe the magnetization state at 0 K of a supposedly spherical nanoparticle and discuss its mode of switching. In this case, the magnetization state in a particle is given through minimizing the magnetic energy:

$$E = E_{exchage} + E_{zeeman} + E_{Magnetostatic} + E_{Anisotropy} \tag{B.1}$$

Minimizing this energy determines the orientation direction of the magnetic moments of the system. It is difficult to satisfy the simultaneous minimization of the four energy terms. Thus, the most favorable state, where the system's energy is minimum, results from as compromise.

Exchange energy

$$E_{exchange} = \int_V A_E \left(\nabla \frac{M}{M_s}\right)^2 dV \tag{B.2}$$

The exchange interaction is the origin of the spontaneous orientation of the moments carried by the atoms. Following the sign of the coefficient of exchange interaction A_E , the material will be either ferromagnetic or antiferromagnetic. This interaction of an electrostatic origin was introduced by Heisenberg in 1929 in his quantum mechanics representation. This type of interaction is strong; however it only acts on close neighbours because it decreases rapidly with distance. Three different types of spontaneous orders can exist:

- The ferromagnetic, where the atomic moments are parallel to each other.

- The antiferromagnetic, where the moments are antiparallel with compensating moments.

- The ferrimagnetic, where the moments are antiparallel without compensating moments.

These orders exist under a certain temperature, called the Curie temperature (T_C) for the ferromagnetic order and the Néel temperature (T_N) for the antiferromagnetic and ferrimagnetic orders. Above this temperature, the magnetic order disappears and the material becomes paramagnetic, where the moments exist but are not coupled.

Zeeman energy

This energy appears when an external magnetic field $\mu_0 H$ is applied. It is basically the interaction between the applied magnetic field and the particle's magnetization.

$$E_{Zeeman} = \mu_0 \int_V \overrightarrow{M}\overrightarrow{H} dV \tag{B.3}$$

Magnetostatic energy

The magnetostatic energy, or demagnetizing energy, is the resulting energy from the interaction between the dipoles, on each atom. It is a much weaker energy compared to the exchange energy, but has a longer range. In general, the magnetostatic interaction energy is given by:

$$E_{Magnetostatic} = -\frac{1}{2}\mu_0 \int_V \overrightarrow{M}\overrightarrow{H_d} dV \tag{B.4}$$

The notion of magnetostatic energy can not be separated from the demagnetizing field. The demagnetizing field is the field created by the magnetization distribution inside the material itself. It is proportional to the opposite direction of magnetization and tends to close the magnetic flux. The demagnetizing field is related to the magnetization by $\overrightarrow{H_d} = -\mathcal{N}\overrightarrow{M}$, where $\mathcal{N}$ is the demagnetizing tensor, which is represented by a symmetric 3 x 3 matrix.

Anisotropy energy

The anisotropy energy can be defined by the natural orientation of the magnetization and consequently the orbital moment, and is generated by different contributions:

- The magnetocrystalline anisotropy energy comes from the interactions of the atomic orbitals with the electric field (crystalline field) created by the charge distribution in their environment. In order to characterize the magnetocrystalline anisotropy energy, the magnetization is expressed as a function of the principal lattice axis according to their symmetries. The energetically favorable direction of spontaneous magnetization is called the easy axis. For a cubic material, the expression is given by:

$$E_{anisotropy} = \int_V (K_1(cos^2\alpha_1 cor^2\alpha_2 + cos^2\alpha_2 cor^2\alpha_3 + cos^2\alpha_1 cor^2\alpha_3) + K2cos^2\alpha_1 cos^2\alpha_2 cos^2\alpha_3 + ...)dV \quad \text{(B.5)}$$

  where K_i are the anisotropy constants and α_i are the angles between the magnetization and a crystallographic axis. In the case of a tetragonal material where the axis c plays a particular role, the anisotropy energy is written in the spherical system:

$$E_{anisotropy} = \int_V (K_1 sin^2\theta + K_2 sin^4\theta cos(4\phi) + ...)dV \quad \text{(B.6)}$$

- The magnetocrystalline surface anisotropy energy that originates from the symmetry breaking at the surfaces and interfaces. The atomic magnetic interactions experience a discontinuity at the surface-interface. Thus, surface atom moments will have a tendency to align parallel or perpendicular to the surface plane where their crystallographic environment is changed compared to that of the core atoms. The surface magnetocrystalline anisotropy energy can be described by:

$$E_{anisotropy} = K_s cos^2\alpha \quad \text{(B.7)}$$

  where K s is the surface anisotropy constant and α is the angle between the atomic magnetic moment and the surface normal.

- The magneto-elastic energy that comes from a deformation of the crystal structure under mechanical stress. In our samples in carbon matrix, this anisotropy is neglected. The nanoparticles being preformed in a gas phase, their growth is unconstrained in carbon matrix. But it could be interesting to consider this term for cluster in epitaxy on monocrystalline surface.

In order to optimize the contributions of the different energies, in particular the magnetostatic and anisotropy energies, a magnetic material is divided into uniformly magnetized regions, called Weiss domains, separated by domain walls (Néel or Bloch walls). The magnetic moments are parallel inside these domains and tend to be antiparallel between each other in order to close the field lines (i.e. minimize the magnetostatic energy in the vacuum). Figure B.1 represents a demonstration of magnetic stray fields versus domain walls [113].

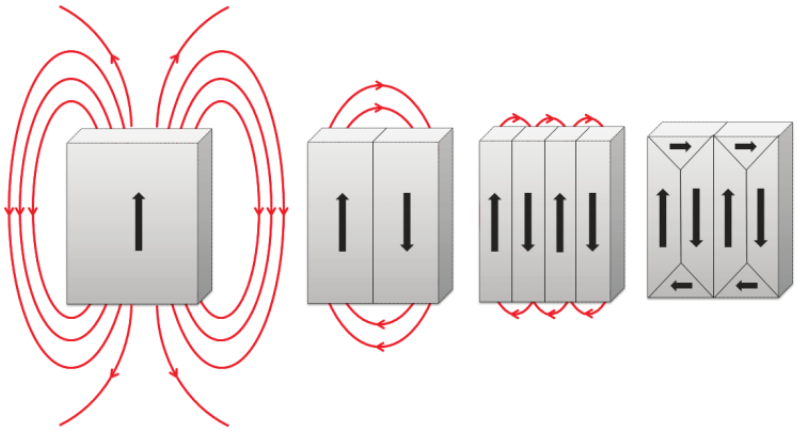

Figure B.1: Reduction of the magnetostatic energy.
From left configuration with less magnetic domains and more magnetostatic energy, and moving to the right configuration with more domains and magnetostatic energy are shown.

Stoner-Wohlfarth macrospin model

Magnetic materials are made up of multiple magnetic domains. These domains are separated by domain walls, as described earlier. However, the creation of magnetic walls cost energy, exchange energy in particular. The fundamental length scales which govern the magnetic properties are the domain wall width δ_m , the exchange length L_{ex} and the magnetostatic length L_s . These length scales are determined from the competition between the internal magnetic forces. The competition between the exchange energy and the magnetocrystalline anisotropy energy defines the domain wall width $\delta_m = \sqrt{A_{ex}/K}$. The competition between the exchange energy and the magnetostatic energy (demagnetizing field) defines the exchange length $L_{ex} = \sqrt{2A_{ex}/\mu_0 M_s^2}$ and the magnetostatic length is $L_s = \sqrt{A_{ex}/2\pi M_s^2}$, where K is the magnetic anisotropy constant and A_{ex} is the exchange length constant within a grain.

For spherical particles, we define the critical radius R_c [114] which is determined by the balance of domain wall energy and magnetostatic energy as:

$$R_c = 36\frac{L_{ex}^2}{\delta_m} = \frac{36\sqrt{A_{ex}K_{eff}}}{\mu_0 M_s^2} \tag{B.8}$$

Where K_{eff} is the effective anisotropy. R_c determines the radius limit below which a particle is single domain. In addition, we define the coherent radius $R_{coh} = 5L_{ex}$. The coherent radius presents the limit below which the magnetic reversal of the particle is coherent, which implies the all the magnetic moments carried by the atoms inside the particle rotate at the same time. This means that all the atomic moments in a particle are represented by one magnetic moment, known as the macrospin. The macrospin is thus defined as $m_{NP} = m_{at}N_{at}$ where m_{at} is the moment of an atom and N_{at} is the number of atoms in a particle. The coherent reversal of a mono-domain magnetic moment is described by the Stoner-Wohlfarth model [87, 115].

The macrospin model (or Stoner-Wohlfarth SW model) is widely used to simulate and model the magnetization reversal of ferromagnetic nanoparticles. It is a simple model based on several hypothesis. The nanoparticles are described geometrically as elongated ellipsoids, where the major axis and the easy axis coincide (Figure B.2). The anisotropy is considered uniaxial with a volume, shape and/or magnetocrystalline nature. The anisotropy introduces an energy barrier (ΔE) that must be overcome for the reversal of the magnetic moment to occur. The energy barrier is given by $\Delta E = K_{eff}V$, where K_{eff} is the effective anisotropy constant supposed independent of the volume V. In addition, the SW model supposes a temperature of 0 K, the so-called absolute zero.

When a magnetic field ($\mu_0 H$) is applied, the two energy terms in play are the anisotropy and Zeeman energy. The sum of these two terms constitute the magnetic energy (E) of the nanoparticle. Considering the left diagram of B.2, we get:

$$E = \Delta E sin^2\theta - \mu_0 H M_S V cos(\phi - \theta) \tag{B.9}$$

The reversal field, where the energy barrier disappears in the particular case of $\phi = \pi$ or $\phi = \pi/2$, is obtained for:

$$H = H_a = \frac{2K_{eff}}{\mu_0 M_S} \tag{B.10}$$

where H_a is called the anisotropy field of the particle.

Figure B.3 represents the evolution of the component of the normalized magnetization (in the direction along the field) ($M_H = \overrightarrow{M} \cdot \overrightarrow{H} / \parallel \overrightarrow{M} \parallel \parallel \overrightarrow{H}$) as a function

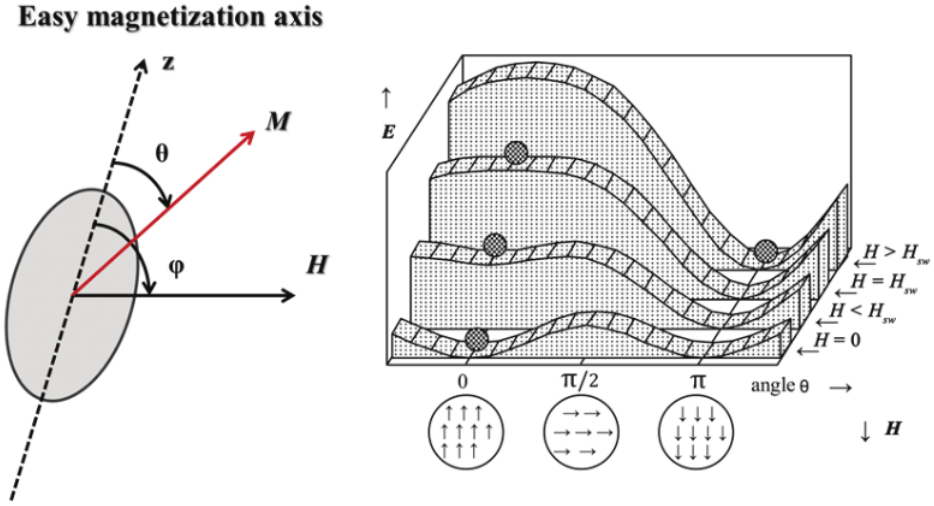

Figure B.2: Schematic of a macrospin potential.
Schematic representation of a macrospin in a external magnetic field (Left) and the superparamagnetic potential well at different magnetic fields (Right).

of the applied magnetic field.

The equation B.9 allows determining numerically the hysteresis loop described by the magnetization component in the direction of the applied field for a single particle. In order to calculate for a given magnetic field the stable values of magnetization, it is necessary to minimize the total energy and to determine its critical values.

In figure B.4, the hysteresis loops for a single particle are presented as a function of the applied field H and the angle ϕ (from 0° to 90°). The value of H that verify:

$$\left(\frac{\delta E}{\delta \theta}\right)_{\theta=\theta_0} = 0 \; and \; \left(\frac{\delta^2 E}{\delta \theta^2}\right)_{\theta=\theta_0} > 0 \tag{B.11}$$

is known as the switching field. The switching field H_{sw} corresponds to the magnetization reversal by applying an external magnetic field H having an angle ϕ with the easy axis of magnetization:

$$H_{sw}(\phi) = H_a \left(sin^{\frac{2}{3}}(\phi) + cos^{\frac{2}{3}}(\phi)\right)^{-\frac{3}{2}} \tag{B.12}$$

From equation B.12 it can be noted that the switching field does not depend on the particle's volume. The anisotropy and switching fields are identical for all particle sizes. The obtained curve represents, in polar coordinates, the Stoner-Wohlfarth astroid (Figure 2.28) [87]. This curve represents the switching (reversal)

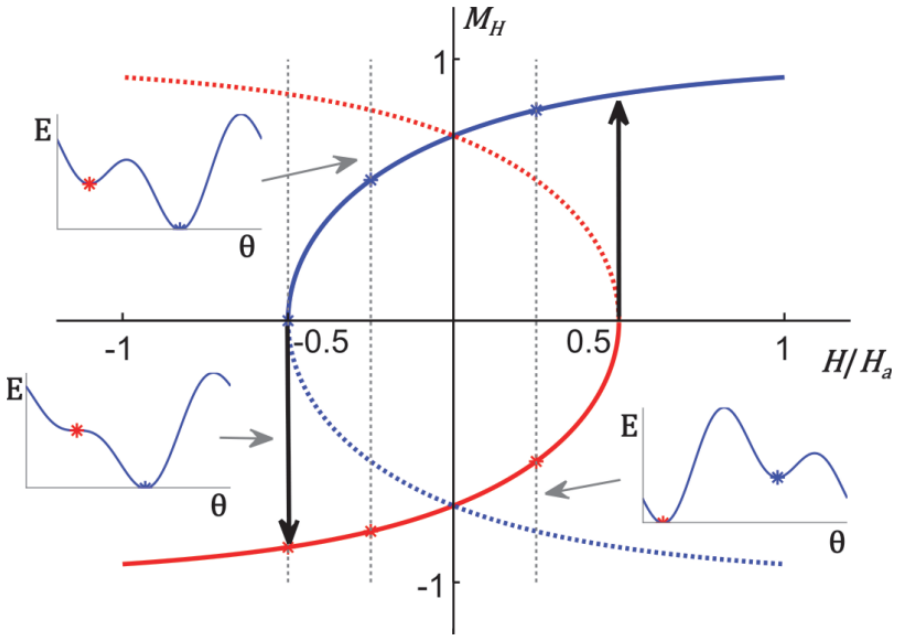

Figure B.3: Stoner-Wolhfarth representation of energy for different fields.
An example of the solution for the Stoner-Wolhfarth model for two positions of easy magnetization. The continuous line represents the positions of energy minimum; the dashed line, the local energy minima. The energy profiles for three different applied magnetic field are represented.

field of the particle's magnetization in the space of the applied magnetic field. The two axes, characteristic of an astroid, correspond to the easy and hard axis of magnetization. For all fields inside the astroid, the magnetization has two possible orientations (stable or meta-stable), whereas outside the astroid there is only one orientation (figure B.5).

Superparamagnetism

For single domain nanoparticles, another new magnetic regime is observed which is the superparamagnetism. If we suppose that the nanoparticles have a uniaxial magnetic anisotropy without an applied field, the energy barrier ΔE, presented in figure B.2, can be overcome by thermal energy ($k_B T$). The magnetic reversal being thermally activated, the relaxation time τ and the reversal frequency ν between the two directions of easy magnetization can be expressed by an Arrhenius law:

$$\tau = \tau_0 e^{\frac{\Delta E}{k_B T}} \tag{B.13}$$

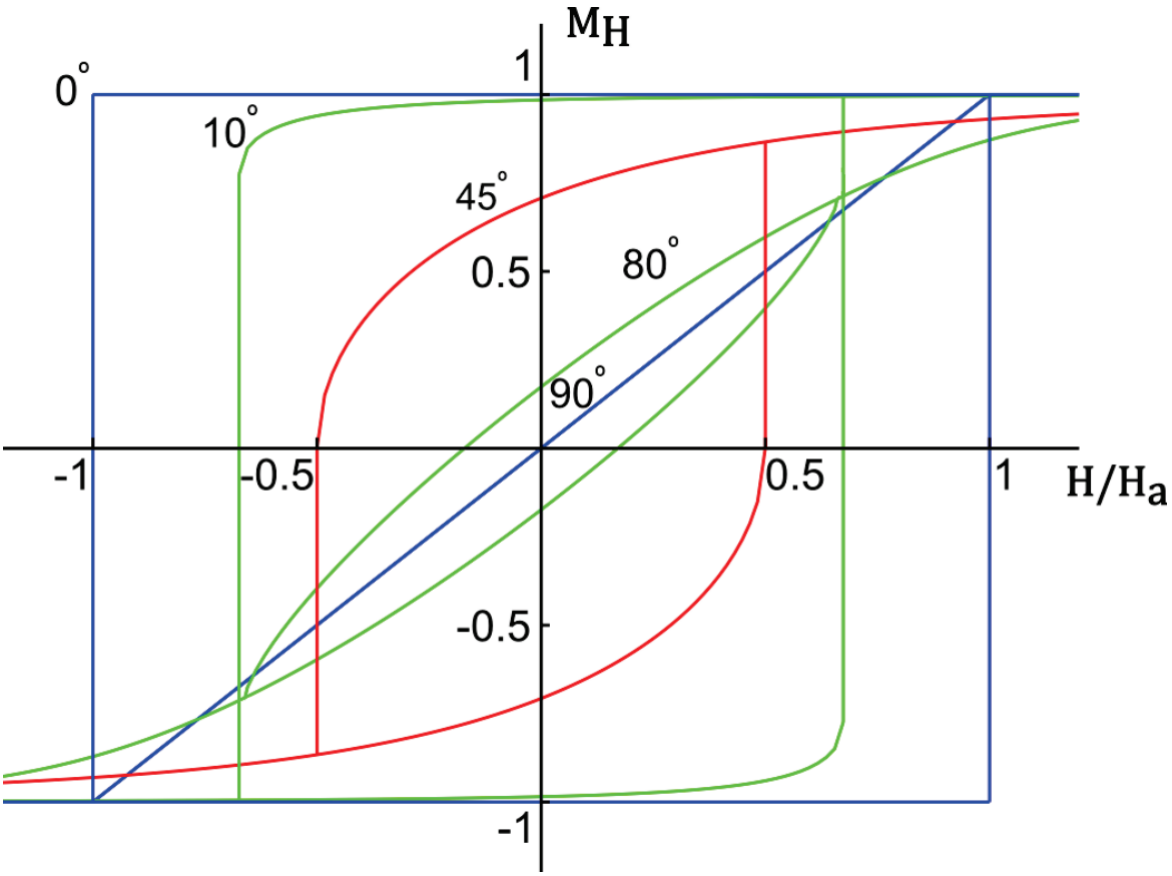

Figure B.4: Hysteresis loops according to Stoner-Wolhfarth model.

Magnetization curves for the Stoner-Wohlfarth model for various angles ϕ between the applied field direction and the easy axis.

where τ_0 is the relaxation time in the absence of a barrier. τ_0 can be determined from different models [116–119]. Nevertheless, its variation with temperature is overlooked experimentally against the exponential term. Its value is typically in the orders of 10^{-9} s to 10^{-11} s. So, if we take into account the experimental measuring time of the magnetization, denoted τ_{mes}, we can put into evidence that for a particle there exist two regimes:

- For $\tau_{mes} >> \tau$, the average magnetization of the measured particle will be zero since the particle's magnetization will be constantly reversing from one direction of the easy axis to the other during the measurement. This is referred to as superparamagnetism; it corresponds to an appearance of paramagnetism even though all the atomic moments in the particle are coupled ferromagnetically.

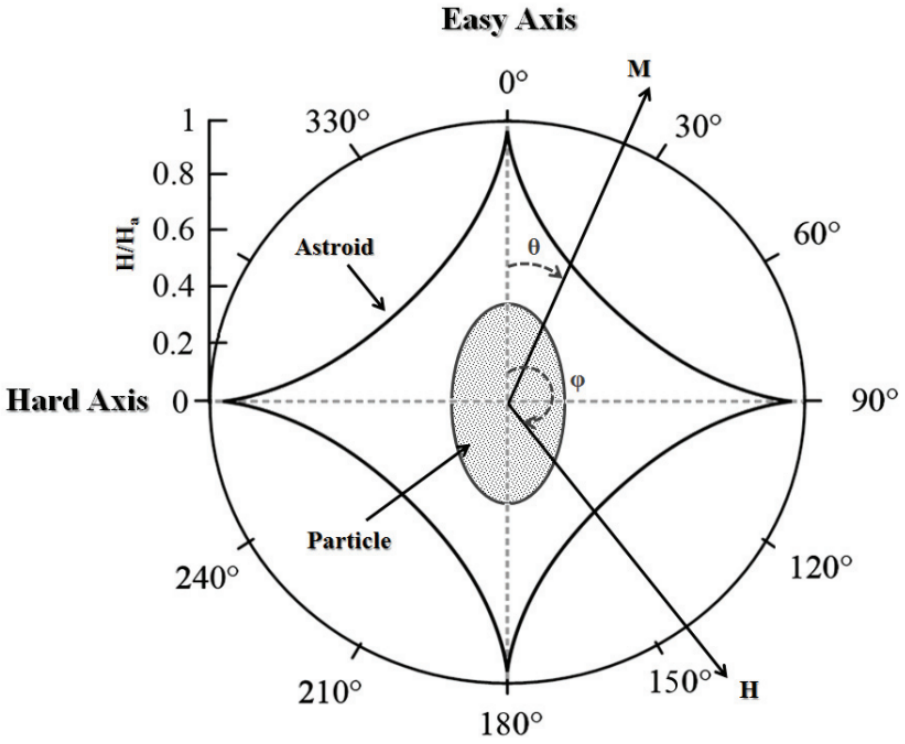

Figure B.5: Diagram of the Stoner-Wohlfarth astroid in two dimensions.

- For $\tau_{mes} << \tau$, the measured magnetization is different than zero, the particles is labeled as "blocked".

Thus, the progressive transition between the two regimes (blocked and superparamagnetic) is achieved for $\tau \approx \tau_{mes}$. The expression of τ reveals that it is strongly dependent on T such that for a given particle size, the transition temperature between the two states, referred to as the blocking temperature T_B, for which $\tau(T_B) = \tau_{mes}$ is:

$$T_B = \frac{\Delta E}{k_B ln\left(\frac{\tau_{mes}}{\tau_0}\right)} = \frac{K_{eff} V}{k_B ln\left(\frac{\tau_{mes}}{\tau_0}\right)} \tag{B.14}$$

Nanoparticle assembly

The studied samples are made up of diluted size-selected and non size-selected (neutral) FeRh nanoparticle samples embedded in either an amorphous carbon

matrix, or a copper matrix. To interpret the different magnetic curves, several hypothesis were assumed:

- the magnetic moments of a particle is a macrospin, described by the Stoner-Wohlfarth model
- The anisotropy of the nanoparticles is uniaxial with random orientation of the easy magnetization axes from one particle to another.
- M_S and ΔE are temperature independent.

The measurements that will be presented were done on assemblies of nanoparticles embedded in a matrix (Chapter 4). In both cases, it is possible to question whether or not there are magnetic interactions between the particles. Three types of magnetic interactions could intervene between the particles present in the matrix:

- Dipolar interactions, independent from the nature of the matrix, are long range interactions since they decay as a $1/d^3$, where d is the distance between the particles
- Ruderman-Kittel-Kasuya-Yosida (RKKY) interactions exist only in metallic matrices. They originate from a parallel or anti-parallel coupling between ferromagnetic layers [120]. This type of interaction is short range as it disappears after 5 nm [121].
- Superexchange interactions are present in isolating matrices (oxydes) [122]. These influences are very short range, a few interatomic distances.

Field-cooling zero-field-cooling

The acquisition of the susceptibility curves following the ZFC-FC protocol is a typical tool used to determine the magnetic properties of cluster assemblies. These measurements are commonly used since they provide valuable information concerning the magnetic anisotropy energy (MAE) of the nanoparticles. The MAE is a key information related to the energy barrier that governs the magnetization reversal from one direction of easy magnetization to the other. It controls the magnetic stability of the nano-magnets which is an important parameter from an applications' point of view, mainly in the domain of magnetic data storage.

m(T) measurements following the ZFC-FC protocols were realized in order to determine the magnetic anisotropy of the clusters. First, the sample is cooled down

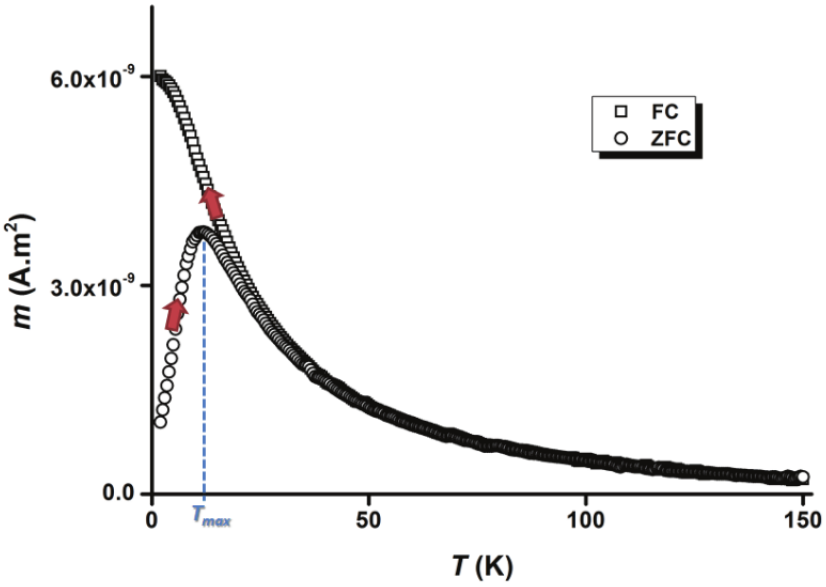

Figure B.6: Example of FC/ZFC for a magnetic nanocluster.

to a low temperature (2 K) without field. The particles are thus in a blocked state with their magnetization randomly distributed homogeneously in all directions of space. Since no external magnetic field was applied, the average magnetization of the sample is zero. A small field $\mu_0 H$ is then applied to remain in the linear response regime where the magnetic susceptibility depends linearly on the applied field. The magnetic moments of the sample is then measured as a function of temperature (Figure B.6). Thermal energy will allow overcoming the MAE barrier. An increasing number of particles will pass from the blocked state to the superparamagnetic state with a response following $1/T$; this gives the ZFC susceptibility curve shown in figure B.6.

The FC susceptibility curve is obtained by decreasing the temperature while keeping the previously applied field H. At high temperatures, the particles are superparamagnetic, the ZFC and FC curves superpose on a $1/T$ evolving curve. Once the temperature is low enough, the particles go back to the blocked state.

Inverse remanent magnetization and direct current demagnetization (IRM-DCD)

The Isothermal Remanent Magnetization (IRM) curve corresponds to a series of measurements of the remanent magnetization of an initially demagnetized sample. The measurement is done at remanence, an external magnetic field $\mu_0 H$ is applied

then nullified ($\mu_0 H = 0$) at a fixed temperature after which the sample magnetization is measured. The complete curve is obtained by repeating the process of applying a field, nullifying and measuring while increasing H progressively (see figure B.7). The acquisition process is longer than that of a typical hysteresis loop since the applied field H must be returned to zero field before doing each measurement. On the contrary, returning the field to zero allows for the measurement of only the irreversible magnetization variations of a sample. In addition, this type of measurement allows to eliminate all diamagnetic (from the substrate, for example), paramagnetic (eventual impurities) contributions as well as contributions from particles in the superparamagnetic state.

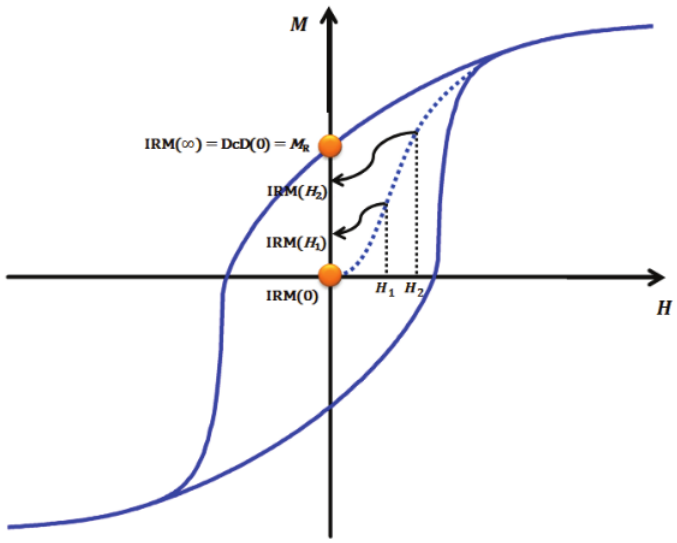

Figure B.7: Example of IRM for a magnetic nanocluster.

The evolution of an IRM at zero temperature comes uniquely from an irreversible change within the sample. In the case of an assembly of macrospins with uniaxial anisotropy, the magnetization reversal of some particles is measured. In the initial state $IRM(H = 0)$, the particles magnetic moments are randomly oriented, such that, statistically, the moment provided by each particle is compensated by another one. When a field is applied this symmetry is broken and one direction becomes more favourable than the others (in the half-sphere defined by the direction of the applied field H). Thus, half the particles are found in the initially stable potential well, while the other half is in the initially metastable well. The increase of the applied field H corresponds to a decrease in the energy barrier that needs to be crossed to pass from the metastable to the stable potential well. Thus, implying an increasing dissymmetry in the proportion of particles magnetized in the field direction with respect to the opposite direction. Finally,

at $T = 0K$ and in the uniaxial case, the energy barrier vanishes for $H > H_a$. All the moments that pointed initially in the direction opposite of the field H have necessarily flipped. At a larger field, the IRM is identical to the hysteresis loop at $H = 0$ after saturation of the sample. This implies that $IRM(H = \inf) = m_r$.

The complementary measurement of the IRM is the Direct current Demagnetization (DCD). It corresponds to a progressive demagnetization of a sample that was initially brought to remanence after saturation in one direction. The measurement is carried out by applying an increasing field in the opposite direction, and measuring the sample's magnetization after nullifying the field ($\mu_0 H = 0$). Similar to the IRM protocol, this measurement is sensitive to the irreversible magnetization variations in the sample. Thus, it has the same physical process as the IRM curve, the difference comes uniquely from the initial state. Here, the sample is initially saturated by applying a field in the opposite direction to the one used for the acquisition of the DCD curve. The moments of all the particles are initially pointing in the same half-sphere ($DCD(H = 0) = m_r$). For a sufficiently large applied field (at $T = 0K$ and for $H > H_a$), all the magnetic moments will be switched (thus ($DCD(H = \inf) = -m_r$). In this case, the reversal concerns all the particles, whereas in the case of the IRM it concerns only half. If in the case of the IRM N particles have switched with a field H, 2N particles will switch in the case of the DCD(H) measurement. Since the starting point of the IRM is a demagnetized state, while it is the remanent state for the DCD, the following fundamental equality can be deduced:

$$DCD = mr - 2IRM \tag{B.15}$$

It should be noted that this equality is valid regardless of the temperature, the particle's size distribution, the anisotropy distribution, the nature of the anisotropy of the particles, and even if the magnetization reversal is achieved in an incoherent manner. On the other hand, the only hypothesis necessary for the validity of this equality is the absence of interactions between the magnetic particles. The reversal of each particle must depend only on the applied field and not on the state of the other particles. If this hypothesis, which is in practice very binding, is not verified, the magnetization reversal of the magnetic moments will depend on the environment and thus on the initial state of magnetization of the sample. A dissymmetry is thus observed between the magnetization reversal of the DcD and IRM curves and the equation B.15 is no longer valid. Thus, the invalidity of this equality reveals the presence of magnetic interactions in the sample. This criterion is widely used to characterize the interactions in an assembly of nanoparticles, nanofilaments or thin films [123–128]. The magnitude Δm is considered in this case and is defined as:

$$\Delta m = DCD(H) - (m_r - 2IRM(H)) \tag{B.16}$$

This magnitude corresponds to the difference between the number of moments that switch in the IRM measurement and those that switch in the DCD measurement as a function of field. Thus, a negative value for Δm signifies that the magnetic moment is most easily switched when the initial state is the remanent state (the magnetic moment of all the particles point in the same half-sphere). Considering only one direction, this means that for the moment for a given particle, the switching from +z to -z direction is easier when the other particles have a global magnetic moment directed towards +z. This translates to demagnetizing interactions (as the case of dipolar interactions). On the contrary, a positive Δm means that it is harder to switch the magnetic moments when its neighbours have a global orientation in the same direction. This translates to magnetizing interactions (as the case of exchange interactions of the ferromagnetic type). Another way to present the Δm is the Henkel graph [129]. Figure B.8 shows the theoretical IRM, DCD and Δm curves for an assembly of randomly oriented uniaxial macrospins and without interactions ($\Delta m = 0$). We will therefore use:

- $\Delta m < 0$, demagnetizing interaction.
- $\Delta m > 0$, magnetizing interaction.
- $\Delta m = 0$, no interaction.

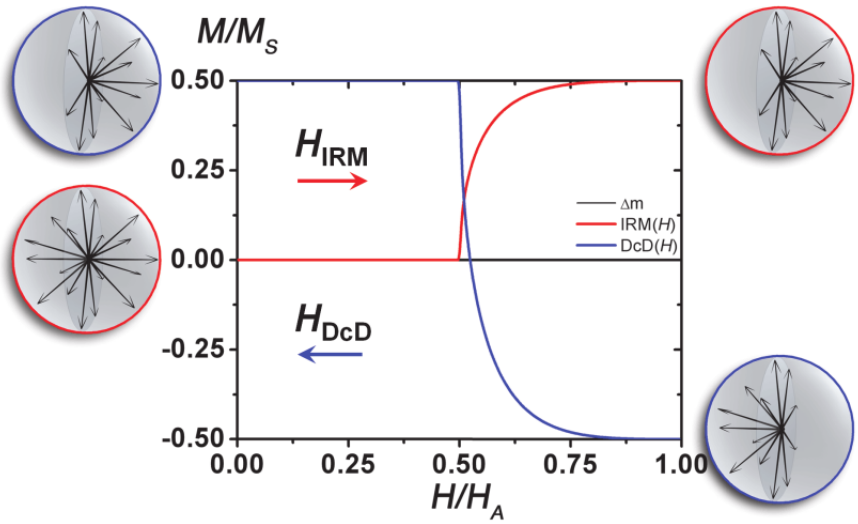

Figure B.8: IRM/DCD for a macrospin.
IRM, DcD and Δm curves calculated at T=0 K for an assembly of randomly oriented uniaxial macrospins.

Appendix C

TEM images

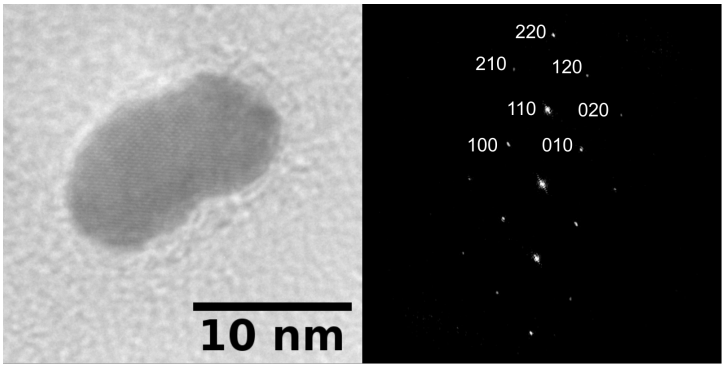

Figure C.1: B2 FeRh nanoparticle, view of plane [001]

Figure C.1 is to show a highly defined B2 crystal. It posses 3 Å of lattice parameter and is projected over the plane [001]

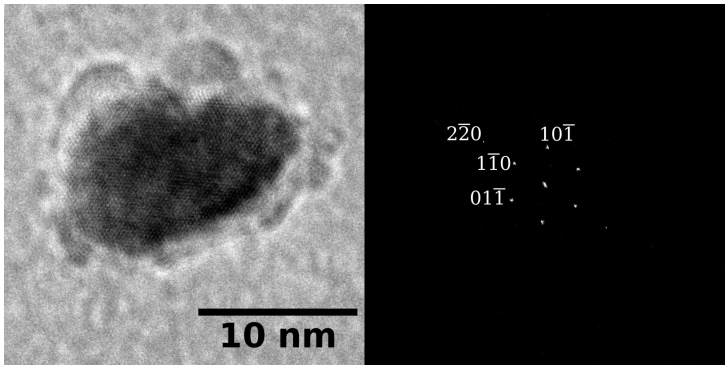

Figure C.2: B2 FeRh nanoparticle, view of plane [111]

Figure C.2 is a FeRh B2 crystal. It posses 3 Å of lattice parameter and is projected over the plane [111] giving a hexagonal pattern. The 'cloud' observed around the nanoparticle normally appears when the electron beam is applied long time over the same area. It could correspond to grafitization of the carbon capping as well it may be CO_X contamination attached with the electron beam exposure.

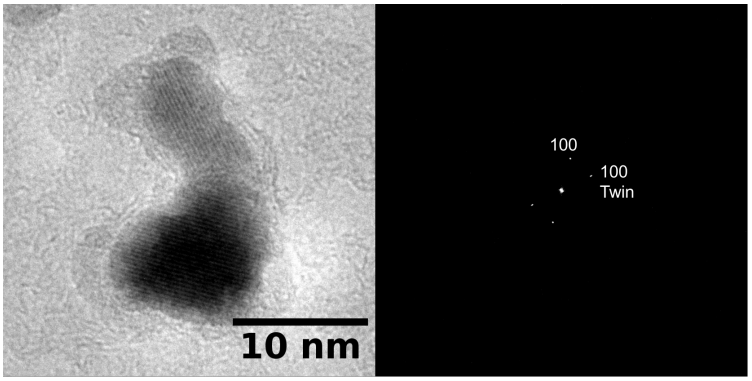

Figure C.3: B2 FeRh nanoparticle, view of plane [001] with twin at the plane [310] that correspond to 50°

Figure C.3 is a FeRh B2 crystal. It posses two crystalline regions with 3 Å of lattice parameter and both projected in the plane [001]. It corresponds to a twin in the plane [310] which gives a 50° of inclination.

Appendix D

Additional XAS/XMCD scans

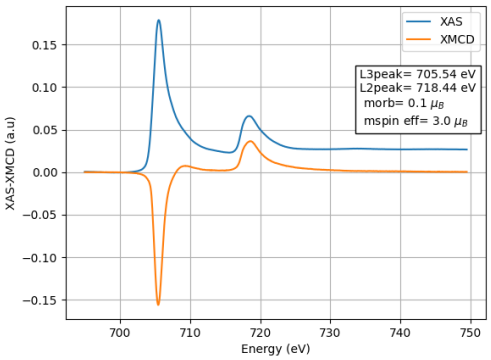

2 K.

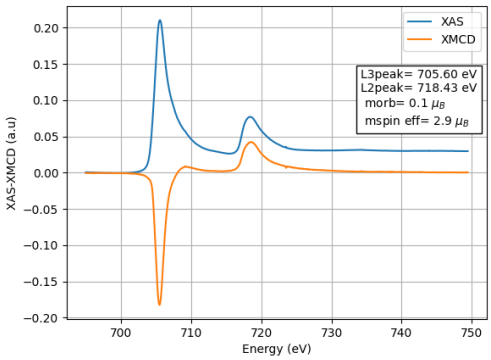

50 K

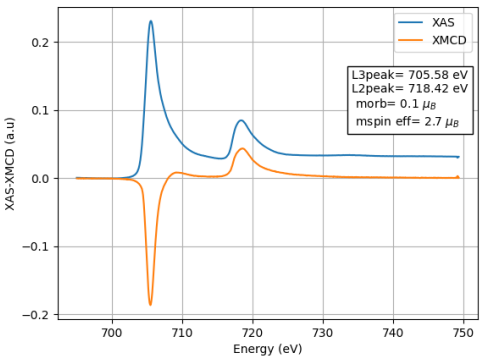

250 K

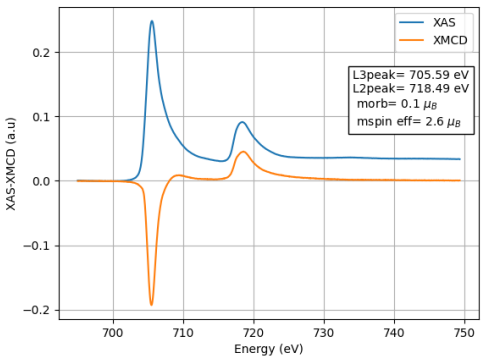

300 K

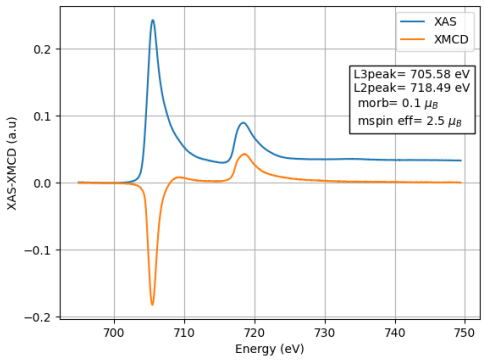

350 K

Figure D.1: XMCD for FeRh embedded in carbon matrix in normal incidence configuration.

XMCD for FeRh nanoparticles of 7 nm for temperatures from 4 K to 300 K for normal incidence X-rays.

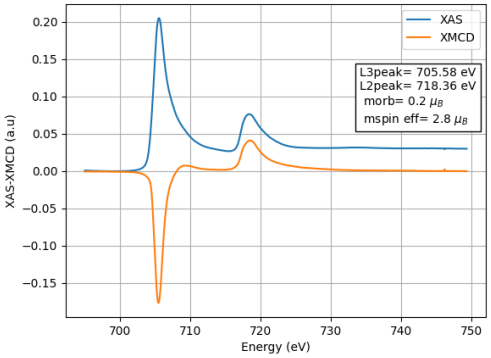

2 K.

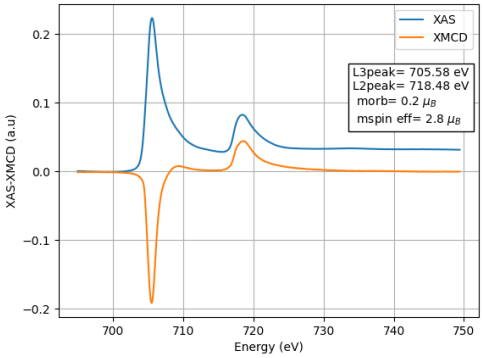

50 K

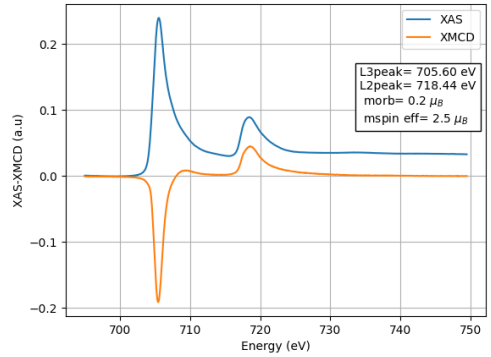

250 K

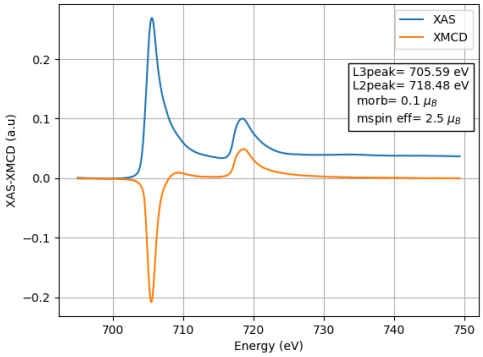

300 K

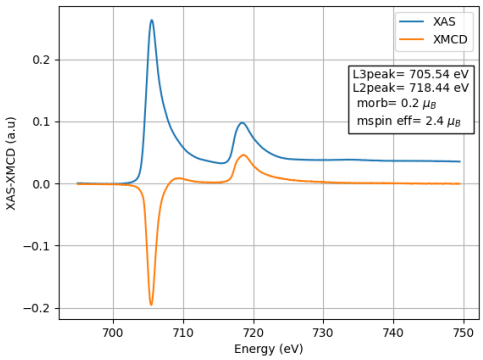

350 K

Figure D.2: XMCD for FeRh embeded in carbon matrix in grazing incidence configuration.

XMCD for FeRh nanoparticles of 7 nm for temperatures from 4 K to 300 K for grazing incidence X-rays.

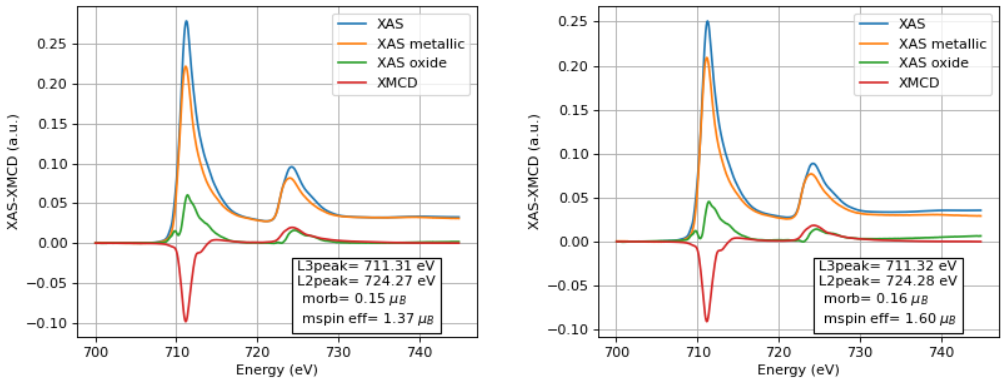

350K cooling

300K cooling

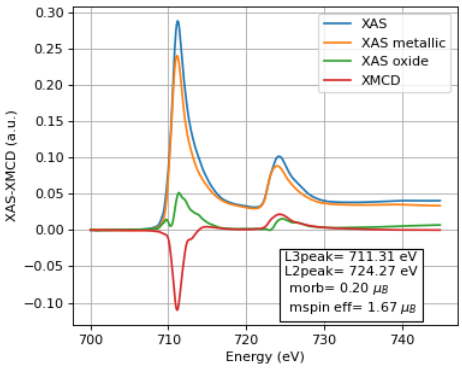

250K cooling

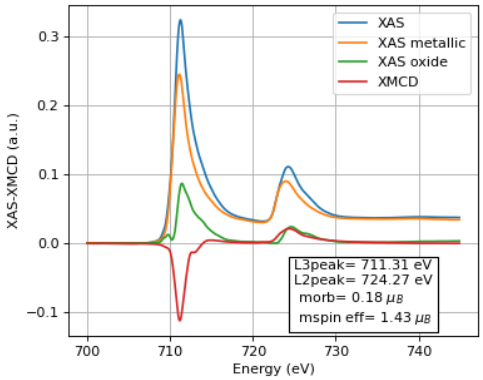

200K cooling

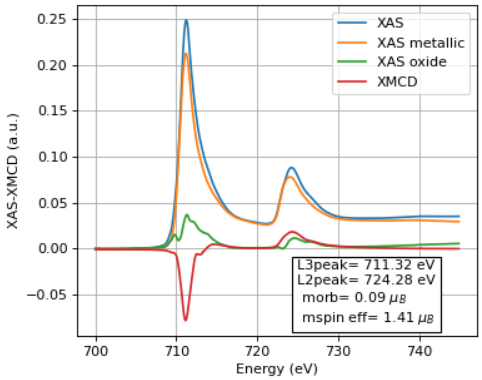

100K cooling

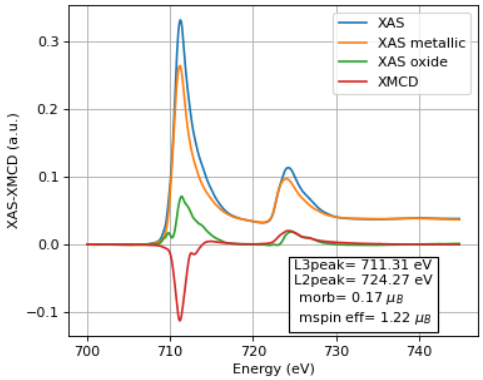

4K cooling

Figure D.3: XMCD for FeRh thick sample in the cooling down branch.

XMCD at 350K, 300K, 250K, 200K, 100K and 4K in the cooling branch down for the 150nm thick FeRh nanocluster assembled film after being reduced in situ UHV

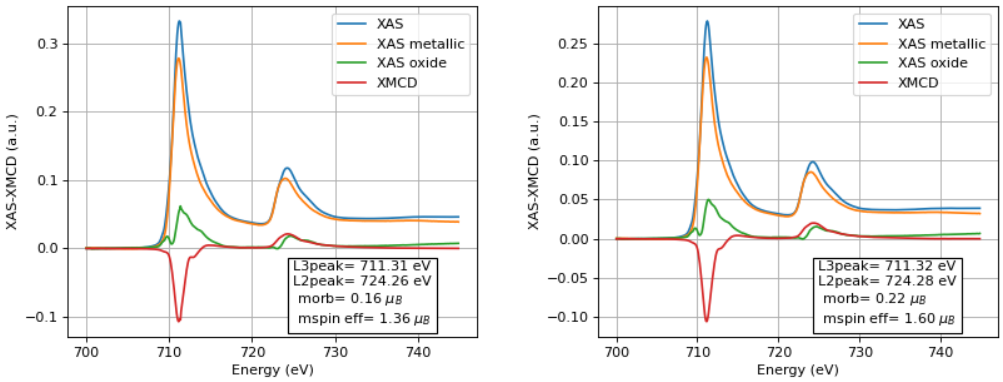

350K heating

300K heating

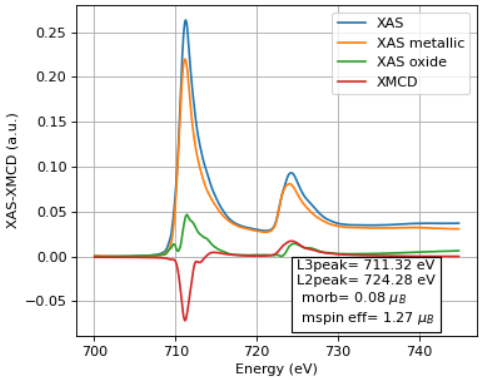

250K heating

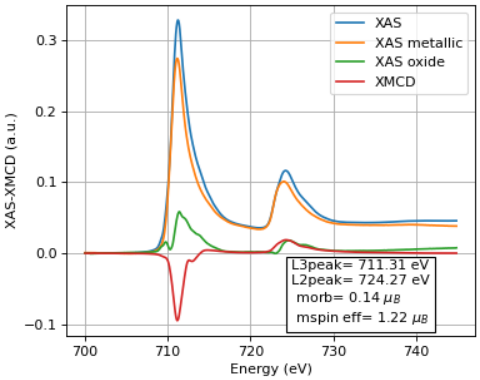

200K heating

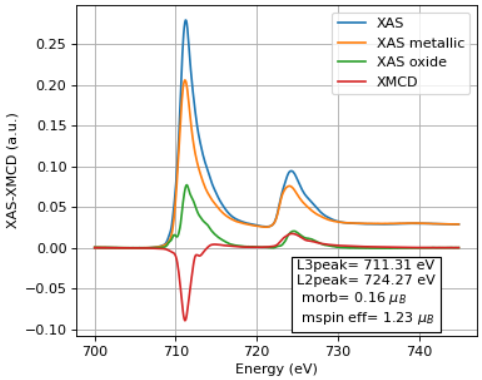

100K heating

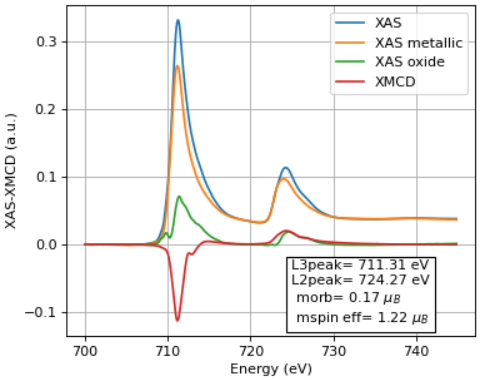

4K heating

Figure D.4: XMCD for FeRh thick sample in the heating up branch.

XMCD at 350K, 300K, 250K, 200K, 100K and 4K in the heating up branch for the 150nm thick FeRh nanocluster assembled film after being reduced in situ UHV

Appendix E

XANES references

Here are exposed some evidences that correlate the presence of the B2 phase in FeRh with specific XANES shape at the K Fe and L Rh edge.

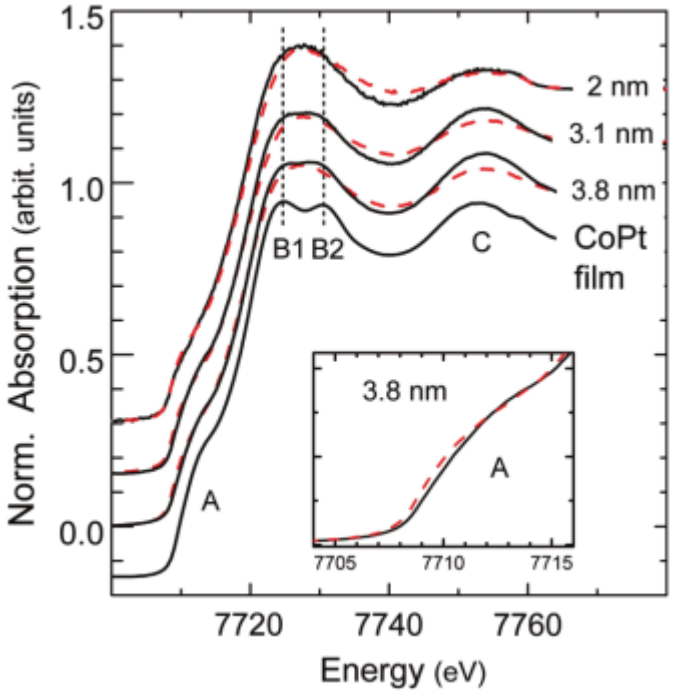

Figure E.1: XANES on CoPt

XANES spectra for CoPt nanoparticles of 2.0nm, 3.1nm, 3.8nm size and film before annealing (dashed red) and after annealing (in black) with the Co K edge splitting into B1 and B2 peaks corresponding to $L1_0$ phase transformation.

Blanc et al [93] showed the transition from $A1$-like phase to $L1_0$-like phase for CoPt clusters, from XANES at Co K edge. In Figure E.1, is possible to see that the as-prepared A1 phase posses single peak while chemically ordered CoPt film posses B1 and B2 peaks associated to the $L1_0$ phase.

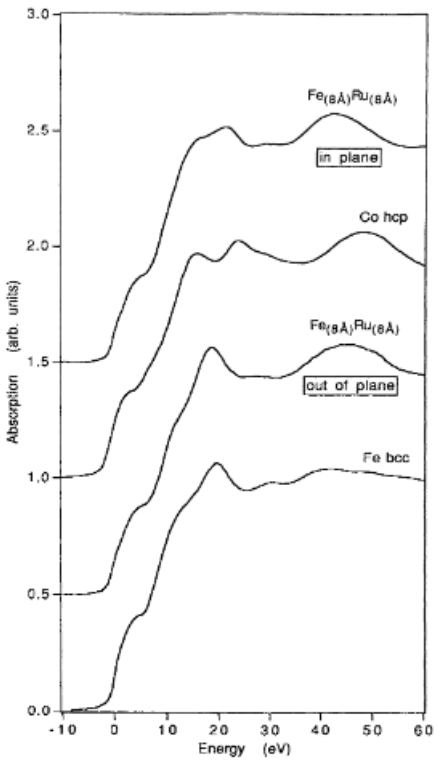

Figure E.2: XANES on FeRu and Fe

XANES spectra for Fe/Ru superlattices with in plane and out of plane X-ray polarization at Fe K edge

Baudelet et al [94] explore Fe/Ru superlattices of alternated thin films from XANES at Fe K edge, showing that Fe bcc posses a characteristic peak observed outside plane X-ray polarization. They reveal an anisotropy in the XANES that is an indicator of having hcp-like lattice in plane.

Aubert et al [96] expose on their work that bulk FeRh B2 phase shows a XANES peak after the Rh L edges (figure E.3) which is not present for fcc Rh alone or for FeRh in A1 phase. *Smekhova et al* [95] present XANES for Fe@Rh and Rh@Fe shell where is possible to notice there is no shoulder at Rh L edges (figure E.4). The last one is a reference that can be used for a full segregated alloy scenario.

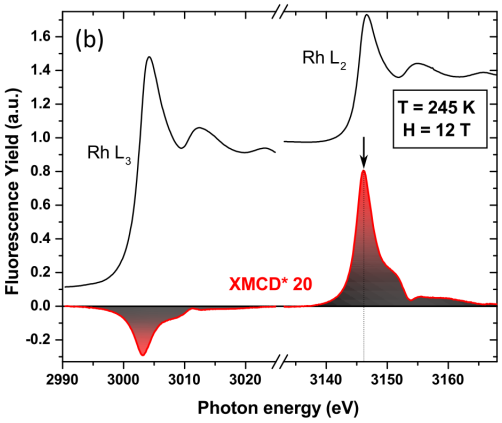

Figure E.3: XANES on FeRh B2 bulk

XANES spectra for FeRh B2 phase at Rh L edge

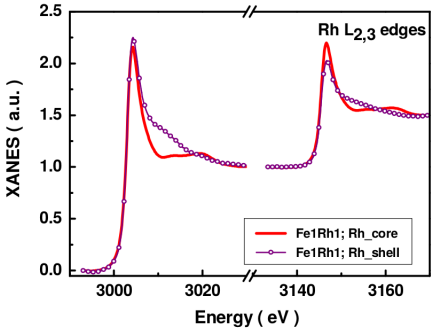

Figure E.4: XANES on Fe@Rh and Rh@Fe nanoparticles

XANES at the Rh L edge for nanoparticles with core shell Fe-Rh structures at 10 K and 6T.

Appendix F

2D crystal projection to 3D

The path got from the five-gaussian fit (fig 5.14 and table 5.2) correspond to a 2D crystal with four variables (2 distances and 2 angles). A 3D crystal correspond to nine variables (3 distances and 6 angles), so that correspond to five free variables and is necessary to impose a total of four conditions to do the 3D projection of a 2D crystal. Here as an example we will do a projection of the 2D crystal found, but is important to keep in mind that there is a total of four conditions imposed which is which is a strong assumption. For this reason this is treated as an exercise and does not have to be treated as a result.

The conditions imposed are that the crystal is an octahedron with $a = b \neq c$ (first condition imposed) and 90° in its three angles (the other three conditions). For a certain plane hkl that fit N_{hkl} times in the crystal cell the inter-planar distance is:

$$D_{inter-planar} = \frac{N_{hkl}}{\sqrt{\frac{h^2}{a^2} + \frac{k^2}{b^2} + \frac{l^2}{c^2}}} \tag{F.1}$$

Using the plane [112] for the vertical direction with 2.7 Å and [211] for the direction with 2.4 Å and the previous condition mentioned $a = b \neq c$ then is obtained:

$$2.7\text{Å} = D_{inter-planar1} = \frac{2}{\sqrt{\frac{2^2}{a^2} + \frac{4^2}{c^2}}}$$
$$2.4\text{Å} = D_{inter-planar2} = \frac{2}{\sqrt{\frac{5^2}{a^2} + \frac{1^2}{c^2}}}$$
$$\rightarrow a = 2.84\text{Å}$$
$$\rightarrow c = 3.65\text{Å}$$

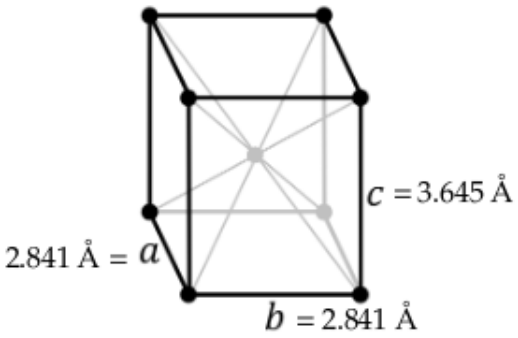

Figure F.1: Lattice parameter found for the nanoparticle in epitaxy using the imposed conditions.

Bibliography

[1] V. L. Moruzzi and P. M. Marcus. Antiferromagnetic-ferromagnetic transition in ferh. *Phys. Rev. B*, 46:2864–2873, Aug 1992.

[2] M. R. Ibarra and P. A. Algarabel. Giant volume magnetostriction in the ferh alloy. *Phys. Rev. B*, 50:4196–4199, Aug 1994.

[3] E Mancini, F Pressacco, M Haertinger, E E Fullerton, T Suzuki, G Woltersdorf, and C H Back. Magnetic phase transition in iron–rhodium thin films probed by ferromagnetic resonance. *Journal of Physics D: Applied Physics*, 46(24):245302, jun 2013.

[4] Michael J. Mehl. A brief history of strukturbericht symbols and other crystallographic classification schemes. *Journal of Physics: Conference Series*, 1290(1):012016, oct 2019.

[5] Fallot, M. Les alliages du fer avec les métaux de la famille du platine. *Ann. Phys.*, 11(10):291–332, 1938.

[6] E. F. Bertaut, A. Delapalme, F. Forrat, G. Roult, F. De Bergevin, and R. Pauthenet. Magnetic structure work at the nuclear center of grenoble. *Journal of Applied Physics*, 33(3):1123–1124, 1962.

[7] G. Shirane, C. W. Chen, P. A. Flinn, and R. Nathans. Mössbauer study of hyperfine fields and isomer shifts in the fe-rh alloys. *Phys. Rev.*, 131:183–190, Jul 1963.

[8] L H Lewis, C H Marrows, and S Langridge. Coupled magnetic, structural, and electronic phase transitions in ferh. *Journal of Physics D: Applied Physics*, 49(32):323002, jul 2016.

[9] L. J. Swartzendruber. The ferh (iron-rhodium) system. *Bulletin of Alloy Phase Diagrams*, 5(5):456–462, Oct 1984.

[10] M. Fallot and R. Horcart. *Rev. Sci.*, 77:498, 1939.

[11] R. O. Cherifi, V. Ivanovskaya, L. C. Phillips, A. Zobelli, I. C. Infante, E. Jacquet, V. Garcia, S. Fusil, P. R. Briddon, N. Guiblin, A. Mougin, A. A. Ünal, F. Kronast, S. Valencia, B. Dkhil, A. Barthélémy, and M. Bibes. Electric-field control of magnetic order above room temperature. *Nature Materials*, 13(4):345–351, Apr 2014.

[12] C. Baldasseroni, C. Bordel, A. X. Gray, A. M. Kaiser, F. Kronast, J. Herrero-Albillos, C. M. Schneider, C. S. Fadley, and F. Hellman. Temperature-driven nucleation of ferromagnetic domains in ferh thin films. *Applied Physics Letters*, 100(26):262401, 2012.

[13] C. Baldasseroni, G. K. Pálsson, C. Bordel, S. Valencia, A. A. Unal, F. Kronast, S. Nemsak, C. S. Fadley, J. A. Borchers, B. B. Maranville, and F. Hellman. Effect of capping material on interfacial ferromagnetism in FeRh thin films. *Journal of Applied Physics*, 115(4), 01 2014. 043919.

[14] Jan-Ulrich Thiele, Stefan Maat, and Eric E. Fullerton. Ferh/fept exchange spring films for thermally assisted magnetic recording media. *Applied Physics Letters*, 82(17):2859–2861, 2003.

[15] Y.I. Spichkin and A.M. Tishin. Magnetocaloric effect at the first-order magnetic phase transitions. *Journal of Alloys and Compounds*, 403(1):38–44, 2005.

[16] Meghmalhar Manekar and S B Roy. Reproducible room temperature giant magnetocaloric effect in fe–rh. *Journal of Physics D: Applied Physics*, 41(19):192004, sep 2008.

[17] Enric Stern-Taulats, Antoni Planes, Pol Lloveras, Maria Barrio, Josep-Lluís Tamarit, Sabyasachi Pramanick, Subham Majumdar, Carlos Frontera, and Lluís Mañosa. Barocaloric and magnetocaloric effects in $fe_{49}rh_{51}$. *Phys. Rev. B*, 89:214105, Jun 2014.

[18] Yang Liu, Lee C. Phillips, Richard Mattana, Manuel Bibes, Agnès Barthélémy, and Brahim Dkhil. Large reversible caloric effect in ferh thin films via a dual-stimulus multicaloric cycle. *Nature Communications*, 7(1):11614, May 2016.

[19] David W. Cooke, F. Hellman, C. Baldasseroni, C. Bordel, S. Moyerman, and E. E. Fullerton. Thermodynamic measurements of fe-rh alloys. *Phys. Rev. Lett.*, 109:255901, Dec 2012.

[20] M. Balli, S. Jandl, P. Fournier, and A. Kedous-Lebouc. Advanced materials for magnetic cooling: Fundamentals and practical aspects. *Applied Physics Reviews*, 4(2):021305, 2017.

[21] Hung Ba Tran, Tetsuya Fukushima, Hiroyoshi Momida, Kazunori Sato, Yukihiro Makino, and Tamio Oguchi. Direct and inverse magnetocaloric effects in ferh alloy. *Journal of Alloys and Compounds*, 926:166718, 2022.

[22] Jan-Ulrich Thiele, Matthias Buess, and Christian H. Back. Spin dynamics of the antiferromagnetic-to-ferromagnetic phase transition in ferh on a subpicosecond time scale. *Applied Physics Letters*, 85(14):2857–2859, 2004.

[23] Ganping Ju, Julius Hohlfeld, Bastiaan Bergman, René J. M. van de Veerdonk, Oleg N. Mryasov, Jai-Young Kim, Xiaowei Wu, Dieter Weller, and Bert Koopmans. Ultrafast generation of ferromagnetic order via a laser-induced phase transformation in ferh thin films. *Phys. Rev. Lett.*, 93:197403, Nov 2004.

[24] S. Maat, J.-U. Thiele, and Eric E. Fullerton. Temperature and field hysteresis of the antiferromagnetic-to-ferromagnetic phase transition in epitaxial ferh films. *Phys. Rev. B*, 72:214432, Dec 2005.

[25] M. E. Gruner, E. Hoffmann, and P. Entel. Instability of the rhodium magnetic moment as the origin of the metamagnetic phase transition in $\alpha-$FeRh. *Phys. Rev. B*, 67:064415, Feb 2003.

[26] M.E. Gruner and P. Entel. Simulation of the (ρ, t) phase diagram of the temperature-driven metamagnet α-ferh. *Phase Transitions*, 78(1-3):209–217, 2005.

[27] Brianne R. McGrath, Robert E. Camley, and Karen L. Livesey. Self-consistent local mean-field theory for phase transitions and magnetic properties of ferh. *Phys. Rev. B*, 101:014444, Jan 2020.

[28] Jiangwei Cao, Nguyen T. Nam, Sho Inoue, Hnin Yu Yu Ko, Nguyen N. Phuoc, and Takao Suzuki. Magnetization behaviors for ferh single crystal thin films. *Journal of Applied Physics*, 103(7):07F501, 2008.

[29] Ippei Suzuki, Tomoyuki Naito, Mitsuru Itoh, Tetsuya Sato, and Tomoyasu Taniyama. Clear correspondence between magnetoresistance and magnetization of epitaxially grown ordered ferh thin films. *Journal of Applied Physics*, 109(7):07C717, 2011.

[30] Federico Pressacco, Vojtěch Uhlíř, Matteo Gatti, Azzedine Bendounan, Eric E. Fullerton, and Fausto Sirotti. Stable room-temperature ferromagnetic phase at the ferh(100) surface. *Scientific Reports*, 6(1):22383, Mar 2016.

[31] C. Gatel, B. Warot-Fonrose, N. Biziere, L. A. Rodríguez, D. Reyes, R. Cours, M. Castiella, and M. J. Casanove. Inhomogeneous spatial distribution of the magnetic transition in an iron-rhodium thin film. *Nature Communications*, 8(1):15703, Jun 2017.

[32] G. C. Han, J. J. Qiu, Q. J. Yap, P. Luo, D. E. Laughlin, J. G. Zhu, T. Kanbe, and T. Shige. Magnetic stability of ultrathin FeRh films. *Journal of Applied Physics*, 113(17), 03 2013. 17C107.

[33] Tomasz Blachowicz and Andrea Ehrmann. Magnetic elements for neuromorphic computing. *Molecules*, 25(11), 2020.

[34] Pascal Andreazza, Veronique Pierron-Bohnes, Florent Tournus, Caroline Andreazza-Vignolle, and Veronique Dupuis. Structure and order in cobalt/platinum-type nanoalloys: from thin films to supported clusters. *Surface Science Reports*, 70(2):188–258, 2015.

[35] F. Tournus, K. Sato, T. Epicier, T. J. Konno, and V. Dupuis. Multi-$l1_0$ domain copt and fept nanoparticles revealed by electron microscopy. *Phys. Rev. Lett.*, 110:055501, Jan 2013.

[36] C Antoniak, M Spasova, A Trunova, K Fauth, F Wilhelm, A Rogalev, J Minár, H Ebert, M Farle, and H Wende. Inhomogeneous alloying in FePt nanoparticles as a reason for reduced magnetic moments. *J. Phys. Condens. Matter*, 21(33):336002, August 2009.

[37] R. Van Hardeveld and F. Hartog. The statistics of surface atoms and surface sites on metal crystals. *Surface Science*, 15(2):189–230, 1969.

[38] Diana Ciuculescu, Catherine Amiens, Marc Respaud, Andrea Falqui, Pierre Lecante, Robert E. Benfield, Linqin Jiang, Kai Fauth, and Bruno Chaudret. One-pot synthesis of core-shell ferh nanoparticles. *Chemistry of Materials*, 19(19):4624–4626, Sep 2007.

[39] Laurent Piccolo. Restructuring effects of the chemical environment in metal nanocatalysis and single-atom catalysis. *Catalysis Today*, 373:80–97, 2021. Perspectives in heterogeneous Catalysis on the Occasion of the 60th anniversary of the Research Institute of Catalysis of the CNRS, in Lyon-Villeubanne France.

[40] Vasiliki Papaefthimiou, Florent Tournus, Arnaud Hillion, Ghassan Khadra, Detre Teschner, Axel Knop-Gericke, Veronique Dupuis, and Spyridon Zafeiratos. Mixing patterns and redox properties of iron-based alloy nanoparticles under oxidation and reduction conditions. *Chemistry of Materials*, Feb 2014.

[41] Patrizio Benzo, Ségolène Combettes, Cécile Garcia, Teresa Hungria, Béatrice Pécassou, and Marie-José Casanove. Epitaxial growth of a gold shell on intermetallic ferh nanocrystals. *Crystal Growth & Design*, 20(6):4144–4149, Jun 2020.

[42] Florent Tournus. Multimer formation for two-dimensional random nanoparticle deposition. *Phys. Rev. E*, 84:011612, Jul 2011.

[43] Simón Oyarzún, Alexandre Tamion, Florent Tournus, Véronique Dupuis, and Matthias Hillenkamp. Size effects in the magnetic anisotropy of embedded cobalt nanoparticles: from shape to surface. *Scientific Reports*, 5(1):14749, Oct 2015.

[44] A. Kleibert, K.-H. Meiwes-Broer, and J. Bansmann. Size-dependent magnetic spin and orbital moments of fe nanoparticles deposited onto co/w(110). *Phys. Rev. B*, 79:125423, Mar 2009.

[45] Florent Tournus. Random nanoparticle deposition: inter-particle distances in 2d, 3d, and multilayer samples. *Journal of Nanoparticle Research*, 13(10):5211, Jul 2011.

[46] M Loving, F Jimenez-Villacorta, B Kaeswurm, D A Arena, C H Marrows, and L H Lewis. Structural evidence for stabilized ferromagnetism in epitaxial ferh nanoislands. *Journal of Physics D: Applied Physics*, 46(16):162002, apr 2013.

[47] Hnin Yu Yu Ko, Takao Suzuki, Nguyen N. Phuoc, and Jiangwei Cao. Fabrication and characterization of FeRh nanoparticles. *Journal of Applied Physics*, 103(7), 01 2008. 07D508.

[48] A. Hillion, A. Cavallin, S. Vlaic, A. Tamion, F. Tournus, G. Khadra, J. Dreiser, C. Piamonteze, F. Nolting, S. Rusponi, K. Sato, T. J. Konno, O. Proux, V. Dupuis, and H. Brune. Low temperature ferromagnetism in chemically ordered ferh nanocrystals. *Phys. Rev. Lett.*, 110:087207, Feb 2013.

[49] Nicola A. Spaldin and Manfred Fiebig. The renaissance of magnetoelectric multiferroics. *Science*, 309(5733):391–392, 2005.

[50] Nicola A. Spaldin and Manfred Fiebig. The renaissance of magnetoelectric multiferroics. *Science*, 309(5733):391–392, 2005.

[51] Muhammad Rizwan, Zahid Usman, Muhammad Shakil, S S A Gillani, S Azeem, H B Jin, C B Cao, Rana Farhat Mehmood, Ghulam Nabi, and Muhammad Adnan Asghar. Electronic and optical behaviour of lanthanum doped catio3 perovskite. *Materials Research Express*, 7(1):015920, jan 2020.

[52] Ziyong Cheng and Jun Lin. Layered organic–inorganic hybrid perovskites: structure, optical properties, film preparation, patterning and templating engineering. *CrystEngComm*, 12:2646–2662, 2010.

[53] W. Zhong, David Vanderbilt, and K. M. Rabe. Phase transitions in batio$_3$ from first principles. *Phys. Rev. Lett.*, 73:1861–1864, Sep 1994.

[54] Shizuo Miyake and Ryuzo Ueda. On phase transformation of batio3. *Journal of the Physical Society of Japan*, 2(5):93–97, 1947.

[55] G. H. Kwei, A. C. Lawson, S. J. L. Billinge, and S. W. Cheong. Structures of the ferroelectric phases of barium titanate. *The Journal of Physical Chemistry*, 97(10):2368–2377, Mar 1993.

[56] S. Nomura, T. Mitsui, K.H. Hellwege, and A.M. Hellwege. *Landolt-Börnstein: Numerical data and functional relationships in science and technology. New series. Crystal and solid state physics. Ferroelectrics and related substances. Oxides. 3:16a,*. Springer, 1981.

[57] Ronald E. Cohen. Origin of ferroelectricity in perovskite oxides. *Nature*, 358(6382):136–138, Jul 1992.

[58] G. Niu, S. Yin, G. Saint-Girons, B. Gautier, P. Lecoeur, V. Pillard, G. Hollinger, and B. Vilquin. Epitaxy of batio3 thin film on si(001) using a srtio3 buffer layer for non-volatile memory application. *Microelectronic Engineering*, 88(7):1232–1235, 2011. Proceedings of the 17th Biennial International Insulating Films on Semiconductor Conference.

[59] V. Garcia, S. Fusil, K. Bouzehouane, S. Enouz-Vedrenne, N. D. Mathur, A. Barthélémy, and M. Bibes. Giant tunnel electroresistance for non-destructive readout of ferroelectric states. *Nature*, 460(7251):81–84, Jul 2009.

[60] Catherine Dubourdieu, John Bruley, Thomas M. Arruda, Agham Posadas, Jean Jordan-Sweet, Martin M. Frank, Eduard Cartier, David J. Frank, Sergei V. Kalinin, Alexander A. Demkov, and Vijay Narayanan. Switching of ferroelectric polarization in epitaxial batio3 films on silicon without

a conducting bottom electrode. *Nature Nanotechnology*, 8(10):748–754, Oct 2013.

[61] P. Galinetto, F. Rossella, G. Samoggia, V. Trepakov, E. Kotomin, E. Heifets, P. Markovin, and L. Jastrabik. Structural phase transition and photo-charge carrier transport in srtio3. *Ferroelectrics*, 337(1):179–188, 2006.

[62] Jiahui Chen, Ya Gao, Liang Wu, Jing Ma, and Ce-Wen Nan. A magnetic glass state over the first-order ferromagnetic-to-antiferromagnetic transition in ferh film. *Materials Research Letters*, 5(5):329–334, 2017.

[63] S. P. Bennett, A. T. Wong, A. Glavic, A. Herklotz, C. Urban, I. Valmianski, M. D. Biegalski, H. M. Christen, T. Z. Ward, and V. Lauter. Giant controllable magnetization changes induced by structural phase transitions in a metamagnetic artificial multiferroic. *Scientific Reports*, 6(1):22708, Mar 2016.

[64] M. Jiang, X. Z. Chen, X. J. Zhou, B. Cui, Y. N. Yan, H. Q. Wu, F. Pan, and C. Song. Electrochemical control of the phase transition of ultrathin FeRh films. *Applied Physics Letters*, 108(20), 05 2016. 202404.

[65] Dimensions app. Total amount of publications that mention 'ferh' of 'iron-rhodium'. app.dimensions.ai.

[66] Arnaud Hillion, Alexandre Tamion, Florent Tournus, Clément Albin, and Véronique Dupuis. From vanishing interaction to superferromagnetic dimerization: Experimental determination of interaction lengths for embedded co clusters. *Phys. Rev. B*, 95:134446, Apr 2017.

[67] F. Parent, J. Tuaillon, L. B. Stern, V. Dupuis, B. Prevel, A. Perez, P. Melinon, G. Guiraud, R. Morel, A. Barthélémy, and A. Fert. Giant magnetoresistance in co-ag granular films preparedby low-energy cluster beam deposition. *Phys. Rev. B*, 55:3683–3687, Feb 1997.

[68] R. Alayan, L. Arnaud, M. Broyer, E. Cottancin, J. Lermé, J. L. Vialle, and M. Pellarin. Morphology and growth of metal clusters in the gas phase: A transition from spherical to ramified structures. *Phys. Rev. B*, 73:125444, Mar 2006.

[69] Magnetic Property Measurement System – MPMS-XL. Knuth: Computers and typesetting.

[70] Harold Weinstock and Martin nisenoff. *Microwave superconductivity*. Nato Science Series. Springer Science+Busines s Media , B.V ., 1999.

[71] F. R. Elder, A. M. Gurewitsch, R. V. Langmuir, and H. C. Pollock. Radiation from electrons in a synchrotron. *Phys. Rev.*, 71:829–830, Jun 1947.

[72] DEIMOS. Deimos webpage. https://www.synchrotron-soleil.fr.

[73] ID12. Id12 webpage. https://www.esrf.fr/.

[74] The International X ray Absorption Society. X-ray spectrocopy table. xrayabsorption.org.

[75] J. Stöhr. Exploring the microscopic origin of magnetic anisotropies with x-ray magnetic circular dichroism (xmcd) spectroscopy. *Journal of Magnetism and Magnetic Materials*, 200(1):470–497, 1999.

[76] M. Sacchi and J. Vogel. *Magnetism and Synchrotron Radiation, Lecture Notes in Physics*, volume 565. Springer Verlag, 2001.

[77] Heiko Wende. Recent advances in x-ray absorption spectroscopy. *Reports on Progress in Physics*, 67(12):2105, oct 2004.

[78] J. L. Erskine and E. A. Stern. Calculation of the M_{23} magneto-optical absorption spectrum of ferromagnetic nickel. *Phys. Rev. B*, 12:5016–5024, Dec 1975.

[79] G. Schütz, W. Wagner, W. Wilhelm, P. Kienle, R. Zeller, R. Frahm, and G. Materlik. Absorption of circularly polarized x rays in iron. *Phys. Rev. Lett.*, 58:737–740, Feb 1987.

[80] Paolo Carra, B. T. Thole, Massimo Altarelli, and Xindong Wang. X-ray circular dichroism and local magnetic fields. *Phys. Rev. Lett.*, 70:694–697, Feb 1993.

[81] B. T. Thole, P. Carra, F. Sette, and G. van der Laan. X-ray circular dichroism as a probe of orbital magnetization. *Phys. Rev. Lett.*, 68:1943–1946, Mar 1992.

[82] C. T. Chen, Y. U. Idzerda, H.-J. Lin, N. V. Smith, G. Meigs, E. Chaban, G. H. Ho, E. Pellegrin, and F. Sette. Experimental confirmation of the x-ray magnetic circular dichroism sum rules for iron and cobalt. *Phys. Rev. Lett.*, 75:152–155, Jul 1995.

[83] O. Šipr, J. Minár, and H. Ebert. On the importance of the magnetic dipole term tz in analyzing x-ray magnetic circular dichroism spectra of clusters. *Europhysics Letters*, 87(6):67007, oct 2009.

[84] P. Moskovkin, S. Pisov, M. Hou, C. Raufast, F. Tournus, L. Favre, and V. Dupuis. Model predictions and experimental characterization of co-pt alloy clusters. *The European Physical Journal D*, 43(1):27–32, Jul 2007.

[85] Ostwald,W. Blocking of ostwald ripening allowing long-term stabilization. *Z. Phy. Chem.*, 37:385, 1901.

[86] Alexandre Tamion, Matthias Hillenkamp, Florent Tournus, Edgar Bonet, and Véronique Dupuis. Accurate determination of the magnetic anisotropy in cluster-assembled nanostructures. *Applied Physics Letters*, 95(6):062503, 2009.

[87] Edmund Clifton Stoner and E. P. Wohlfarth. A mechanism of magnetic hysteresis in heterogeneous alloys. *Philosophical Transactions of the Royal Society of London. Series A, Mathematical and Physical Sciences*, 240(826):599–642, 1948.

[88] V. Dupuis, A. Hillion, and A. et al Robert. Bottom-up strategies for the assembling of magnetic systems using nanoclusters. *J Nanopart Res*, 20:128, 2018.

[89] Herrera, Guillermo, Robert, Anthony, Dupuis, Veronique, Blanchard, Nicholas, Boisron, Olivier, Albin, Clement, Bardotti, Laurent, Le Roy, Damien, Tournus, Florent, and Tamion, Alexandre. Chemical and magnetic order in mass-selected large ferh nanomagnets embedded in a carbon matrix. *Eur. Phys. J. Appl. Phys.*, 97:32, 2022.

[90] A. L. Patterson. The scherrer formula for x-ray particle size determination. *Phys. Rev.*, 56:978–982, Nov 1939.

[91] J.P. Perez, V. Dupuis, J. Tuaillon, A. Perez, V. Paillard, P. Melinon, M. Treilleux, L. Thomas, B. Barbara, and B. Bouchet-Fabre. Magnetic properties of nanostructured iron films obtained by low energy neutral cluster beam deposition. *Journal of Magnetism and Magnetic Materials*, 145(1):74–80, 1995.

[92] S. Torquato, T. M. Truskett, and P. G. Debenedetti. Is random close packing of spheres well defined? *Phys. Rev. Lett.*, 84:2064–2067, Mar 2000.

[93] N. Blanc, L. E. Díaz-Sánchez, A. Y. Ramos, F. Tournus, H. C. N. Tolentino, M. De Santis, O. Proux, A. Tamion, J. Tuaillon-Combes, L. Bardotti, O. Boisron, G. M. Pastor, and V. Dupuis. Element-specific quantitative determination of the local atomic order in copt alloy nanoparticles: Experiment and theory. *Phys. Rev. B*, 87:155412, Apr 2013.

[94] F. Baudelet, A. Fontaine, G. Tourillon, D. Guay, M. Maurer, M. Piecuch, M. F. Ravet, and V. Dupuis. Iron atomic packing in fe-ru superlattices by x-ray-absorption spectroscopy. *Phys. Rev. B*, 47:2344–2352, Jan 1993.

[95] A. Smekhova, D. Ciuculescu, P. Lecante, F. Wilhelm, C. Amiens, A. Rogalev, and B. Chaudret. X-ray magnetic circular dichroism studies of ferh nanoparticles. *IEEE Transactions on Magnetics*, 44(11):2776–2779, 2008.

[96] Alex Aubert, Konstantin Skokov, Gabriel Gomez, Alisa Chirkova, Iliya Radulov, Fabrice Wilhelm, Andrei Rogalev, Heiko Wende, Oliver Gutfleisch, and Katharina Ollefs. Simultaneous multi-property probing during magneto-structural phase transitions: An element-specific and macroscopic hysteresis characterization at id12 of the esrf. *IEEE Transactions on Instrumentation and Measurement*, 71:1–9, 2022.

[97] V. Uhlíř, J. A. Arregi, and E. E. Fullerton. Colossal magnetic phase transition asymmetry in mesoscale ferh stripes. *Nature Communications*, 7(1):13113, Oct 2016.

[98] G. F. M. Gomes, T. E. P. Bueno, D. E. Parreiras, G. J. P. Abreu, A. de Siervo, J. C. Cezar, H.-D. Pfannes, and R. Paniago. Magnetic moment of fe_3o_4 films with thicknesses near the unit-cell size. *Phys. Rev. B*, 90:134422, Oct 2014.

[99] Michel Sassi, Carolyn I. Pearce, Paul S. Bagus, Elke Arenholz, and Kevin M. Rosso. First-principles fe l2,3-edge and o k-edge xanes and xmcd spectra for iron oxides. *The Journal of Physical Chemistry A*, 121(40):7613–7618, Oct 2017.

[100] Waiz Karim, Armin Kleibert, Urs Hartfelder, Ana Balan, Jens Gobrecht, Jeroen A van Bokhoven, and Yasin Ekinci. Size-dependent redox behavior of iron observed by in-situ single nanoparticle spectro-microscopy on well-defined model systems. *Scientific reports*, 6(1):1–8, 2016.

[101] C. Stamm, J.-U. Thiele, T. Kachel, I. Radu, P. Ramm, M. Kosuth, J. Minár, H. Ebert, H. A. Dürr, W. Eberhardt, and C. H. Back. Antiferromagnetic-ferromagnetic phase transition in ferh probed by x-ray magnetic circular dichroism. *Phys. Rev. B*, 77:184401, May 2008.

[102] Jill Chastain and Roger C King Jr. Handbook of x-ray photoelectron spectroscopy. *Perkin-Elmer Corporation*, 40:221, 1992.

[103] Kevin Ruwisch, Tobias Pohlmann, Florian Bertram, Christoph Schlüter, Andrei Gloskovskii, Karsten Küpper, and Joachim Wollschläger. Real-time monitoring the growth of epitaxial $co_x fe_{3-x} o_4$ ultrathin films on nb-doped

srtio3(001) via reactive molecular beam epitaxy by means of operando haxpes. *Materials*, 15(7), 2022.

[104] Qiang Fu, Thomas Wagner, Sven Olliges, and Heinz-Dieter Carstanjen. Metal-oxide interfacial reactions: encapsulation of pd on tio2 (110). *The Journal of Physical Chemistry B*, 109(2):944–951, Jan 2005.

[105] P. Catrou, S. Tricot, G. Delhaye, J.-C. Le Breton, P. Turban, B. Lépine, and P. Schieffer. Effect of oxygen vacancies at the Fe/srtio$_3$(001) interface: Schottky barrier and surface electron accumulation layer. *Phys. Rev. B*, 98:115402, Sep 2018.

[106] Yangyang Li, Yunshang Zhang, Kun Qian, and Weixin Huang. Metal–support interactions in metal/oxide catalysts and oxide–metal interactions in oxide/metal inverse catalysts. *ACS Catalysis*, 12(2):1268–1287, Jan 2022.

[107] Peiyu Chen, Yakun Gao, and Martin R. Castell. Thermodynamics driving the strong metal support interaction: Titanate encapsulation of supported pd nanocrystals. *Phys. Rev. Mater.*, 5:075001, Jul 2021.

[108] Qiang Fu and Thomas Wagner. Interaction of nanostructured metal overlayers with oxide surfaces. *Surface Science Reports*, 62(11):431–498, 2007.

[109] T. Wagner, A. D. Polli, G. Richter, and H. Stanzick. Epitaxial growth of metals on (100) srtio3: The influence of lattice mismatch and reactivity. *International Journal of Materials Research*, 92(7):701–706, 2001.

[110] S. Bernal, J.J. Calvino, M.A. Cauqui, J.M. Gatica, C. López Cartes, J.A. Pérez Omil, and J.M. Pintado. Some contributions of electron microscopy to the characterisation of the strong metal-support interaction effect. *Catalysis Today*, 77(4):385–406, 2003. Fundamentals of Catalysis and Applications to Environmental Problems.

[111] Elizabeth R. Hopper, Christina Boukouvala, Duncan N. Johnstone, John S. Biggins, and Emilie Ringe. On the identification of twinning in body-centred cubic nanoparticles. *Nanoscale*, 12:22009–22013, 2020.

[112] H.H Ku. Notes on the use of propagation of error formulas. *Journal of Research of the National Bureau of Standards. Section C: Engineering and Instrumentation*, 70C(4), 10 1966.

[113] D. A. Allwood, G. Xiong, C. C. Faulkner, D. Atkinson, D. Petit, and R. P. Cowburn. Magnetic domain-wall logic. *Science*, 309(5741):1688–1692, 2005.

[114] Vajtai R. *Springer Handbook of Nanomaterials*. Springer Science and Business Media, 2013.

[115] C Tannous and J Gieraltowski. The stoner–wohlfarth model of ferromagnetism. *European Journal of Physics*, 29(3):475, mar 2008.

[116] Louis Néel. Influence des fluctuations thermiques sur l'aimantation de grains ferromagnétiques très fins. *Comptes Rendus Hebdomadaires Des Seances De L Academie Des Sciences*, 228(8):664–666, 1949.

[117] William Fuller Brown. Thermal fluctuations of a single-domain particle. *Phys. Rev.*, 130:1677–1686, Jun 1963.

[118] J.L. Dormann. Le phénomène de superparamagnétisme. *Revue de Physique Appliquée*, 16(6):275–301, 1981.

[119] W. Wernsdorfer, E. Bonet Orozco, K. Hasselbach, A. Benoit, B. Barbara, N. Demoncy, A. Loiseau, H. Pascard, and D. Mailly. Experimental evidence of the néel-brown model of magnetization reversal. *Phys. Rev. Lett.*, 78:1791–1794, Mar 1997.

[120] P. Bruno and C. Chappert. Ruderman-kittel theory of oscillatory interlayer exchange coupling. *Phys. Rev. B*, 46:261–270, Jul 1992.

[121] S. S. P. Parkin, N. More, and K. P. Roche. Oscillations in exchange coupling and magnetoresistance in metallic superlattice structures: Co/ru, co/cr, and fe/cr. *Phys. Rev. Lett.*, 64:2304–2307, May 1990.

[122] H.A Kramers. L'interaction entre les atomes magnétogènes dans un cristal paramagnétique. *Physica*, 1(1):182–192, 1934.

[123] Jesús García-Otero, Markus Porto, José Rivas, and Armin Bunde. Influence of dipolar interaction on magnetic properties of ultrafine ferromagnetic particles. *Phys. Rev. Lett.*, 84:167–170, Jan 2000.

[124] O. Hellwig, A. Berger, T. Thomson, E. Dobisz, Z. Z Bandic, H. Yang, D. S. Kercher, and E. E. Fullerton. Separating dipolar broadening from the intrinsic switching field distribution in perpendicular patterned media. *Applied Physics Letters*, 90(16):162516, 2007.

[125] S A Majetich and M Sachan. Magnetostatic interactions in magnetic nanoparticle assemblies: energy, time and length scales. *Journal of Physics D: Applied Physics*, 39(21):R407, oct 2006.

[126] P. I. Mayo, K. O'Grady, P. E. Kelly, J. Cambridge, I. L. Sanders, T. Yogi, and R. W. Chantrell. A magnetic evaluation of interaction and noise characteristics of conicr thin films. *Journal of Applied Physics*, 69(8):4733–4735, 1991.

[127] X. Batlle, M. García del Muro, and A. Labarta. Interaction effects and energy barrier distribution on the magnetic relaxation of nanocrystalline hexagonal ferrites. *Phys. Rev. B*, 55:6440–6445, Mar 1997.

[128] J Rivas, A Kazadi Mukenga Bantu, G Zaragoza, M.C Blanco, and M.A López-Quintela. Preparation and magnetic behavior of arrays of electrodeposited co nanowires. *Journal of Magnetism and Magnetic Materials*, 249(1):220–227, 2002. International Workshop on Magnetic Wires.

[129] O. Henkel. Remanenzverhalten und wechselwirkungen in hartmagnetischen teilchenkollektiven. *physica status solidi (b)*, 7(3):919–929, 1964.